Coherent Transient Spectroscopy with Continuous Wave Quantum Cascade Lasers

A thesis submitted for the degree of Doctor of Philosophy

by

James Kirkbride

Wolfson College, University of Oxford

Trinity term 2014

Declaration of Authorship

I, James Kirkbride, declare that this thesis entitled, 'Coherent Transient Spectroscopy with Continuous Wave Quantum Cascade Lasers' and the work presented in it are my own. I confirm that:

- This work was done wholly or mainly while in candidature for a research degree at this University.
- Where any part of thesis thesis has previously been submitted for a degree or any other qualification at this University or any other institution, this has been clearly stated.
- Where I have consulted the published work of others, this is always clearly attributed.
- Where I have quoted from the work of others, the source is always given. With the exception of such quotations, this thesis is entirely my own work.
- I have acknowledged all main sources of help
- Where the thesis is based on work done by myself jointly with others, I have made clear exactly what was done by others and what I have contributed myself.

Signature: _____

Date: _____

Abstract

This thesis is concerned with coherent effects in high resolution mid-infrared gas phase spectroscopy using quantum cascade lasers (QCLs). An introductory chapter explains the importance of QCLs as radiation sources in the mid-infrared region of the spectrum and goes on to detail their development and structure. A discussion of coherent effects in spectroscopy follows, leading into the second chapter which discusses the theories relevant to the experimental sections of the thesis.

In chapter 2 the theory underpinning direct and velocity selective, Doppler-free spectroscopy is discussed and a density matrix formalism is followed to derive the equations of motion that govern coherent excitation effects in two-level systems. In the final part of the chapter this treatment is extended to three-level systems. The equations derived in this chapter form the basis of quantitative interpretations of the phenomena observed in experimental data and presented in the remainder of the thesis.

In chapter 3 the characterisation of a high power, narrow linewidth QCL is carried out. This laser is then used to perform direct and sub-Doppler resolution spectroscopy on NO, demonstrating non-linear absorption at high laser intensities and providing a measurement of the laser linewidth in the limit of slow frequency tuning. As the slow tuning rate increases, evidence of coherent transient effects is presented and density matrix theory used to model this behaviour. The data presented include the first observations of asymmetric Lamb dips and the onset of rapid passage oscillations from a Lamb dip.

Pump-probe experiments on NO, utilising two cw QCLs are presented in chapter

4. The high level of velocity selection afforded by QCL excitation leads to coherent transient signals at far lower probe scan rates than previously reported. The effect of altering both the scan rate and the gas pressure and the importance of hyperfine structure are presented. A radio frequency noise source applied to one of the lasers is shown to broaden the laser linewidth, leading to rapid dephasing. A two-colour polarisation spectroscopy experiment is also presented which allows the measurement of both the absorption and the Doppler-free dispersion signals and the three-level density matrix formalism presented at the end of chapter 2 used to model the non-linear response of the system.

The final chapter details the use of an acousto-optic modulator to create a pulse of mid-IR light using a cw QCL and the application of this to time resolved pump-probe spectroscopy. This capability suggests the prospect of achieving coherent population transfer by stimulated Raman adiabatic passage (STIRAP) using two such pulses. Simulations based on a simple three-level model and including Zeeman coherences are presented, which take the measured properties of the lasers used in this thesis as inputs to predict the potential population transfer achievable in NO as well as providing useful information about the angular momentum polarisation of the excited molecules. An experimental realisation of STIRAP would require the lasers to be stabilised, and so the final part of the chapter details experimental attempts to achieve stabilisation of an external cavity QCL, and suggests future avenues for improved implementation.

Acknowledgements

Four years is a long time and I can't possibly begin to thank all the people who have helped me out on my way to finally finishing this thesis. I should start by thanking Grant for giving me a place in his group. Having heard several horror stories from friends with bad supervisors, I have to say that I feel lucky that Grant's approach to supervision has produced a group that is fun to be a part of and the enthusiasm he has for the project is inspiring.

My early days were spent under the tutelage of Rich Walker. Thanks to him I learnt all about Lamb dip spectroscopy and how awesome QCLs are. I'm sorry to disappoint you Rich but as yet I have failed to win the notorious Hepwood prize. I also wish to thank Damien for the guidance he provided through barely understood technical discussions and completely illegible notes on draft papers.

The two part IIs I've worked with deserve a mention for their 'help' with this work. Sarah suffered through my attempts to work out how to guide another person to do my experiment and eventually realised I wasn't going to shout at her. I learnt a huge amount from the time we worked together and I think that year was probably the most successful time on the experiment. Andrew taught me what stress really is and despite my inability to deal with all of his questions, he made a valuable contribution to the work in this thesis.

Due to Grant's habit of coming into the office to catch up on progress the evening before group meetings, these events usually became a time to explain my findings and my problems to Gus and my thanks are due to him both for his guidance and for his excellent skills as a raconteur. His numerous tales of life in the PTCL are

always a welcome break.

Fellow group members past and present deserve a mention for tea time talks and for those talks rarely being about science. Julian and Katy both truly understood how Anngry one can get when food is not forthcoming and although I don't think Ann every had the same feeling, she did put up with us and force a waiter to give us snacks when the three of us were too busy complaining to do anything for ourselves. Katherine is to be thanked in particular for her baking skills although I think she does some science too. Helen joined the group as a part II at the same time I joined as a DPhil student and she has been a constant source of bizarre tea time topics throughout this time.

I should mention Kim, my fellow year group member and the most organised person I know. Her hard work, dedication and meticulous planning are an inspiration for me to be a better person and it's no surprise that I am writing this *after* she has already graduated with her DPhil.

Outside of the lab my chief distraction throughout my time here has been messing about in boats. Although many would not say that rowing has particularly aided my studies, my thanks are due to the innumerable people involved in the Wolf Pack (Wolfson College Boat Club) and Oxford University Lightweight Rowing Club. There really are too many of you to mention you all by name but without you my Oxford experience would have been very different. The characters I've met in four years of rowing here will live in my memory long after I finally give up this ridiculous sport. Special mention goes to Gregers, Peter Haining, and Dr J for being some of the most unconventionally inspiring people I have ever had the fortune to know.

The final mention should go to my parents who have had to get used to never seeing me and have had to put up with my infrequent calls but have always supported me unwaveringly and smiled and nodded politely when I told them all about the problems with my experiment. I could not wish for a more supportive family and you have both my never ending gratitude and undying love.

List of Publications

- R. J. Walker, J. H. van Helden, J. M. R. Kirkbride, E. A. McCormack, M. T. Bell, D. Weidmann and G. A. D. Ritchie, "Rapid passage signals from a vibrationally excited target molecule: a pump and probe experiment with continuous wave quantum cascade lasers," *Optics Letters*, vol. 36, no. 24, pp. 4725-7, 2011.

- R. J. Walker, J. M. R. Kirkbride, J. H. van Helden, D. Weidmann and G. A. D. Ritchie, "Sub-Doppler spectroscopy with an external cavity quantum cascade laser," *Applied Physics B,* vol. 112, no. 2, pp. 159-167, 2013.

- J. M. R. Kirkbride, S. K. Causier, E. A. McCormack, D. Weidmann and G. A. D. Ritchie, "Coherent transient spectroscopy with continuous wave quantum cascade lasers," *Physical chemistry chemical physics,* vol. 15, no. 8, pp. 2684-91, 2013.

- J. M. R. Kirkbride, S. K. Causier, A. R. Dalton, D. Weidmann and G. A. D. Ritchie, "Pump and probe spectroscopy with continuous wave quantum cascade lasers," *The Journal of Chemical Physics,* vol. 140, no. 5, p. 054311, 2014

- J. M. R. Kirkbride, A. R. Dalton and G. A. D. Ritchie, "Polarization spectroscopy of a velocity-selected molecular sample," *Optics Letters,* vol. 39, no. 9, p. 2645, 2014.

- K. M. Manfred, J. M. R. Kirkbride, L. Ciaffoni, R. Peverall, G. Hancock and G. A. D. Ritchie, "Enhancing the Sensitivity of Mid-Infrared QCL-based

Cavity-Enhanced Absorption Spectroscopy using RF Current Perturbation," *Optics Letters (In Preparation).*

Contents

Chapter 1

Introduction

1.1 Mid Infra-Red Spectroscopy with Quantum Cascade Lasers

In recent years the telecoms industry has forced the technological advancement of near infra-red single mode continuous wave (cw) lasers whose bandwidths (< 10 MHz) allow sub-Doppler resolution of gas phase spectroscopic features. Semiconductor diode lasers emitting in the visible to near-IR wavelength region (400 nm - 1.4 µm are readily available across this wavelength region, are economical, efficient, operate at room temperature, can output relatively high powers, are easily electronically modulated and are very robust. However they have limited tunability (unless placed in an extended cavity system) and whilst the spectral region that they cover contains vibrational overtone bands, these transitions have relatively small absorption cross sections, generally requiring sensitivity enhanced techniques to be employed for the detection of trace gases. Fundamental rotation-vibrational transitions occur in the mid-IR region from 3 µm to 12 µm and have much larger cross sections (typically two orders of magnitude) offering the prospect of increased sensitivity and selectivity for trace gas detection [1]. Until relatively recently there were few single mode laser sources available in this region, being limited to lead salt diode lasers [2, 3] or Difference Frequency Generation (DFG) [4, 5] using two

shorter wavelength near-IR diode lasers. Lead salt diode lasers require cryogenic cooling and are limited to low output powers, similarly DFG systems produce only up to a few mW of optical power (and often considerably less with unamplified laser sources) and require complex optical and electronic setups [6]. These drawbacks are addressed by the recent development of quantum cascade lasers.

The first quantum cascade laser (QCL) was demonstrated in 1994 by Faist *et al.* [7], emitting at 4.2 µm. This first laser operated only in pulsed mode in which a current pulse is applied to the laser causing rapid Joule heating and a consequent change in the laser output frequency. Recent advances in QCL design have enabled the production of high powered single mode cw lasers with narrow linewidths [8–11]. These are ideal sources not only for sensing strategies based on modulation spectroscopy such as wavelength modulation spectroscopy (WMS) [12–15] and cavity enhanced absorption and ringdown spectroscopies (CEAS, CRDS) [16–20], but also for non-linear spectroscopy [21] and vibrational state preparation. QCLs address many of the drawbacks of other laser systems available in the mid IR frequency range and offer scope to perform highly sensitive spectroscopic measurements as well as non-linear spectroscopy which is the subject of this thesis.

1.1.1 The Structure of Quantum Cascade Lasers

While the principle behind the construction of a quantum cascade laser was initially proposed by Kazarinov and Suris in 1971, [22] it wasn't until the advancement of molecular beam epitaxy and chemical vapour deposition that it was possible to make such a laser. The operating principle behind a QCL differs significantly from that of traditional semiconductor diode lasers. In diode lasers electrons from the conduction n-type doped band combine with holes from the valence p-type doped band at a p-n junction. Application of an electrical potential across the laser diode causes the electrons and holes to re-combine across the band gap, emitting a photon in the process as shown schematically in figure 1.1. The energy of the emitted photon is determined by the size of the band gap. To achieve emission in the mid-IR the band

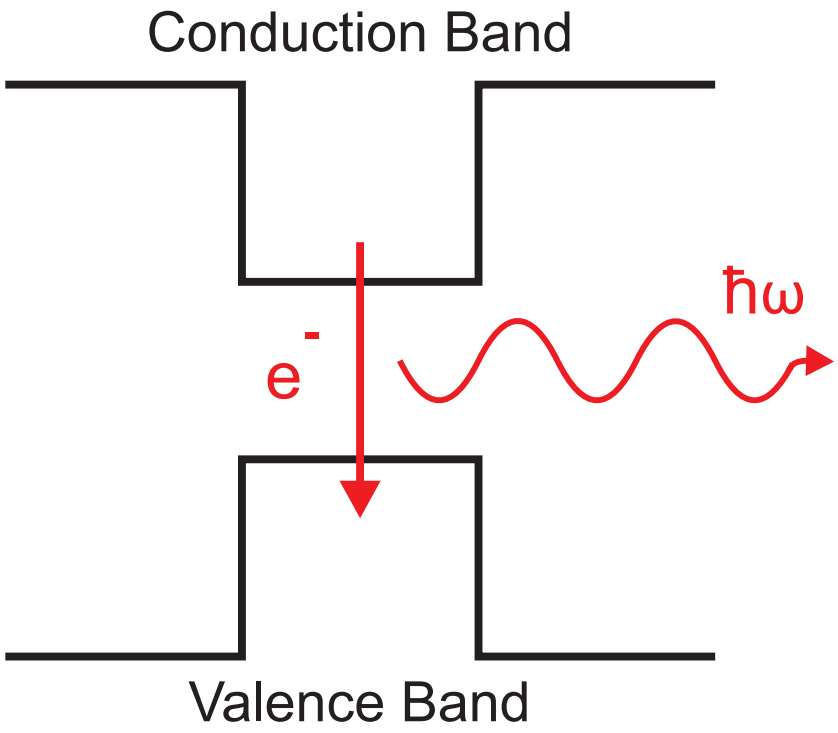

Figure 1.1: A schematic of a diode laser active region. An electron from the conduction band combines with an electron hole in the valence band releasing a photon with an energy corresponding to the band gap energy.

gap must be relatively small, but this leads to efficient Auger recombination, a non-radiative process which drastically reduces the efficiency of the diode and makes the design unsuitable for wavelengths longer than ∼2 µm [23, 24]. Recent advances in GaSb semiconductor lasers however, have allowed the production of lasers emitting at up to 3.6 µm [25–27]

QCLs differ from the traditional diode laser as they involve intersubband transitions rather than transitions from the conduction band into the valence band, relying on only one type of charge carrier. A QCL is made up of periodic thin layers of alternating high and low band gap semiconductors which form a superlattice [7, 28]. As the layer thickness approaches the de Broglie wavelength of the material electrons are confined into one-dimensional quantum wells. The energy states of the quantum wells are defined by the layer thickness and therefore by suitable design of layer thickness it is possible to achieve the population inversion between two subbands necessary for laser emission. As layer thickness rather than material band gap determines

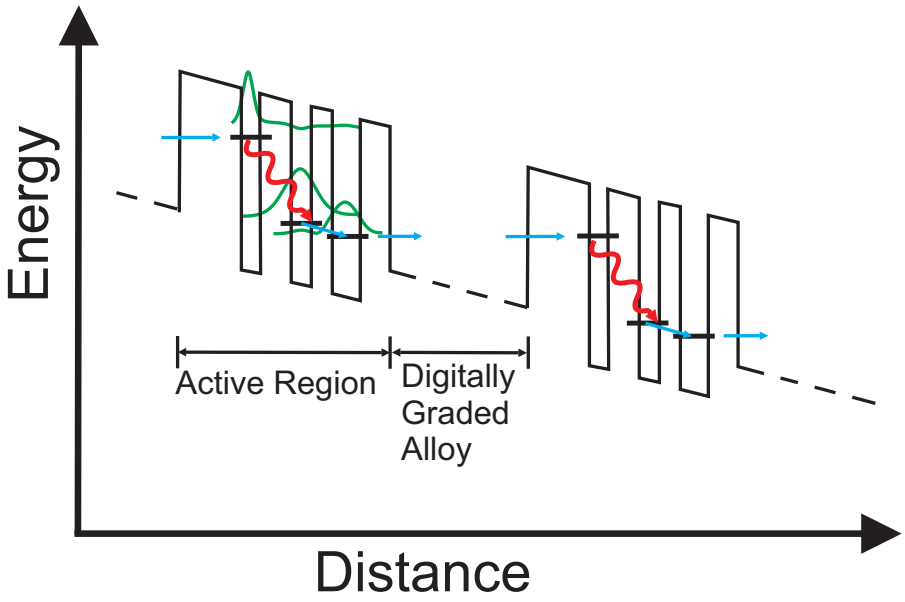

Figure 1.2: Two active regions of a QCL. Electrons are injected into the upper laser level from the digitally graded alloy and relax into the lower laser level, releasing a photon (red wavy line) in the process. The electrons then transition rapidly from the lower laser level into the ground level before tunnelling into the digitally graded alloy and thus into the next active region. The slope in the energy levels is determined by the magnitude of the electric field across the laser. This figure shows a diagonal transition. Wavefunctions are shown in green for example only. Adapted from [7].

the wavelength of emission, it is possible to make QCLs with a wide range of emission wavelengths using mature semiconductor technology. Typical semiconductor materials for QCL manufacture are InGaAs/AlInAs [7] and GaAs/Al(Ga)As [29].

Figure 1.2 shows a typical three quantum well active region. Electrons are injected into the the upper laser level and undergo radiative decay into the lower laser level. The electrons then quickly decay into a third level, the ground level (which is slightly lower in energy than the lower laser level) and then into digitally graded alloy. The rate of decay from the lower laser level into the ground level is sufficiently fast that it maintains population inversion between the upper and lower laser levels.

The barrier thickness between wells is chosen so that tunnelling between wells is an efficient process and the electronic wavefunctions span all of the wells in the active region. If the layer thickness is chosen such that the wavefunction for the upper laser level lies mainly in the left hand well with the lower laser level wavefunction lying towards the central and right hand wells then the emitting transition is known

as a diagonal transition. Vertical transitions occur when the upper state wavefunction also lies towards the central and right hand wells. Vertical transitions reduce population inversion since there is greater overlap between the two wavefunctions but the increased transition strength increases the gain. A vertical transition is less susceptible to applied electric field and temperature than the diagonal design. This feature lends itself well to making stable fixed frequency lasers but results in limited tunability. [28] By contrast diagonal designs are less stable to applied electric fields, showing wavelength dependence through a voltage induced Stark effect, and thus allow the laser greater tunability.

The lower laser level and the ground level are designed to have a large overlap between their wavefunctions and so increase the rate of depopulation of the lower laser level and maintain population inversion between the two laser levels. Some designs involve the upper laser state decaying into a continuum of lower states; not only do these bound to continuum lasers guarantee the rapid removal of electrons from the lower state, but they also benefit from increased output frequency range, enabling tuning of up to $150\,\mathrm{cm}^{-1}$ and allow high current flow which in turn gives rise to high optical power. [28, 30–32]

A QCL chip consists of may active regions (typically 30-100) and when a potential is applied across the chip it causes a shift in the energy levels such that each active region lies to slightly lower energy than the previous one. [33] Thus an electron cascades down through many active regions, emitting a photon at each of them. In this way it has been demonstrated that the wall plug efficiency of QCLs (the optical output power divided by the electrical power drawn) can exceed 50% and optical powers in excess of 1 W have been reported for room temperature continuous wave operation. [11, 34–37]

Early QCLs only operated in pulsed mode and required cryogenic cooling. The high current required results in Joule heating of the laser, where the heat produced

Q, is proportional to the square of the current according to Joule's first law:

$$Q \propto I^2 R, \tag{1.1}$$

where R is the resistance across the laser. Commonly QCLs require several hundred mA of current and have a voltage drop of several volts meaning that for cw operation several watts of power are dissipated as heat and light. As the temperature of the laser increases, so does the threshold current required for laser operation which thus requires very efficient cooling in order to allow continuous operation. This can be achieved by increasing the wall plug efficiency through active region design, resulting in less heat being produced and more light [35]. Advances in mounting of the lasers such as the 'epi-down' mounting [38] by which the laser gain medium directly contacts a heat sink give increased heat dissipation. These advances have meant that current QCLs can operate in pulsed mode with air cooling only and cw devices are able to operate at room temperature, usually with only water cooling.

1.1.2 Wavelength Selection in QCLs

Wavelength selection in QCLs is much the same as it is for standard diode lasers. The gain medium is first formed into an optical waveguide; the parallel ends of the gain medium are cleaved along the crystal axis, producing reflective surfaces due to the large refractive index change into air. This forms a Fabry-Perot laser cavity which amplifies a set of frequencies according to the free spectral range of the cavity $\Delta\nu$:

$$\Delta\nu = \frac{c}{2nl}, \tag{1.2}$$

where n is the refractive index of the gain medium and l is the length of the resonator. Typically one facet will be coated in a high reflectivity material to minimise light lost from that facet and thus increase the efficiency of the resonator. The gain spectrum of the laser medium is quite broad and so the laser output spans many modes of the resonator, separated by the free spectral range. Altering the temperature and/or

current supplied to the laser chip will change the output wavelengths. Multi-mode lasers may be used for high resolution detection of multiple gas species using the technique called multi-mode absorption spectroscopy (MUMAS) [39, 40] and Fabry-Perot QCLs make ideal sources for these kinds of measurements.

The active medium of the laser is surrounded by a cladding layer. If a diffraction grating is etched into this cladding layer then the wavelengths present in the gain medium will be further selected by this so-called 'Bragg grating'. The Bragg grating supports only certain modes within the resonator, feeding back to the gain material, resulting in a single output mode being selected and allowing for narrow laser linewidths. Altering the temperature changes the spacing of the grating and thus changes the output wavelength by changing the modes supported; altering the current has a similar effect to changing the temperature. This type of laser is known as a distributed feedback (DFB) laser [41–43].

Another method for selecting a single lasing mode is to utilise an external cavity (EC) containing a grating. A Fabry-Perot type resonator is placed in an external cavity and one facet is anti-reflection coated so that the laser modes must satisfy the resonance conditions for the external cavity. A movable grating placed within the cavity allows the selection of a single wavelength. Changing the grating angle then allows tuning of up to 15% of the free-running wavelength [32].

The configuration of the EC-QCL used in this thesis is known as the double-ended Littrow configuration [44]. The gain medium sits between two collimating lenses with one directing the light onto a diffraction grating and the other outputting the light. The double-ended configuration ensures that the output beam direction remains constant regardless of the grating angle unlike that in the standard Littrow configuration [46, 47].

Distributed feedback QCLs are relatively easy to produce since the technology to etch the gratings onto the waveguides is mature, being widely used in semiconductor diode lasers. However the wavelength tuning, by temperature and/or current is limited to a few cm^{-1}. By contrast EC-QCLs offer much larger tuning ranges (typically

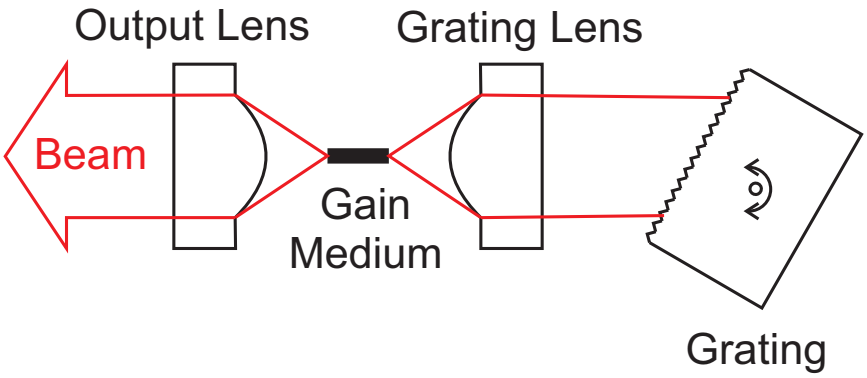

Figure 1.3: Schematic representation of the double-ended Littrow external cavity configuration. Adapted from [45].

around 150 cm^{-1} but > 500 cm^{-1} in some cases [8, 32, 45]) but are technically more challenging to produce, making them far more costly.

Regardless of whether single mode lasers select their output wavelength through distributed feedback or with an external cavity, the narrow linewidths and high powers afforded by QCLs in comparison to previously available mid-IR lasers makes them an invaluable tool in high resolution spectroscopy and chemical sensing [48]. Their narrow linewidths allow the discrimination of different species absorbing at similar wavelengths and the large absorption cross sections of molecules in the mid-IR allow the very low detection limits. For example QCLs have been used in conjunction with CRDS to detect NO at ppb level with a sensitivity of 0.7 ppb [49]. They have also been used by Nelson *et al.* to measure less than 1 ppb NO using a multi-pass cell [50], and by Webster *et al.* to measure stratospheric CH_4 to a minimum of 2 ppb [51].

1.1.3 Linewidths of QCLs

A fundamental limit on the linewidth of a laser was first proposed by Schawlow and Townes, [52] and adapted to diode lasers by Henry producing equation (1.3): [53]

$$\delta\omega = \frac{v_g^2 h\omega\alpha\alpha_m n_{sp}}{4\pi P_0}\left(1+\alpha_e^2\right), \tag{1.3}$$

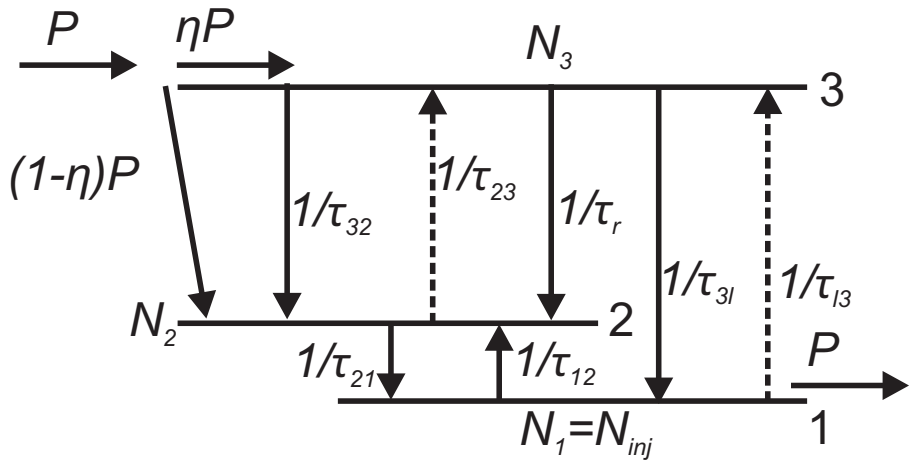

Figure 1.4: The three level model employed by Yamanishi *et al.* showing the rate processes within the active region of the gain medium. Reproduced from [56]

where v_g is the group velocity of the electrons, α the cavity losses, α_m the mirror losses, n_{sp} is the spontaneous emission factor, P_0 the output power and α_e is the Henry linewidth enhancement factor. α_e accounts for variations in the refractive index caused by fluctuations in the electron density in the gain medium. In conventional diode lasers this tends to increase the linewidth but for QCLs the refractive index varies very little at the peak of the gain spectrum [54, 55].

Yamanishi *et al.* reformulated equation (1.3) in terms of the rate of processes occurring in a three-level system shown in figure 1.4 [56]. In this scheme N_i corresponds to the electron population in level i, P is the net rate of inflow and outflow of electrons, η to the coupling into level 3 and the various τ values are time constants for relaxation between levels. The equation for the linewidth now becomes:

$$\delta\omega = \frac{1}{4\pi} F_R \frac{N_3}{(N_3 - N_2)_{th}} \frac{(\hbar\omega)\gamma_{photon}^2}{P_{int}} \left(1 + \alpha_e^2\right), \tag{1.4}$$

where F_R is a factor due to spontaneous emission enhancement that is assumed to be 1, γ_{photon} is the photon decay rate, P_{int} is the internal power given by $P_{int} = \gamma_{photon}\hbar\omega N_{photon}$ and N_{photon} is the number of photons. This equation is applicable to DFB-QCLs but is not entirely so for EC systems as it takes no account of the mirror and grating reflectivities that lead to cavity losses [57]. By measuring the frequency noise spectral density, Bartalini *et al.* have shown that the intrinsic linewidth of a

QCL may be as low as a few hundred Hz [9, 58]. The intrinsic linewidth is however, broadened mainly by current noise and both DFB and EC-QCLs have been reported with measured linewidths of a few MHz [59–62]. A measurement of the linewidth of a DFB-QCL will be detailed in chapter 3 using Lamb dip spectroscopy.

1.2 Coherent Excitation Processes

The absorption of (near) resonant incoherent light by a sample of gas should be treated according to Einstein's equations for absorption and emission [63]. Assuming that the radiation intensity is large enough that spontaneous emission may be neglected, then the population in the excited state P_1, is given by

$$P_1(t) = \frac{1}{2}\left(1 - e^{-BF(t)}\right), \tag{1.5}$$

where $F(t) = \int_{-\infty}^{t} I(t')dt'$ is the radiation fluence (energy per unit area) up until time t, I is the time varying radiation intensity and B is the Einstein coefficient. This shows that as time passes the amount of population excited into the upper state monotonically approaches 50% as shown in figure 1.5. If the incoherent source is replaced with a coherent light source then the system instead oscillates between the ground and upper state. The population in the upper state is now given by

$$P_1(t) = \frac{1}{2}\left(1 - \cos\Omega t\right), \tag{1.6}$$

where $\Omega = \frac{\mu E}{\hbar}$ is the Rabi frequency [64] with μ being the transition dipole moment and E the electric field. As is shown in figure 1.5 the population now oscillates between 0 and 1. Application of the coherent radiation for the appropriate length of time (Ωt equal to odd multiples of π) results in complete population inversion. These so-called π-pulses are however, very difficult to achieve in real systems due to phase fluctuations and so other methods for achieving state preparation with population inversion, by evolving the population adiabatically (see figure 1.5) are

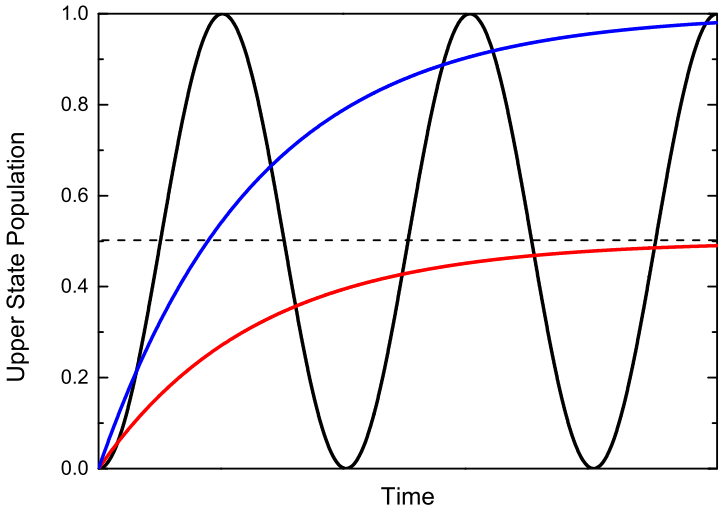

Figure 1.5: A comparison of the population transfer to the excited state $P_1(t)$, in the three types of excitation. Incoherent excitation (red) results in the populations of the excited state monotonically approaching 50%. Coherent excitation (black) results in the population oscillating between the excited and ground states and adiabatic passage (blue) results in complete population inversion.

sought.

Adiabatic rapid passage (ARP) in which the frequency of a laser is swept through a molecular resonance on a time scale that is fast compared to the collisionally induced polarisation dephasing, is an established method of preparing molecules in selected excited states [65]. Initially however, the necessary tunability was not available from the high power lasers required to conduct ARP. Therefore techniques such as Stark Chirped Adiabatic Rapid Passage (SCARP) in which the resonant frequency of the molecular sample is swept via the Stark effect using an applied electric field were developed [66, 67]. Another population transfer method involved crossing a fixed frequency laser beam with a molecular beam with the laser beam focused off the molecular beam axis [68, 69]. In this case the molecules experience a curved wavefront that appears as a time varying Doppler shift and thus achieves the tuning required for adiabatic rapid passage. With the laser beam fixed on the molecular beam axis the molecules experience a flat wavefront and Rabi oscillations (whereby the population oscillated between the ground and excited state as shown

in figure 1.5) are observed [70]. Hamadani *et al.* achieved adiabatic rapid passage by sweeping the frequency of an N_2O laser through the $\nu_2\,[asQ(8,7)]$ transition in NH_3. The tuning conditions required for ARP to occur were eased by utilising counter-propagating laser beams to give a sub-Doppler resonance [71].

Another approach for achieving population transfer into an excited state involves the incorporation of a third state and two lasers, pulsed in a counter-intuitive ordering in a process called Stimulated Raman Adiabatic Passage (STIRAP) [72,73]. The theory of STIRAP will be presented in chapter 2 and later on the measured properties of our lasers will be used in simulations to calculate the population transfer possible using STIRAP on nitric oxide using two QCLs (see chapter 5). It is shown that cw quantum cascade lasers open up the possibility for coherent rovibrational state preparation of gas phase molecules in low frequency vibrational modes.

The adiabatic limit requires that the ratio of the laser tuning rate k, to the square of the Rabi frequency (known as the β-parameter) be less than or equal to 1. For $\beta = \frac{k}{\Omega^2} \gg 1$ the passage is non-adiabatic, leading to minimal population transfer, and is known simply as rapid passage (RP). The tunability and high output powers produced by QCLs make them ideal laser sources for studying RP in ro-vibrational systems absorbing in the mid-IR and it is in this regime, using pulsed devices that most coherent transient studies using QCLs have been conducted. For pulsed QCLs application of a current pulse to the laser results in rapid Joule heating causing a fast frequency down chirp in the laser output, typically in the range 5 - 250 MHz ns^{-1}. The resulting high chirp rate may mean that the laser is swept through a spectroscopic resonance in a sample of low pressure gas in a time that is short compared to the that for collisionally induced polarization dephasing leading to rapid passage effects which appear as oscillations in the measured spectrum [74–76].

A qualitative explanation of the structure of RP signals would be to say that the macroscopic polarisation of the sample that has been created by an intense coherent laser beam beats with the frequency chirped electric field of that beam. The result is that the measured intensity of the beam oscillates due to constructive

and destructive interference. The oscillations are damped out by the processes that destroy the macroscopic polarisation of the sample, chiefly collisional dephasing even in a low pressure gas. Provided that the laser frequency is chirped through resonance on a time scale that is rapid compared to the dephasing time, and that the detector/amplifier system has sufficient bandwidth to resolve the high oscillation frequency, RP oscillations will be observed post resonance (in time).

With the increase in availability and power of room temperature cw QCLs, the same effects may be observed by applying a waveform to the laser to scan its frequency. The frequency scan rate may easily be changed by altering either the frequency or magnitude of the waveform. Rapid passage has been observed using a single laser setup over a long path length using OCS gas and a single mode QCL operating at 10 µm [77], and using two cw QCLs in a pump-probe type setup [78]. Other coherent effects may also be seen with rapidly chirped cw QCLs such as the electric field induced Autler-Townes splitting (also known as the AC Stark effect [79]) seen by Duxbury *et al.* [80,81]. In this case the splitting, observed in a low pressure sample sample of NO over a path length of 100 m, was found to be chirp rate dependent. These types of coherent effects lead to non-linear optical responses and such processes are generally modelled using the optical Bloch equations. These are the optical analogues of the original Bloch equations which describe the time evolution of the nuclear magnetisation in NMR [82]. The Bloch equations will be introduced in chapter 2, in which they will be derived from the density matrix describing the interaction of a two level system with radiation and they will be used in later chapters to simulate coherent transient experimental measurements.

1.3 Thesis Overview

Coherent spectroscopy is investigated throughout this thesis with particular attention given to high resolution sub-Doppler velocity selection. In chapter 2 the theory underpinning the types of spectroscopy employed in the thesis will be discussed. This will include density matrix calculations for two level systems coherently ex-

cited by a photon and the extension of the density matrix formalism to a three level system coupled by two photons. These equations underpin the phenomena seen throughout much of the rest of the thesis.

In chapter 3 a DFB-QCL is characterised, with its electrical and optical properties investigated. This laser is then used to perform both direct and sub-Doppler resolution spectroscopy on NO, the spectroscopic properties of which are explained in the chapter. The non-linear effect of saturation in the presence of a strong driving laser field is investigated and utilised in order to measure the laser linewidth via Lamb dip spectroscopy. Evidence of adiabatic rapid passage will be presented with line shape of the Lamb dip changing markedly as the rate of laser frequency scan is increased. Rapid passage oscillations are seen as the laser scan rate is increased even further and the optical Bloch equations will be used to model this transient non-linear behaviour.

Chapter 4 presents experiments in which both a DFB-QCL and an EC-QCL are used in pump-probe type experiments. These experiments are shown to be highly velocity selective and the data once again shows RP oscillations, even at relatively slow chirp rates. The effect of altering both the chirp rate and the total pressure will be presented and evidence of velocity redistribution will be shown. The linewidth broadening properties of a radio frequency noise source will be used to remove the coherence, demonstrating the high level of velocity selectivity available from the narrow linewidth QCLs and the importance of velocity dephasing in these studies. A two-colour polarisation spectroscopy experiment will also be presented with the measured signals able to provide both the absorption and the dispersion directly. Finally, simulations based on the three-level density matrix will be used to model the behaviour of the system.

Chapter 5 details experiments in which two lasers were again used, but now with one being amplitude modulated. Pump-probe studies will be presented in which the pump laser is amplitude modulated using an acousto-optic modulator to give a defined switch off time, allowing us to study the temporal dependence of

the combined population and polarisation relaxation. The properties of the lasers measured in the previous chapters are then used in calculations of the theoretical population transfer achievable using STIRAP. Simulations using a simple three-level model will be shown and compared with an extended simulation that takes account of the Zeeman coherences between M_J levels of the system. The simulation program is shown to provide much useful information about the optimal conditions for high population transfer and to provide information about the macroscopic polarisation alignment of the resulting excited molecules. The thesis concludes with experiments that attempt to stabilise the frequency output of the EC-QCL and suggestions for future experimental work in this area.

Chapter 2

Theory of Nonlinear Optics

Many of the experiments detailed in this thesis result in spectra which deviate from the standard linear absorption lineshapes $A(\nu)$, given by the Beer-Lambert law

$$A(\nu) = -\ln\left(\frac{I(\nu)}{I_0(\nu)}\right) = \sigma(\nu)lN = \alpha(\nu)l, \tag{2.1}$$

where $I(\nu)$ is the measured intensity of light passing through the sample, $I_0(\nu)$ is the intensity in the absence of absorbing species, l is the path length, N is the number density of the absorbers, $\sigma(\nu)$ is the frequency (ν) dependent absorption cross section, $\alpha(\nu)$ is the absorption coefficient and l is the path length. This chapter details the theoretical framework used to analyse and model this non-linear behaviour in the experimental data presented in later chapters. In the first instance the mechanisms leading to the broadening of spectral lines will be presented followed by the theory behind saturation spectroscopy, the method used in chapter 3 to measure the linewidth of a DFB-QCL. The theory of polarisation spectroscopy which provides a Doppler-free spectrum will also be detailed with experiments utilising this technique described in chapter 4. The next part of this chapter will then focus on a density matrix treatment of coherence in a two-level system coupled by the electric field of a laser. The density matrix treatment will be used to derive the optical Bloch equations which will be used in chapter 3 to model rapid passage signals originating from a velocity selected subset of an optically saturated gas sample. Finally the

density matrix treatment is extended to cover three-level systems coupled by two fields, with the theory being used in chapter 4 to model the rapid passage behaviour observed in a pump-probe type experiment and in chapter 5 to simulate, using properties of the system measured in the previous chapters, the population transfer technique known as STIRAP.

2.1 Line Broadening Mechanisms

To a crude first approximation, absorption of a photon occurs at a single frequency that corresponds to the energy difference between two energy levels in the molecule under study. However several mechanisms exist that broaden the frequency distribution over which the molecules absorb. These encompass homogeneous broadening, whereby all the molecules are affected to the same extent and results in a Lorentzian lineshape, and inhomogeneous broadening mechanisms in which each molecule is differently affected, resulting in a Gaussian lineshape. When multiple broadening mechanisms are in effect the resulting lineshape is a convolution of the constituent Lorentzian and Gaussian lineshapes that results in a Voigt profile [83]. In cases where the mean free path of the molecules is shorter than the emission wavelength, the molecules undergo several collisions during the emission process, changing velocity with each collision. This causes an averaging effect over the Doppler states of the molecule resulting in a narrowing of the line profile [84] and resulting in a Voigt fit underestimating the data at the line centre and at the wings. In these cases, more advanced line profiles are used to fit the spectra, the Galatry profile [85] assumes soft collisions between molecules, whereas the Rautian profile [86] assumes hard collisions. Both Galatry and Rautian profiles contain relaxation coefficients that depend on velocity changing collisions. Another advanced lineshape model that includes relaxation coefficients based on speed dependent effects is the speed-dependent Voigt profile [87]. All three are commonly used in high pressure spectroscopy to account for the change in lineshape due to collisional narrowing. At the low pressures used in the experiments presented in this thesis however, these line profiles are not necessary.

2.1.1 Doppler broadening

A ubiquitous phenomenon in gas phase absorption spectroscopy is the shift in the resonant frequency caused by the Doppler effect. The molecules in a gaseous sample have a distribution of velocities $f(v)$, given by the Maxwell-Boltzmann distribution

$$f(v) = \left(\frac{m}{2\pi k_B T}\right)^{\frac{3}{2}} 4\pi v^2 e^{\frac{-mv^2}{2k_B T}}, \tag{2.2}$$

determined by the particle mass m and the temperature T. A molecule that is moving in the direction of propagation of the incident radiation 'sees' a lower frequency of radiation than a stationary observer and so absorbs at a higher frequency according to that observer and appears blue shifted. Likewise a molecule moving opposite to the direction of propagation will see a higher frequency and appear red shifted. To the observer the molecules appear to absorb at the following frequency

$$\nu = \frac{\nu_0}{1 \pm \frac{v}{c}}, \tag{2.3}$$

where positive velocity corresponds to a red shift and negative velocity to a blue shift. The intensity of the measured absorption for a particular molecular velocity is hence proportional to the probability of finding the molecule at that velocity. The only component of the molecular velocity that adds to the Doppler broadening is the component along the direction of propagation of the incident radiation which leads to the following frequency distribution $f(\nu)$,

$$f(\nu) = \sqrt{\frac{mc^2}{2\pi k_B T \nu_0^2}}\, e^{-\frac{mc^2(\nu-\nu_0)^2}{2k_B T \nu_0^2}}. \tag{2.4}$$

We recognise this as a Gaussian function centred on the resonant frequency ν_0, which has a full width at half maximum of

$$\Delta\nu_{FWHM} = \nu_0 \sqrt{\frac{8k_B T \ln 2}{mc^2}}. \tag{2.5}$$

Doppler broadening is inhomogeneous as each molecule adds to the broadening independently. In nitric oxide as used in this thesis, the Doppler broadening at 300 K is typically of the order of 125 MHz ($0.0042\,\mathrm{cm}^{-1}$).

2.1.2 Lifetime Broadening

Even in the limit of no Doppler broadening an absorption line cannot be infinitely narrow (*ie.* a delta function). Heisenberg's uncertainty principle relates the uncertainty in the energy of a system to its finite lifetime τ,

$$\Delta E\tau \geq \hbar. \tag{2.6}$$

An excited state, populated to a greater extent than in the Boltzmann distribution, decays at a rate given by

$$\frac{dN_i}{dt} = -kN_i, \tag{2.7}$$

where N_i is the number of molecules in level i. The lifetime τ is given by the reciprocal of the rate constant k and leads to a natural linewidth of $\Delta\nu$,

$$\Delta\nu = \frac{1}{2\pi\tau}. \tag{2.8}$$

This natural broadening is homogeneous in nature as every molecule is affected identically and leads to a Lorentzian line profile given by

$$I(\nu) \propto \frac{1}{\pi}\frac{\frac{\gamma}{2}}{\left(\nu-\nu_0\right)^2 + \left(\frac{\gamma}{2}\right)^2}, \tag{2.9}$$

where $\gamma = \Delta\nu$. For the nitric oxide molecule, the lifetime of the excited state is of the order of 10^{-1} s, leading to lifetime broadening of order Hz.

2.1.3 Pressure Broadening

In a gaseous sample molecules are free to move about and collide with one another. These collisions result in an a loss of coherence between the laser and the transition dipole which also leads to a broadening of spectral lines. In this case the rate is determined by the collision frequency which is proportional to the pressure. Again the broadening is homogeneous and produces a Lorentzian lineshape given by equation (2.9) with a typical half-width (for NO) of $0.06\,\mathrm{cm}^{-1}\mathrm{atm}^{-1}$. The collisional processes may also lead to a small pressure dependent shift in the centre frequency of the absorption line (typically an order of magnitude less than the broadening). Since the coherent effects studied in this thesis are quickly damped out by high pressures, the experiments presented all utilise low gas pressures (generally « 1 Torr) and as such the pressure shifts and broadening are not a concern.

2.1.4 Transit-Time Broadening

For experiments involving transitions for which the spontaneous lifetimes are long compared to the interaction time of the molecules with the radiation field, the Doppler-free linewidth is limited by the interaction time. For a molecule that traverses a laser beam the interaction time T, is determined by the radius r, of the laser beam, and the mean thermal velocity v of the molecules,

$$T = \frac{2r}{v}. \tag{2.10}$$

Transit time broadening is inhomogeneous for the same reason that Doppler broadening is, *ie.* because each molecule has a different velocity and thus a different contribution to the broadening. For a laser beam that has a Gaussian intensity profile the resulting transit time broadening also results in a Gaussian profile

$$I(\omega) = I_0 e^{-\frac{(\omega-\omega_0)^2 r^2}{2v^2}}, \tag{2.11}$$

which has a full width at half maximum of $\delta\omega = \frac{2v}{r}\sqrt{2\ln 2}$. The transit time broadening for NO at 300 K through a beam with a radius of 2 mm is 263 kHz (8.8×10^{-6} cm^{-6}).

2.2 Saturation Spectroscopy

A shown by the previous discussion, in a gaseous sample Doppler broadening is by far the largest contribution to the broadening of the absorption lines at room temperature. For transitions which are close together in frequency space as often found in cases such as hyperfine splitting, this broadening often means that the individual transitions cannot be distinguished. One solution which allows the observation of hyperfine structure is obviously to cool the sample down to the point where the Doppler broadening is less than the splitting but another, often far more practical solution, is to use saturation spectroscopy.

2.2.1 Saturation of an Absorption Line

The Beer-Lambert law (2.1) applies under conditions of low incident radiation power such that the populations of the energy levels are essentially unchanged and the absorbed power is linearly proportional to the incident power. With laser sources however it is possible to achieve radiation intensities at which the population difference is no longer independent of the intensity. In these cases significant deviations from the Beer-Lambert law are observed and the absorption is said to become non-linear.

The absorbed power dP is related to the population difference $\Delta N = N_2 - N_1$ between the two levels within the volume Adz by

$$dP = AdzI\sigma\Delta N, \tag{2.12}$$

where I is the incident laser intensity and σ is the absorption cross section. Taking into account the rates of induced absorption and emission and the rates of decay of the two states in an open system (one in which the states under investigation

may lose energy to levels that are not pumped by the incident radiation) gives the following expression for the population difference [88]

$$\Delta N = \frac{\Delta N_0}{1+S}, \tag{2.13}$$

in which ΔN_0 is the population difference in the absence of the radiation field and S is known as the saturation parameter which is given by

$$S = \frac{2B_{12}\rho\left(\omega_{12}\right)}{R_1 + R_2}. \tag{2.14}$$

Here the optical density is denoted by $\rho\left(\omega_{12}\right)$ and the product with the Einstein coefficient B_{12} gives the absorption rate. R_1 and R_2 represent the total relaxation rates of the two states which include spontaneous emission. Physically then, the saturation parameter represents the ratio of the pumping rate to the relaxation rate. In the case of an upper state which relaxes only by spontaneous emission we have $R_1 = 0$ and $R_2 = A_{12}$ where A_{12} is the Einstein coefficient for spontaneous emission. For a monochromatic radiation source of intensity $I(\omega)$, the saturation parameter may now be written as

$$S = \frac{2\sigma_{12}I\left(\omega\right)}{\hbar\omega A_{12}}. \tag{2.15}$$

As mentioned previously the transitions are subject to broadening and so the saturation parameter has a frequency dependence which has a Lorentzian distribution given by

$$S_\omega = S_0 \frac{\frac{\gamma}{2}^2}{\left(\omega-\omega_0\right)^2 + \left(\frac{\gamma}{2}\right)^2}. \tag{2.16}$$

Here S_0 is the saturation parameter on resonance $S\left(\omega=\omega_0\right)$ and γ is the relaxation rate of the system. Having introduced the idea that the measured absorption may be decreased in the presence of a strong saturating field, we now introduce the concept of hole burning.

2.2.2 Hole Burning

A monochromatic wave that passes through a Doppler broadened gaseous sample is absorbed by molecules with velocity components such that the Doppler shifted frequency of the radiation in the molecular reference frame falls within the homogeneously broadened linewidth of the molecule. The absorption cross section for molecules with velocity component v_z in the direction of propagation of the radiation and wavevector $k = k_z$ is

$$\sigma_{12}(\omega, v_z) = \sigma_0 \frac{\left(\frac{\gamma}{2}\right)^2}{(\omega - \omega_0 - kv_z)^2 + \left(\frac{\gamma}{2}\right)^2}, \tag{2.17}$$

where the cross section at the line centre is given by σ_0.

Saturation causes the population in the lower state to be depleted in the velocity interval $dv_z = \frac{\gamma}{k}$ and the population in the upper state to be correspondingly increased. The population densities N_1 and N_2 of the lower and excited states are given by

$$N_1(\omega, v_z) = N_{1,0}(v_z) - \frac{\Delta N_0}{\gamma_1 \tau}\left[\frac{S_0\left(\frac{\gamma}{2}\right)^2}{(\omega - \omega_0 - kv_z)^2 + \left(\frac{\gamma_s}{2}\right)^2}\right], \tag{2.18a}$$

$$N_2(\omega, v_z) = N_{2,0}(v_z) + \frac{\Delta N_0}{\gamma_2 \tau}\left[\frac{S_0\left(\frac{\gamma}{2}\right)^2}{(\omega - \omega_0 - kv_z)^2 + \left(\frac{\gamma_s}{2}\right)^2}\right], \tag{2.18b}$$

and illustrated in figure 2.1, where $\gamma = \gamma_1 + \gamma_2$ is the sum of the homogeneous linewidths of the two states and represents the homogeneous linewidth of the transition. The saturated linewidth is $\gamma_s = \gamma\sqrt{1 + S_0}$ and the longitudinal relaxation time τ is given by

$$\tau = \frac{1}{\gamma_1} + \frac{1}{\gamma_2}. \tag{2.19}$$

The population difference with a saturating electric field is now given by

$$\Delta N(\omega, v_z) = N_0(v_z)\left[1 - \frac{S_0\left(\frac{\gamma}{2}\right)^2}{(\omega - \omega_0 - kv_z)^2 + \left(\frac{\gamma_s}{2}\right)^2}\right]. \tag{2.20}$$

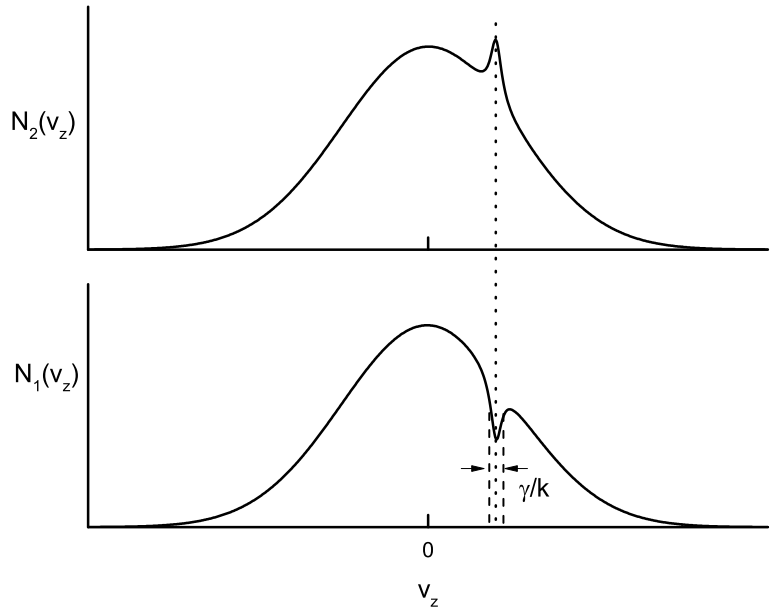

Figure 2.1: The Bennett hole burnt into the population of the initial state N_1, and the simultaneous increase in the population N_2 of the excited state for a pump laser emitting radiation at the frequency $\omega = \omega_0 + kv_z$.

This represents the underlying Gaussian velocity distribution $\Delta N(v_z)$ but with a velocity selective minimum at $v_z = (\omega - \omega_0)/k$ which is known as a Bennett hole. The width of the Bennett hole is the saturated linewidth γ_s and the depth of the hole at the line centre ($\omega = \omega_0 + kv_z$) is given by

$$\Delta N_0 (v_z) - \Delta N (v_z) = \Delta N_0 (v_z) \frac{S_0}{1 + S_0}. \tag{2.21}$$

Tuning the laser through the Doppler profile of an absorption feature will not allow one to view a Bennett hole since holes will be burnt into successive velocity groups such that the observed profile simply shows a reduced absorption compared with a non-saturating field. The absorption coefficient in this case is decreased by the factor $\sqrt{1 + S_0}$ giving

$$\alpha (\omega) = \frac{\alpha_0 (\omega)}{\sqrt{1 + S_0}}, \tag{2.22}$$

where α_0 is the unsaturated absorption coefficient. It is clear from equations (2.15) and (2.22) that as the radiation intensity increases, so the absorption coefficient

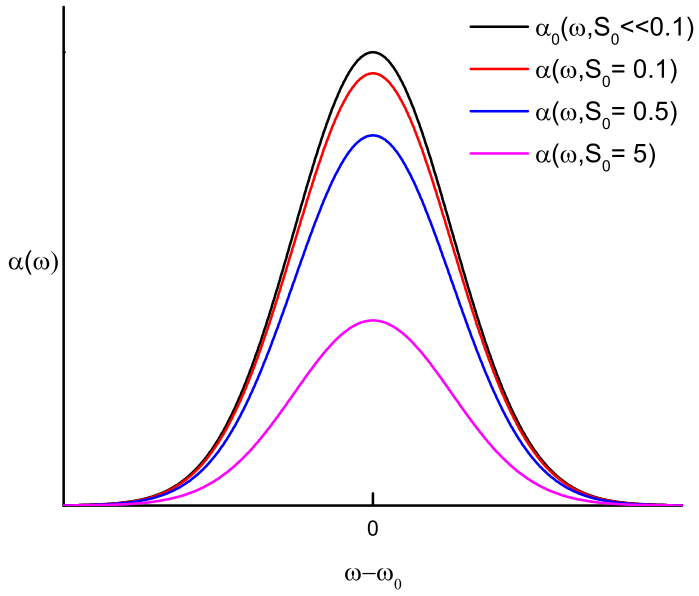

Figure 2.2: The effect of increasing the saturation parameter S_0 by increasing the laser intensity, is to decrease the absorption coefficient $\alpha(\omega)$.

decreases as demonstrated in figure 2.2. The more population that is pumped into the excited state, the less radiation power that is absorbed and hence the smaller the absorption becomes. In the extreme case where the populations in the lower and excited states are equal, then $\Delta N = 0$ and the sample becomes optically transparent to the pumping frequency [89].

2.2.3 Lamb Dip Spectroscopy

While it is not possible to observe a Bennett hole using a single laser beam, it is possible if two beams are used. In this case the saturating beam burns a hole in the velocity group at frequency $\omega_s = \omega_0 + kv_z$ and then a weak probe beam is tuned across the Doppler profile of the absorption feature. The weak probe observes an unsaturated absorption profile for all frequencies except the saturated group, where a dip in the absorption is seen. The absorption coefficient then becomes

$$\alpha_s = \alpha_0(\omega)\left[1 - \frac{S_0}{\sqrt{1+S_0}}\frac{\left(\frac{\gamma}{2}\right)^2}{(\omega-\omega_s)^2 + \left(\frac{\Gamma_s}{2}\right)^2}\right], \tag{2.23}$$

where $\Gamma_s = \gamma + \gamma_s = \gamma\left(1 + \sqrt{1 + S_0}\right)$ is the halfwidth of the absorption dip which is centred at $\omega = \omega_s$.

The saturating 'pump' beam and the weak 'probe' beam may be generated by separate lasers, but a special case exists where a single laser beam is passed through the sample and then retroreflected, forming both pump and probe beam functions simultaneously. In this case the pump and probe beams are tuned simultaneously but as they propagate through the gas in opposite directions they interact with mirror image velocity subsets $\pm v_z$ within the Doppler profile. The only time that the two beams interact with the same velocity subset is at $v_z = 0$, *i.e.* at the line centre. The Bennett hole observed in this case is known as a Lamb dip. [90] For a strong pump field the absorption coefficient of a weak probe can be written (neglecting coherence effects) as [91]

$$\alpha(\omega) = \alpha_0(\omega)\left[1 - \left(1 - \frac{1}{\sqrt{1 + S_0}}\right)\frac{\Gamma^2}{\Gamma^2 + (\omega - \omega_0)^2}\right]. \tag{2.24}$$

Equation 2.24 however, does not take account of the finite laser linewidth and so does not quite give the observed spectrum. The actual lineshape observed is the convolution of equation (2.24) with a function representing the laser linewidth. Mukherjee *et al.* give an analytical approximation to the convolution integral of the form [62]

$$\alpha(\omega) = \alpha_p\left[e^{-\left(\frac{\omega-\omega_0}{\Delta_D}\right)^2} - \frac{\sqrt{\pi}\,\Gamma}{\Delta_l}\left(1 - \frac{1}{\sqrt{1 + S_0}}\right)e^{-\left(\frac{\omega-\omega_0}{\Delta_l}\right)^2}\right], \tag{2.25}$$

where α_p is the maximum absorbance at the line centre, Δ_D is the Doppler width and Δ_l is the laser linewidth. This form assumes that the laser linewidth is greater than the homogeneous broadening of the transition and that the inhomogeneous Doppler broadening is also far greater than the homogeneous broadening such that the Doppler background is accurately approximated by the Gaussian function that is the first term in the square brackets. The Lamb dip technique may therefore be used to measure the linewidth of a laser where this linewidth is greater than the homogeneous broadening.

With Lamb dip spectroscopy the spectral resolution is limited only by the velocity selected linewidth of the Lamb dip rather than the much larger Doppler width. This allows the resolution of spectral features which are too close in transition energies to be resolved in the presence of Doppler broadening. For the investigation of coherent effects lamb dip spectroscopy also greatly increases the decoherence time as the velocity selected sample results in less averaging of the polarisation states than a Boltzmann distribution of velocities. This effect will be discussed further in chapter 3.

2.2.4 Polarisation Spectroscopy

Saturation or Lamb dip spectroscopy measures the change in the absorption caused by a saturating pump beam which significantly depletes the population in the absorbing energy level. Another way to remove the effects of Doppler broadening is to look instead at the change in the refractive index of the medium caused by optical pumping which alters the polarisation state. This is the principle behind polarisation spectroscopy (PS) which was first reported by Wieman and Hänsch in 1976 [92].

In polarisation spectroscopy the laser is split into a high power pump beam and a weak probe beam. The probe beam passes through a linear polariser before entering the sample cell. On exiting the sample cell the probe beam then passes through another polariser which is crossed with respect to the first. An unpumped gas sample contains an isotropic distribution of angular momenta so it has the same refractive index in all directions and the polarisation of the probe beam is unaffected by passing through the sample. A detector placed behind the second polariser thus sees only a very small signal determined by the finite extinction ratio of the polarisers, the birefringence of the optics in the beam path (including the cell windows) and spurious reflections.

In PS the pump beam is usually passed through a $\lambda/4$ plate to produce circularly polarised light before propagating through the sample cell in the opposite direction

to, and overlapping the probe beam. When tuned to a molecular transition the selection rules associated with the magnetic quantum number M are $\Delta M = +1$ for σ^+ polarised light and $\Delta M = -1$ for σ^- polarised light. The magnetic quantum number spans values from $-J$ to J, where J is the total angular momentum quantum number. For rovibrational transitions that involve a change in total angular momentum ($\Delta J = \pm 1$) it can be seen that a saturating pump beam that excites an appreciable population will produce an unequal distribution of population in the excited M sublevels. For example, for an R branch transition with $\Delta J = +1$, magnetic sublevels in the excited state corresponding to $M = -J$ are not populated and for a P transition with $\Delta J = -1$, magnetic sublevels in the excited state corresponding to $M = +J$ are not populated. This unequal population leads to an anisotropic distribution of the angular momentum vectors which in turn makes the gas birefringent.

The pump induced birefringence causes the linearly polarised probe beam to have its electric field vector rotated during its interaction with the sample gas, allowing some of the light to pass through the crossed analysis polariser onto the detector. The counter-propagating setup results in the polarisation signal being observed only at the line centre since as in Lamb dip spectroscopy, only at the line centre is the same velocity subset pumped and probed simultaneously. Furthermore, since it is only at the line centre that the probe beam sees an anisotropic distribution of the angular momentum vectors, the Doppler profile is cut out as the probe beam is not rotated and is thus blocked by the analysis polariser, *ie.* the lineshape is Doppler free.

The linearly polarised probe beam may be thought of as having both σ^+ and σ^- circularly polarised components and these two components experience different absorptions as they pass through the anisotropically pumped gas resulting in a rotation of the polarisation. The most general expression for the intensity I, of light transmitted to the detector after passing through a path length L is given by

$$I = 2I_0 e^{-\bar{\alpha}L} \left|\sin\theta\cos\phi + \cos\theta\sin\phi\right|^2, \tag{2.26}$$

where $\bar{\alpha} = \frac{\alpha^+ + \alpha^-}{2}$ is the average absorption coefficient seen by the σ^+ and σ^- components of the probe [88]. The uncrossing angle between the two polarisers is given by θ and takes values from 0 when the polarisers are fully crossed to 90° when they are aligned on the same axis. The term outside the modulus ($2I_0 e^{-\bar{\alpha}L}$) represents the Doppler background absorption. The complex phase factor ϕ is given by

$$\phi = \frac{1}{2}\left[\left(\Delta\alpha_0 L \frac{\frac{\gamma_s}{2}(\omega-\omega_0)}{\left(\frac{\gamma_s}{2}\right)^2 + (\omega-\omega_0)^2} + \Delta b_r\right) + i\left(\frac{\Delta\alpha_0 L}{2}\frac{\left(\frac{\gamma_s}{2}\right)^2}{\left(\frac{\gamma_s}{2}\right)^2 + (\omega-\omega_0)^2} + \Delta b_i\right)\right]. \tag{2.27}$$

Here the first term represents the optical birefringence $\Delta n = n^+ - n^-$, being the difference in the refractive index seen by the σ^+ and σ^- polarised components of the probe beam. The second term represents the circular dichroism $\Delta\alpha = \alpha^+ - \alpha^-$, being the difference in absorption coefficient experienced by the two polarisation components of the probe. The values Δb_r and Δb_i account for the birefringence and circular dichroism of the cell windows respectively. The first term has a Lorentzian dispersive dependence on the laser frequency, whereas the second has an absorptive dependence. For $\theta = 0$ the dispersion term vanishes and the only signal is from the remaining Lorentzian term.

Combining equations (2.26) and (2.27) gives the expected signal at the detector for all uncrossing angles. As an example, the polarisation spectrum for the $\mathrm{R}(13.5)_{\frac{1}{2}e}$ transition in NO has been simulated in figure 2.3 in which the background absorptions have been normalised to emphasise the lineshape changes. At small angles the dispersive term rises with a $\sin(2\theta)$ dependence and has its maximum at $\theta = 45°$, however the background term rises with $\sin^2\theta$ and dominates the dispersion signal except at small angles. Therefore the usual experimental setup involves finding a small uncrossing angle for which the dispersion signal is maximised while keeping the background small. Due to the vastly reduced background level afforded by the (nearly) crossed polarisers, the signal to noise ratio of polarisation spectroscopy is expected to be much better than that for standard saturation spectroscopy [93].

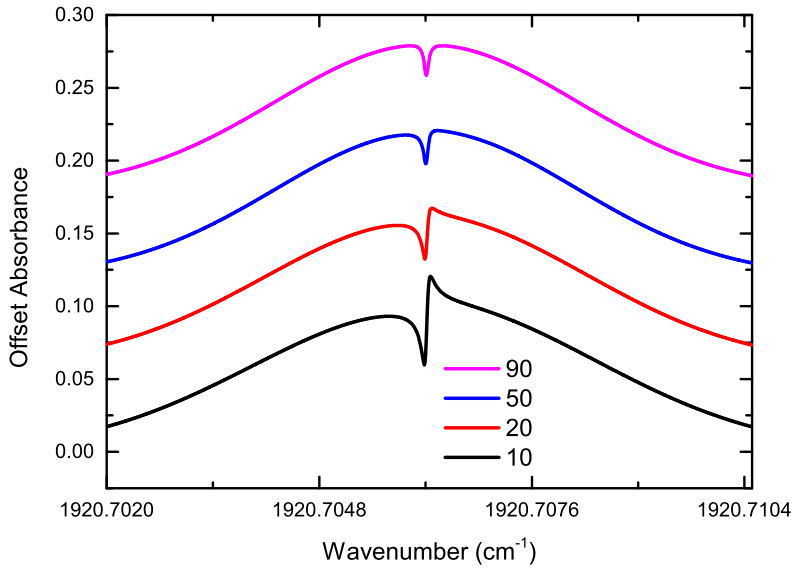

Figure 2.3: Simulations of the polarisation signal expected for various analysis polariser angles θ, on the $R(13.5)_{\frac{1}{2}}$ transition in NO. The signal amplitudes have been normalised and offset in order to clarify the lineshapes.

2.3 Two Level Density Matrix

We now move on to describe the density matrix formalism used to describe the processes that happen when light interacts with a two level system. The density matrix formalism is useful because it is easy to deal with resonance compared with perturbation theory, it provides a simple way to incorporate damping mechanisms and it allows us to deal with mixed rather than pure states [94].

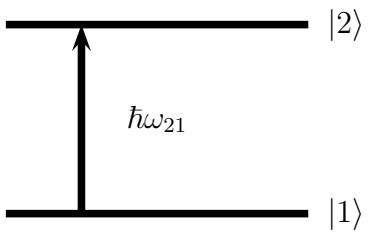

Figure 2.4: A two-level system excited by a resonant photon of energy $\hbar\omega_{21}$.

An ensemble of particles which may individually occupy pure states $|\psi_i\rangle$ with probability amplitudes p_i, and with $\sum_i p_i = 1$, together will form a mixed state

which cannot be described by a single wavefunction. In this case there exists the density operator $\hat{\rho}$, describing the statistical ensemble

$$\hat{\rho} = \sum_i p_i \left|\psi_i\right\rangle \left\langle\psi_i\right| . \tag{2.28}$$

The outer product, $\left|\psi\right\rangle \left\langle\psi\right|$ is a linear operator that maps one state onto another. By expressing the system in terms of a basis $\left|m\right\rangle$ the density matrix elements are then given by

$$\rho_{mn} = \sum_i p_i \left\langle m \right| \left.\psi_i\right\rangle \left\langle\psi_i\right| \left. n\right\rangle . \tag{2.29}$$

For our two level system, this has the form of

$$\rho = \begin{pmatrix} \rho_{11} & \rho_{12} \\ \rho_{21} & \rho_{22} \end{pmatrix} . \tag{2.30}$$

The diagonal elements ρ_{mm} of the density matrix represent the probabilities of finding the system in state $\left|m\right\rangle$ and have the property

$$\rho_{11} + \rho_{22} = 1, \tag{2.31}$$

ie. the trace of the density matrix is equal to 1. The off-diagonal elements represent the coherence between the two levels of the system. If the system occupies a pure state which may be written as a linear superposition of the basis states

$$\left|\psi\right\rangle = c_1 \left|1\right\rangle + c_2 \left|2\right\rangle , \tag{2.32}$$

then the resulting density matrix is given by the products of the basis state probability amplitudes, c_1 and c_2

$$\begin{pmatrix} \rho_{11} & \rho_{12} \\ \rho_{21} & \rho_{22} \end{pmatrix} = \begin{pmatrix} c_1 c_1^* & c_1 c_2^* \\ c_2 c_1^* & c_2 c_2^* \end{pmatrix} . \tag{2.33}$$

In this situation the coherences are non-zero, however if the system is in a mixed

state then the coherence terms are zero.

2.3.1 The Liouville or von Neumann Equation

The time evolution of an atomic or molecular wavefunction Ψ, is given by the time dependent Schrödinger equation

$$i\hbar\frac{\partial}{\partial t}\left|\Psi,t\right\rangle = \hat{H}\left|\Psi,t\right\rangle. \tag{2.34}$$

To derive the time evolution of the density matrix we start by differentiating the form given in equation 2.28 assuming time independent probability amplitudes

$$\frac{\partial}{\partial t}\rho = \sum_i p_i\left(\left|\psi_i\right\rangle\frac{\partial\left\langle\psi_i\right|}{\partial t} + \frac{\partial\left|\psi_i\right\rangle}{\partial t}\left\langle\psi_i\right|\right). \tag{2.35}$$

We identify

$$\frac{\partial\left|\psi_i\right\rangle}{\partial t} = -\frac{i}{\hbar}H\left|\psi_i\right\rangle \tag{2.36}$$

and

$$\frac{\partial\left\langle\psi_i\right|}{\partial t} = \frac{i}{\hbar}\left\langle\psi_i\right|H. \tag{2.37}$$

Substituting equations (2.36) and (2.37) into (2.35) we arrive at the Liouville-von Neumann equation

$$\dot{\rho} = -\frac{i}{\hbar}\left[H,\rho\right]. \tag{2.38}$$

The square brackets denote a commutator which for any two arbitrary operators $\hat{A}$ and $\hat{B}$ is defined as $\left[\hat{A},\hat{B}\right] = \hat{A}\hat{B} - \hat{B}\hat{A}$.

2.3.2 Hamiltonian with external field

The Hamiltonian for an atom or molecule interacting with light is given by the sum of the bare state Hamiltonian, $\hat{H}_0$ and the potential due to the electric field interaction $\hat{V}$,

$$\hat{H}(t) = \hat{H}_0 + \hat{V}(t). \tag{2.39}$$

The bare state Hamiltonian acts on the orthonormal basis states of the system to return the energies of the basis states as per the time-independent Schrödinger equation and is a diagonal matrix containing the energies of the orthonormal basis states:

$$\hat{H}_0 = \begin{pmatrix} \epsilon_1 & 0 \\ 0 & \epsilon_2 \end{pmatrix}. \tag{2.40}$$

We can subtract the lowest energy state from equation 2.40 to give the bare state Hamiltonian in terms of the energy differences or transition energies of the system

$$\hat{H}_0 = \begin{pmatrix} 0 & 0 \\ 0 & \epsilon_2 - \epsilon_0 \end{pmatrix} = \hbar \begin{pmatrix} 0 & 0 \\ 0 & \omega_{21} \end{pmatrix}, \tag{2.41}$$

where the transition energy $\epsilon_2 - \epsilon_1$ is given by the Bohr frequency $\Delta E = \hbar\omega$. Within the dipole approximation, which assumes that the electric field amplitude is essentially unchanging over the length of the atom or molecule, the electric field is written as

$$\vec{E} = E_0 \left(e^{-i\omega t} + e^{i\omega t} \right). \tag{2.42}$$

The electric field interaction term is given by the dot product of the electric dipole of the atom or molecule with the electric field of the incident light

$$\hat{V} = -\vec{\mu} \cdot \vec{E}, \tag{2.43}$$

where the transition dipole moment is a function of position multiplied by charge

$$\hat{\mu} = -q\hat{x} \tag{2.44}$$

with the elements of its matrix representation (in 1 dimension) given by

$$\mu_{ij} = -q \left\langle i \,|\, \hat{x} \,|\, j \right\rangle. \tag{2.45}$$

The position operator is linear with odd parity and may be written as the sum of outer products of the orthonormal basis states

$$\hat{x} = |1\rangle\langle 2| + |2\rangle\langle 1|. \tag{2.46}$$

The odd parity of $\hat{x}$ means that the diagonal matrix elements equal zero (due to symmetry) and so the transition dipole matrix is simply given by

$$\hat{\mu} = \mu_{12}|1\rangle\langle 2| + \mu_{21}|2\rangle\langle 1|. \tag{2.47}$$

Examining the components of equation (2.47), we see that the operator $|1\rangle\langle 2|$ maps state $|2\rangle$ onto $|1\rangle$ and so we refer to it as the annihilation operator. Likewise the operator $|2\rangle\langle 1|$ is the creation operator which maps state $|1\rangle$ onto $|2\rangle$. Combining equation (2.47) with (2.43) and (2.42) gives

$$\hat{V} = -\mu_{12}|1\rangle\langle 2| E_0\left(e^{-i\omega t} + e^{i\omega t}\right) - \mu_{21}|2\rangle\langle 1| E_0\left(e^{-i\omega t} + e^{i\omega t}\right). \tag{2.48}$$

2.3.3 Rotating Wave Approximation

Let us make a unitary transform to put the system into the interaction picture, in which the bare state Hamiltonian is zero. This transform is given by equation 2.49

$$U = e^{\frac{iH_0 t}{\hbar}} = \begin{pmatrix} 1 & 0 \\ 0 & e^{i\omega_{21}t} \end{pmatrix}. \tag{2.49}$$

This can be thought of as transforming to a reference frame that rotates at the transition frequency. Applying the same transform to the interaction term, equation (2.48), gives

$$\begin{aligned}\hat{V}_I = U\hat{V}U^\dagger = &-\mu_{12}E_0|1\rangle\langle 2|\left(e^{-i(\omega+\omega_{21})t} + e^{i(\omega-\omega_{21})t}\right) \\ &-\mu_{21}E_0|2\rangle\langle 1|\left(e^{-i(\omega-\omega_{21})t} + e^{i(\omega+\omega_{21})t}\right).\end{aligned}$$

Near resonance, $(\omega - \omega_{21}) \ll (\omega + \omega_{21})$ and the latter terms are considered to be rapidly oscillating, such that they average to zero over the shortest timescale of the system. We therefore make what is known as the rotating wave approximation by ignoring these rapidly oscillating terms. By making this approximation and transforming back into the Schrödinger picture we arrive at the following form of the interaction potential under the rotating wave approximation

$$\hat{V} = -\hbar\Omega^* \left|1\right\rangle \left\langle 2\right| e^{i\omega t} - \hbar\Omega \left|2\right\rangle \left\langle 1\right| e^{-i\omega t}, \tag{2.50}$$

where $\Omega = \frac{\mu_{21} E_0}{\hbar}$ is known as the Rabi frequency [64]. The rotating wave approximation is valid near resonance and in the weak interaction limit, where the Rabi frequency is much smaller than the transition frequency. The full Hamiltonian is now

$$\hat{H}_{RWA} = \hbar \begin{pmatrix} 0 & -\Omega e^{-i\omega t} \\ -\Omega^* e^{i\omega t} & \omega_{21} \end{pmatrix}. \tag{2.51}$$

We are able to remove all time-dependence from the Hamiltonian by making another transformation into a frame that rotates at the optical frequency ω. The transformation is given by

$$\hat{U} = e^{i\hat{H}_1 t} = \begin{pmatrix} 1 & 0 \\ 0 & e^{i\omega t} \end{pmatrix}, \tag{2.52}$$

and yields the time-independent form of the Hamiltonian given by

$$\hat{H}'_{RWA} = \hat{U}\left(\hat{H} - \hat{H}_1\right)\hat{U}^\dagger = -\hbar \begin{pmatrix} 0 & \Omega \\ \Omega^* & \Delta \end{pmatrix}, \tag{2.53}$$

where Δ is the detuning given by $\omega - \omega_{21}$. Clearly, the application of the rotating wave approximation greatly simplifies the form of the Hamiltonian, making it a time-independent function of the detuning and the Rabi frequency.

2.3.4 Optical Bloch equations

We are now in a position to find expressions for the time evolution of the density matrix elements by placing equation (2.30) and the Hamiltonian into the Liouville equation (2.38). Using the form of the Hamiltonian given by (2.53) gives

$$\dot{\rho}_{11} = i\left(\Omega\rho_{21} - \Omega^*\rho_{12}\right) \tag{2.54a}$$

$$\dot{\rho}_{22} = i\left(\Omega^*\rho_{12} - \Omega\rho_{21}\right) \tag{2.54b}$$

$$\dot{\rho}_{12} = i\Omega\left(\rho_{22} - \rho_{11}\right) - i\Delta\rho_{12} \tag{2.54c}$$

and constitutes one form of the optical Bloch equations, otherwise known as the Maxwell Bloch equations [82, 95, 96]. These were first derived for a spin $\frac{1}{2}$ system in NMR and later adapted to the optical regime [97, 98].

Making a change of variables to describe the system in terms of the real part of the coherence U, the imaginary part of the coherence V, and the population inversion W, allows a more insightful form of the equations which we can use to visualise the processes occurring. The transformation is given by

$$U = \rho_{21} + \rho_{12}, \tag{2.55a}$$

$$V = i\left(\rho_{21} - \rho_{12}\right), \tag{2.55b}$$

$$W = \rho_{22} - \rho_{11}, \tag{2.55c}$$

and yields the following equations of motion

$$\dot{U} = \Delta V, \tag{2.56a}$$

$$\dot{V} = 2\Omega W - \Delta U, \tag{2.56b}$$

$$\dot{W} = -2\Omega V. \tag{2.56c}$$

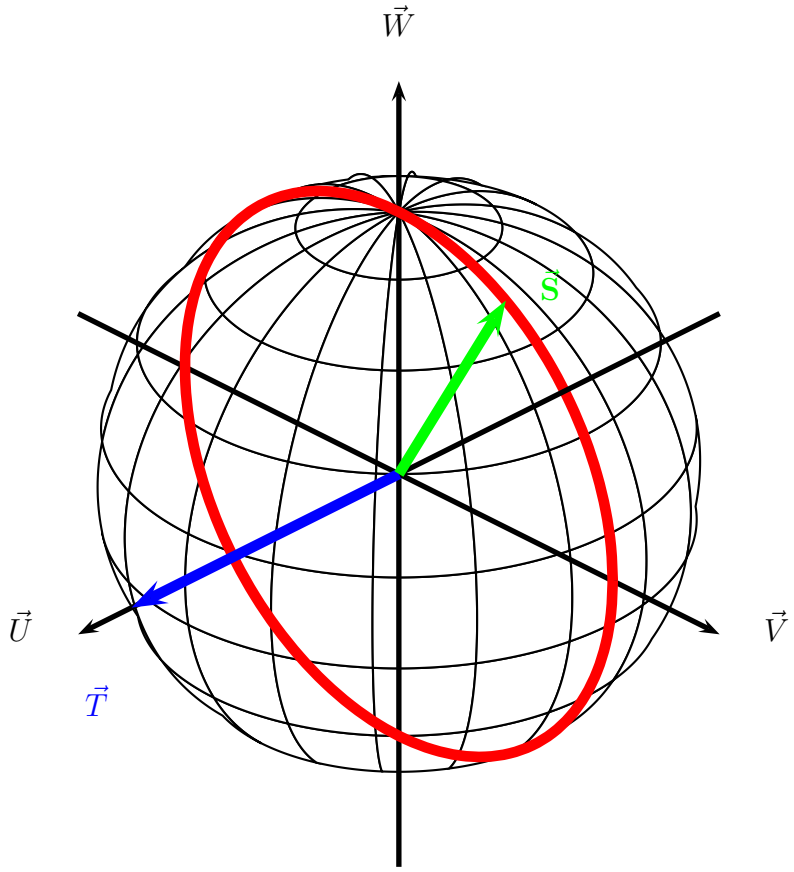

Figure 2.5: A schematic figure illustrating the Bloch sphere in the case of zero detuning. The pseudo-spin vector $\vec{S}$ precesses about the torque vector $\vec{T}$ and traces out a circle on the surface of the Bloch sphere in the V, W plane.

We see that the population inversion changes only due to the imaginary part of the coherence, V. Since this is associated with an energy change we therefore associate V with the absorptive part of the dipole moment and U with the dispersive part [99].

Let us define a vector $\vec{S} = U(t)\hat{x}+V(t)\hat{y}+W(t)\hat{z}$, which is called the 'pseudo-spin vector' due to the analogy with the spin-$\frac{1}{2}$ system seen in NMR. If we also define a 'torque vector', $\vec{T} = -\Omega\hat{x} - \Delta\hat{z}$, then we see that the equations of motion are given by the cross product

$$\dot{S} = \vec{T} \times \vec{S}. \tag{2.57}$$

The variables U, V, and W obey the conservation law $U^2 + V^2 + W^2 = 1$. This can be seen by noting that the time derivative of $U^2 + V^2 + W^2 = 1$ vanishes, and that in the absence of the driving field, with the system in its ground state $W = -1$ and $U = V = 0$ [100]. Thus we can visualise the solutions of equation

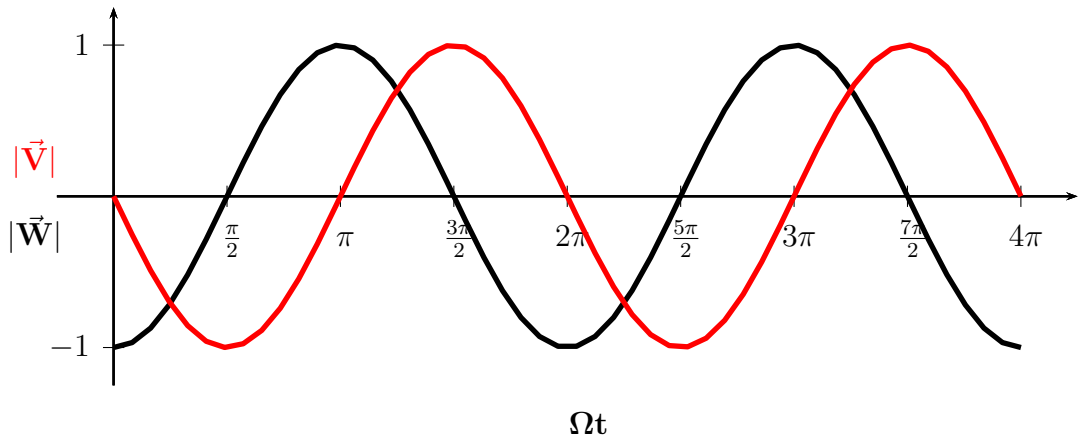

Figure 2.6: The time evolution of the population inversion W, and the absorptive part of the coherence V, for a two level system pumped at the resonant frequency. The population is seen to oscillate between the ground and excited states giving complete population inversion at certain times ($\Omega t = (2n+1)\pi$).

(2.57) occupying the surface of a sphere. The vector $\vec{S}$ precesses about $\vec{T}$ with an angular frequency equal to the magnitude of $\vec{T}$. In the case of zero detuning ($\Delta = 0$) this frequency is equal to the Rabi frequency Ω and we see that $\vec{S}$ traces out a circle on the surface of the Bloch sphere which lies in the V, W plane as shown in figure 2.5. This corresponds to the system population cycling between the ground and excited states and is known as Rabi cycling. The solution of equation (2.57) in the case of zero detuning is

$$U = 0,\ V = -\sin\Omega t,\ W = -\cos\Omega t, \tag{2.58}$$

solutions which are shown in figure 2.6. It may be noticed from figure 2.6 that the application of on-resonance radiation for a length of time corresponding to $\frac{\pi}{\Omega}$ will give complete population inversion. This is known as a π pulse. Similarly a $\frac{\pi}{2}$ pulse being a pulse with length $\frac{\pi}{2\Omega}$ results in an equal population in each of the two states.

In the case of non-zero detuning the solution for a system which starts in its ground state is given by Allen and Eberly as, [99]

$$W = -\frac{\Delta^2 + \Omega^2 \cos\sqrt{\Delta^2 + \Omega^2}t}{\Delta^2 + \Omega^2}. \tag{2.59}$$

The oscillations now happen at the generalised Rabi frequency $\Omega' = \sqrt{\Delta^2 + \Omega^2}$ and

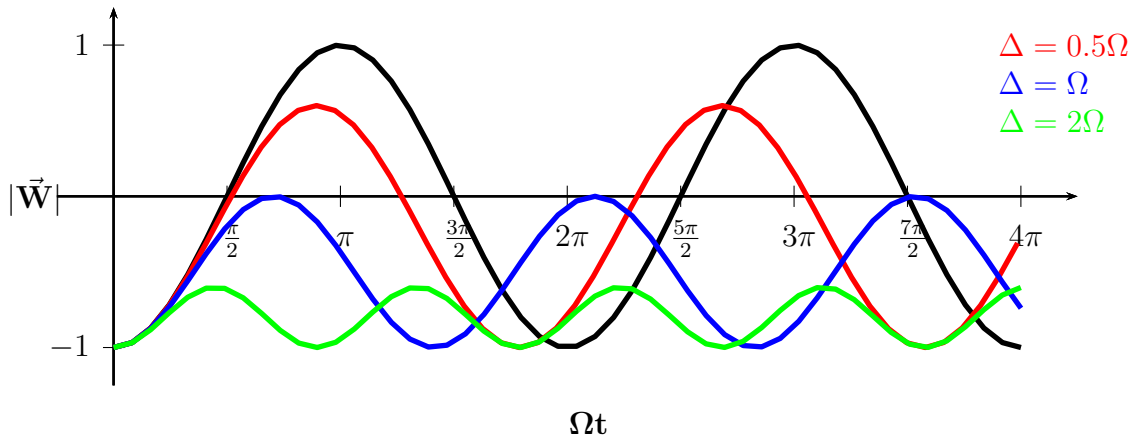

Figure 2.7: The time evolution of the population inversion W for various detunings Δ. As the detuning increases the oscillation frequency increases but the population transferred into the excited state decreases.

the population can no longer be fully inverted. The maximum population transferred into the upper state is limited by the detuning, with greater detunings resulting in smaller population transfer as shown in figure 2.7.

2.3.5 Decay processes

Until now we have considered the equations of motion in the absence of damping mechanisms. Clearly, in order to model real systems we must take account of the mechanisms by which those systems decay. The upper state is assumed to decay spontaneously back to the lower state with a lifetime given by T_1 such that all population will return to the ground state in the absence of an electromagnetic field. The dipole oscillations must also damp out once the field is turned off and do so with the lifetime T_2. This dephasing time is governed by incoherent interactions such as collisions. We now introduce these lifetimes as phenomenological decay constants into the density matrix equation of motion (2.38),

$$\dot{\rho} = -\frac{i}{\hbar}\left[\hat{H}, \rho\right] - (\Gamma\hat{\rho})\,, \tag{2.60}$$

where the matrix $(\Gamma\hat{\rho})$ gives the decay constants, [101]

$$\hat{\Gamma\rho} = \begin{pmatrix} \frac{-\rho_{11}}{T_1} & \frac{\rho_{12}}{T_2} \\ \frac{\rho_{21}}{T_2} & \frac{\rho_{22}}{T_1} \end{pmatrix}. \tag{2.61}$$

The equations of motion given in (2.54c) are thus modified to give

$$\dot{\rho}_{11} = i\left(\Omega\rho_{21} - \Omega^*\rho_{12}\right) + \frac{\rho_{11}}{T_1}, \tag{2.62a}$$

$$\dot{\rho}_{22} = i\left(\Omega^*\rho_{12} - \Omega\rho_{21}\right) - \frac{\rho_{22}}{T_1}, \tag{2.62b}$$

$$\dot{\rho}_{12} = i\Omega\left(\rho_{22} - \rho_{11}\right) - i\Delta\rho_{12} - \frac{\rho_{12}}{T_2}, \tag{2.62c}$$

and the alternative vector forms of the Bloch equations given by (2.56) become,

$$\dot{U} = \Delta V - \frac{U}{T_2}, \tag{2.63a}$$

$$\dot{V} = 2\Omega W - \Delta U - \frac{V}{T_2}, \tag{2.63b}$$

$$\dot{W} = -2\Omega V - \frac{(W+1)}{T_1}. \tag{2.63c}$$

2.3.6 Steady state solutions

In the limit where the relaxation is fast compared to the rate of change of the applied radiation frequency then a steady state is reached. By setting the time derivatives, equations (2.63) to zero and solving the resulting simultaneous equations we find the steady state solutions to the optical Bloch equations [99]

$$U(\infty, \Delta) = \frac{2\Delta\Omega T_2^2}{1 + \Delta^2 T_2^2 + 4T_1 T_2 \Omega^2}, \tag{2.64a}$$

$$V(\infty, \Delta) = -\frac{2\Omega T_2}{1 + \Delta^2 T_2^2 + 4T_1 T_2 \Omega^2}, \tag{2.64b}$$

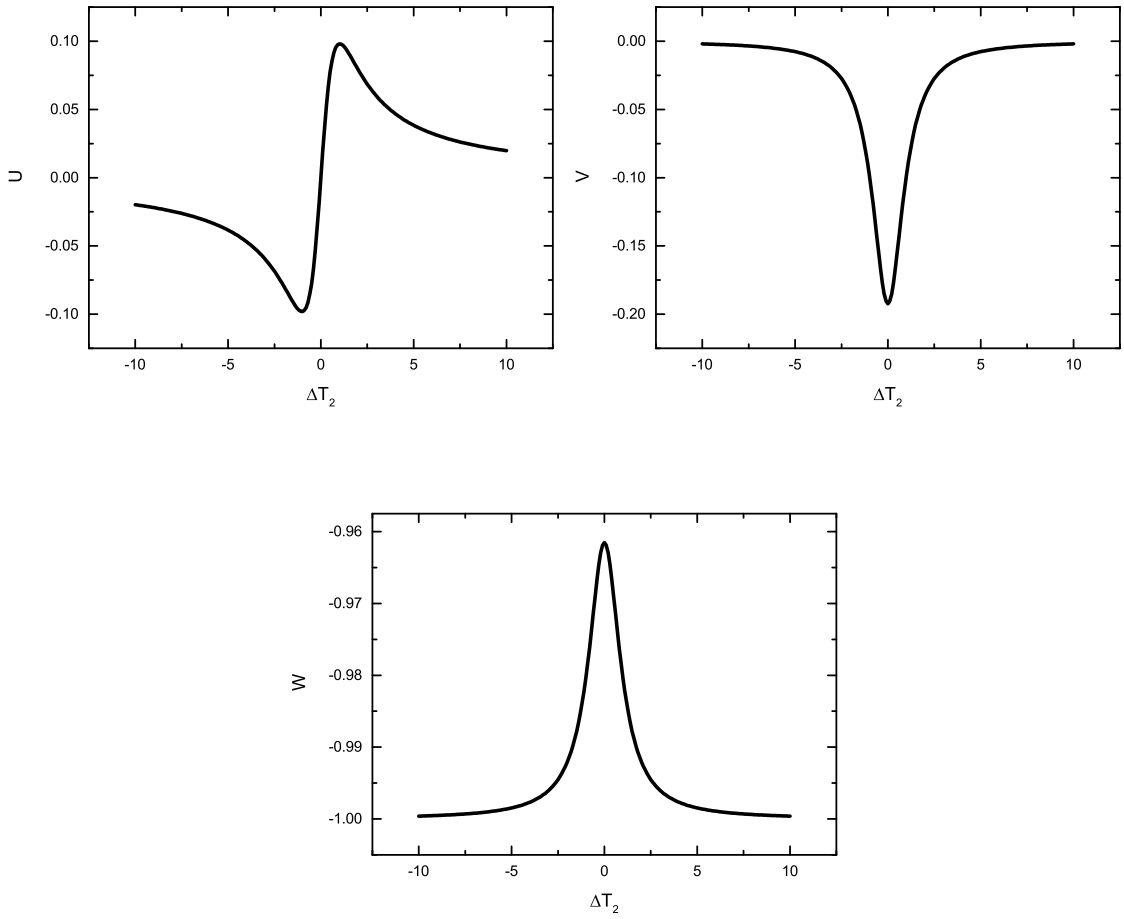

Figure 2.8: The steady state solutions to the optical Bloch equations as a function of detuning show the behaviour expected of an absorptive transition in the weak field limit. U gives a dispersive line shape with both V and W returning a Lorentzian absorptive line shape.

$$W(\infty, \Delta) = -\frac{1 + \Delta^2 T_2^2}{1 + \Delta^2 T_2^2 + 4T_1 T_2 \Omega^2}. \tag{2.64c}$$

These return the expected behaviour for linear absorption in the weak field limit when $\Omega^2 T_1 T_2 \ll 1$ with V and W returning Lorentzian lineshapes and U giving a dispersion type line shape as plotted in figure 2.8. It is notable from these solutions that in the steady state regime the inversion W, is always close to -1, *ie.* little population transfer occurs.

2.3.7 Optical Nutation and Free Induction Decay

We now consider the effect that Rabi cycling of the populations in the two states has on the driving field. As the population oscillates between the lower state, a coherent superposition state, the excited state and back down again, there is a resultant effect on the electric field which leads to amplitude modulation of the light. Initially as the inversion increases from -1 the light amplitude is decreased, corresponding to absorption. As the inversion reaches zero the gas becomes optically transparent and there is no change in amplitude from that entering the sample. Then as the population inversion increases further there is amplification of the light emitted. The amplitude modulation follows the oscillations in population and is termed optical nutation. The oscillations do not continue indefinitely but are damped out by the relaxation processes that give rise to the time constants T_1 and T_2 [102, 103].

If the molecules are exposed to a Stark field, which causes the resonance frequency to shift such that the pumped molecules are no longer close to resonance then the pumped molecules radiate at the sum of the optical frequency and the frequency of the Stark shift. The observed signal caused by this effect oscillates at a beat frequency equal to the Stark shift frequency, *i.e.* the difference between the laser and molecular radiation frequencies. This can be thought of as the interaction between a group of oscillating dipoles and the electric field of the laser beam which causes both constructive and destructive interference and so produces amplitude modulation of the detected signal. The oscillations decay due to the dephasing of the freely precessing dipoles which can take place on a much shorter time scale than population decay. This process is known as free induction decay or rapid passage [104]. With the advent of highly tunable lasers, the detuning from molecular resonance may be achieved simply by tuning the laser frequency. QCLs operating in both pulsed and continuous modes allow fast frequency tuning allowing rapid passage signals to be observed as in the seminal work of Duxbury *et. al.* [76, 105–107].

2.4 Density Matrix of a Three-Level System

For experiments involving three levels coupled by two monochromatic laser fields the density matrix formalism may be extended to reveal interesting new effects. Several types of three-level system exist: a Λ shaped system, a V shaped system and a ladder state system. These are shown in figure 2.9. For this thesis only the ladder

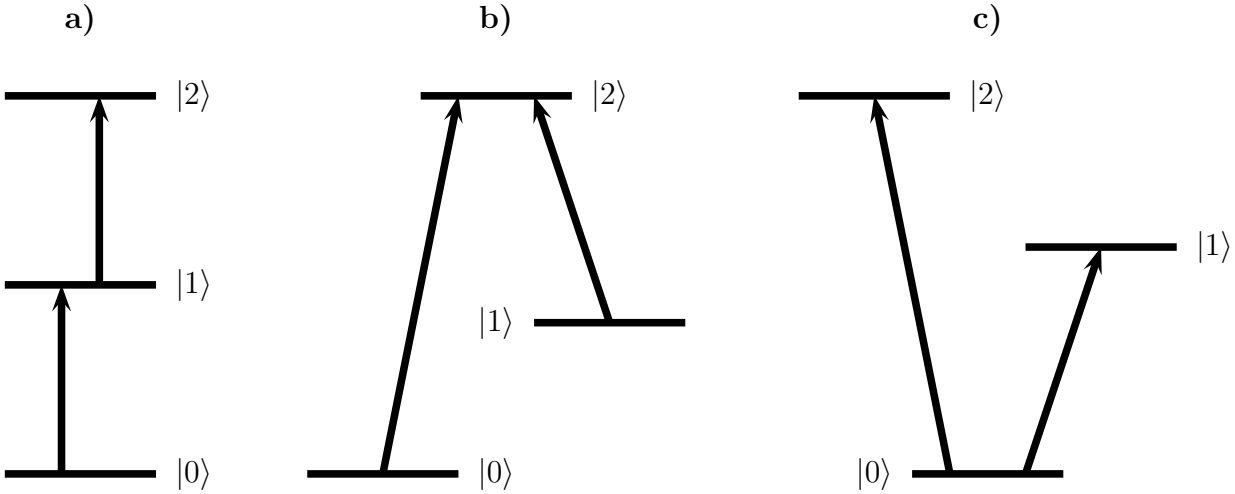

Figure 2.9: The three schemes by which three levels are coupled by two photons. a) A ladder state system, b) a Λ type system and c) a V shaped system. For this thesis only the ladder state system will be discussed in detail.

type system will be discussed. The ladder state system is an extension of the two level system studied previously in this chapter. Essentially it is two such systems added together, sharing a common state as the middle 'rung' of the ladder. The density matrix is now a 3×3 matrix of the same form as equation (2.30) and the time evolution is still given by equation (2.60).

The elements of the Hamiltonian for the three level system are derived in the same way as for the two level system including the rotating wave approximation. It is essentially the Hamiltonians of the two $2-$level systems placed into one 3×3 matrix; the overlap terms between the initial and final states $\hat{H}_{02} = \hat{H}_{20}$ are zero as they are linked only via the intermediate state. The Hamiltonian for the three level

ladder system is therefore given in the rotating wave approximation by

$$\hat{H} = -\hbar \begin{pmatrix} 0 & \Omega_{01} & 0 \\ \Omega_{10} & \Delta_{01} & \Omega_{12} \\ 0 & \Omega_{21} & \Delta_{01} + \Delta_{12} \end{pmatrix}, \tag{2.65}$$

where Ω_{01} is referred to as the pump Rabi frequency and Ω_{12} as the Stokes Rabi frequency. The detunings Δ are likewise referred to as the pump detuning (Δ_{01}) and the Stokes detuning (Δ_{12}) with the sum of the two being known as the two-photon detuning. The time evolution of the system is described by the following set of differential equations:

$$\dot{\rho}_{00} = \frac{i\Omega_{01}}{2}\left(\rho_{01} - \rho_{10}\right), \tag{2.66a}$$

$$\dot{\rho}_{11} = \frac{i\Omega_{01}}{2}\left(\rho_{10} - \rho_{01}\right) + \frac{i\Omega_{12}}{2}\left(\rho_{12} - \rho_{21}\right), \tag{2.66b}$$

$$\dot{\rho}_{22} = \frac{i\Omega_{12}}{2}\left(\rho_{21} - \rho_{12}\right), \tag{2.66c}$$

$$\dot{\rho}_{01} = -i\left(\Delta_{01} - i\gamma_{01}\right)\rho_{01} + i\Omega_{01}\left({}_{11} - \rho_{00}\right) - i\rho_{02}\Omega_{21}, \tag{2.66d}$$

$$\dot{\rho}_{12} = -i\left(\Delta_{12} - i\gamma_{12}\right)\rho_{12} + i\Omega_{12}\left({}_{22} - \rho_{11}\right) + i\rho_{02}\Omega_{10}, \tag{2.66e}$$

$$\dot{\rho}_{02} = -i\left(\Delta_{01} + \Delta_{12} - i\gamma_{02}\right)\rho_{02} + i\Omega_{01}\rho_{12} - i\rho_{01}\Omega_{12}, \tag{2.66f}$$

where the decoherence terms between levels are given by γ_{mn} and the population decay terms γ_{mm} are ignored since the states have long lifetimes compared to the decoherence lifetimes. These equations will be used in chapter 4 to model the observed spectra in velocity selective pump-probe spectroscopy experiments and in chapter 5 to model the theoretical population transfer afforded by STIRAP (described in the next section) in a system limited by the measured properties of our lasers.

2.4.1 STIRAP

One particularly interesting technique based on the three level system is a method of producing near complete population transfer from the initial state $|0\rangle$, to the second

excited state $|2\rangle$ called STImulated Raman Adiabatic Passage (STIRAP). Incoherent excitation can only produce 50% population transfer between two states and successively pumping the $|1\rangle \leftarrow |0\rangle$ transition incoherently and then the $|2\rangle \leftarrow |1\rangle$ transition can only transfer 25% population into the second excited state. Application of two π pulses, first to the $|1\rangle \leftarrow |0\rangle$ transition and then to the $|2\rangle \leftarrow |1\rangle$ transition could produce 100% population transfer [108] but this method is not robust as it requires very careful timing and is vulnerable to decay processes, particularly in the intermediate state [109]. STIRAP is a more robust population transfer method and is explained below.

The eigenstates of the time dependent Hamiltonian (2.65) are linear combinations of the bare states given by (in the case of two photon resonance)

$$\left|a^{+}\right\rangle = \sin\theta \sin\phi \left|0\right\rangle + \cos\phi \left|1\right\rangle + \cos\theta \sin\phi \left|2\right\rangle, \tag{2.67a}$$

$$\left|a^{0}\right\rangle = \cos\theta \left|0\right\rangle - \sin\theta \left|2\right\rangle, \tag{2.67b}$$

$$\left|a^{-}\right\rangle = \sin\theta \cos\phi \left|0\right\rangle - \sin\theta \left|1\right\rangle + \cos\theta \cos\phi \left|2\right\rangle. \tag{2.67c}$$

The mixing angle θ is given by

$$\tan\theta = \frac{\Omega_{01}}{\Omega_{12}}, \tag{2.68}$$

where the Rabi frequencies and therefore the mixing angle are time varying functions. The second mixing angle ϕ is given by [110]

$$\tan\phi = \frac{\sqrt{\Omega_{01}^2 + \Omega_{12}^2}}{\sqrt{\Omega_{01}^2 + \Omega_{12}^2 + \Delta_{01}^2} + \Delta_{01}}, \tag{2.69}$$

although for the remainder of the discussion it is not necessary.

It can be seen that equation (2.67b) is a combination only of the initial and final states with no contribution from the intermediate state. We also see that manipulation of the mixing angle θ from 0 to $\pi/2$ causes $|a^0\rangle$ to initially align with state $|0\rangle$ ($\theta = 0$) and end aligned with state $|2\rangle$ ($\theta = \pi/2$). In fact, if the system is

prepared such that at time $t = 0$ the mixing angle is $\theta = 0$ then only the so called dark state $|a^0\rangle$ is populated. If the mixing angle θ evolves adiabatically over time then the population is trapped in $|a^0\rangle$ and no population will be transferred into state $|1\rangle$ [73, 111].

Examination of equation (2.68) shows that in order to satisfy our condition $\theta\,(t = 0) = 0$ we require that the pump laser be turned off and the Stokes laser be turned on. Similarly to satisfy $\theta\,(t = \text{end}) = \pi/2$ we require that the pump laser be turned on and the Stokes laser turned off. This leads to a counter-intuitive sequence of laser pulses in which the laser which is tuned to the $|2\rangle \leftarrow |1\rangle$ transition is pulsed before the pump pulse. The two pulses must overlap in time and the mixing angle should evolve adiabatically by ensuring that the product of the interaction time and the Rabi frequency is large enough. The adiabatic following condition is given as [112]

$$\Omega\tau \gg 1, \tag{2.70}$$

where τ is the interaction time *i.e* the length of the laser pulse. Ensuring that the adiabatic following condition is met with a counter-intuitive pulse sequence, it is possible to transfer 100% of the population in $|0\rangle$ into $|2\rangle$.

The theoretical framework presented during this chapter will now be used to support the experimental work carried out throughout the rest of this thesis. In the next chapter, a DFB-QCL will be characterised and used to perform saturation spectroscopy on nitric oxide. The laser linewidth will be measured by Lamb-dip spectroscopy and the narrow linewidth will be shown to lead to velocity selection that in turn leads to asymmetry and eventually rapid passage when combined with increasing frequency chirp rates. In chapter 4 a second laser will be introduced in order to perform pump-probe spectroscopy and in this case tt will be necessary to utilise the three-level density matrix to correctly model the observed spectra. In chapter 5 the three-level density matrix equations (2.66)will again be used to model the expected behaviour of a real STIRAP system using the data gathered about our laser systems presented throughout the previous chapters.

Chapter 3

Coherent Transient Spectroscopy Using a Single CW DFB QCL

The work in this thesis involved the use of two different quantum cascade lasers. One, a commercial external cavity laser (Daylight Solutions) that has been described in detail before [15], and the other a distributed feedback (DFB) laser specifically purchased for this project. This chapter details the characterisation of this DFB laser and subsequent absorption spectroscopy experiments, using both direct and sub-Doppler techniques. Initially the high power of the laser is used to demonstrate power saturation of an absorption line in nitric oxide. Next, Lamb dip spectroscopy is used to measure the linewidth of the DFB laser and further investigations using the same experimental setup show the evolution of rapid passage effects.

3.1 Characterisation of a DFB QCL

3.1.1 Mounting the DFB QCL

The DFB QCL used in this thesis was purchased from Maxion Technologies, inc (device number DQ5-M575AH-NS) and was specified to emit at around 5.3 µm in single mode cw operation and at powers in excess of 150 mW. The laser was mounted in a custom designed mount (shown in figure 3.1) for use with custom driving

electronics to enable a large degree of control over both the temperature and the supplied current and thereby provide flexible operation. The mount consists of a copper heatsink onto which the laser is mounted using two screws. A piece of 0.1 mm thick indium foil was placed between the base of the QCL and the copper heatsink as the design made it difficult to polish the mounting platform to achieve a smooth finish. The indium therefore acts as a thermal interface material, filling in any air gaps left by the unpolished surface. Indium is chosen both for its very high thermal conductivity and for its softness, allowing it to mould into any gaps. The copper heatsink is mounted to a two-stage, water cooled peltier thermoelectric cooler (TEC, RS Components Ltd. part number 490-1452) which actively controls the laser chip temperature through in-house designed and built control electronics. Two spring loaded pins contact the laser anode and cathode to supply current to the chip and the whole is mounted inside a sealed body which is evacuated by means of a small vacuum pump (KNF N84.3ANE-K). The laser chip is mounted such that the output facet is as close as possible to the BaF_2 output window and the laser and peltier currents are supplied through a sub-D connector hermetically sealed to the top of the mount.

3.1.2 Laser Output Characteristics

To check that the laser was mounted correctly and that the chip was functioning as expected the voltage drop across the laser was measured as the current I, was increased. It is expected that initially the measured voltage increases rapidly before becoming a linear function of I. The current was supplied to the laser using a custom made low noise current controller, with the temperature being held constant by a custom built driver. The resulting curve shown in figure 3.2 shows that the chip responds as expected, with the potential increasing rapidly to begin with before becoming linear at approximately 200 mA. The laser does not start to emit radiation until the supplied current reaches the threshold current I_{th}, which lies within the region of linear voltage increase. The maximum current recommended by the

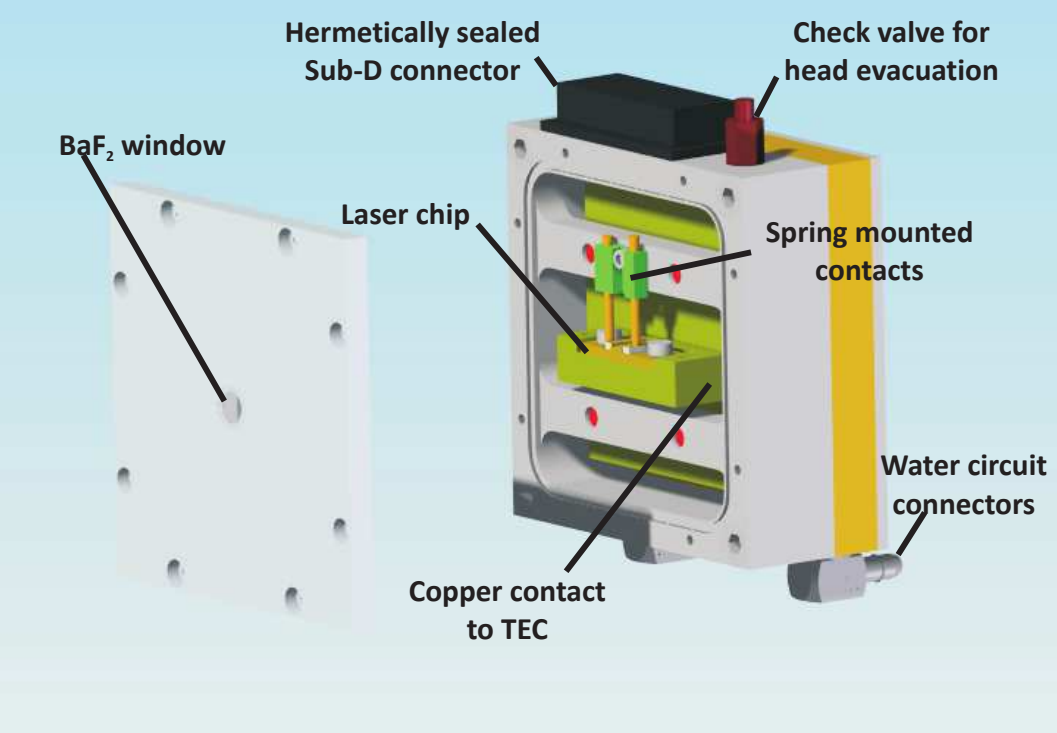

Figure 3.1: A diagram of the mount into which the DFB QCL chip was fixed. The mount was designed and built in-house to allow a high degree of flexible control over the laser output.

manufacturers for cw operation was 1000 mA, hence the properties were not measured beyond this limit and a limiter was built into the current driver to prevent the current being increased further than this accidentally. Checking against the curve in figure 3.2 provides a simple check that the laser circuit is well maintained as a short or open circuit would cause significant deviation which could lead to damage to the laser.

The laser mount shown in figure 3.1 was placed on a translation stage (Thorlabs MBT602) and an aspheric collimation lens (focal length = 4 mm) was brought close to the BaF_2 output window in order to collect as much of the output light as possible. The laser position relative to the lens was then adjusted to achieve collimation over a long path length. The laser may be tuned using both temperature and current. Tuning the temperature is a slow process, whereas current tuning may be done by applying a current ramp to the laser input and can be done very quickly. We choose therefore to tune the laser by changing the current whilst keeping the temperature constant. However the temperature we choose to hold the laser chip at changes the

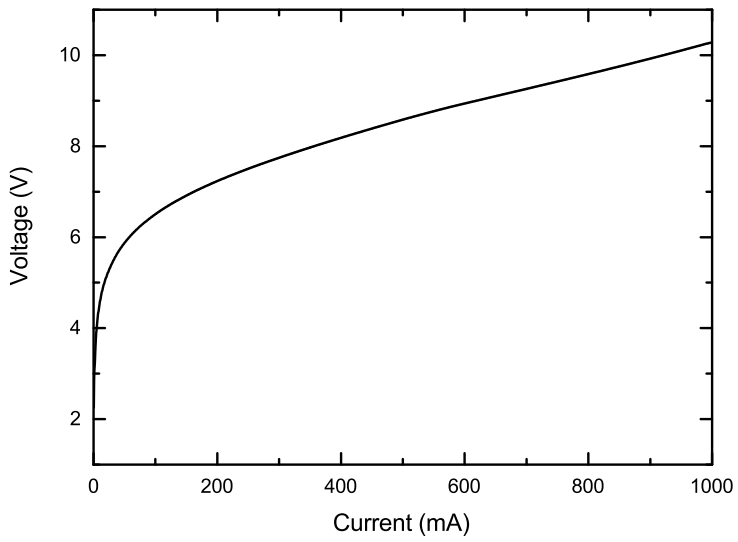

Figure 3.2: Showing the measured voltage drop over the laser as a function of applied current. After rising sharply initially, the voltage increases linearly with applied current after about 200 mA. By checking against this curve it is possible to give an early warning of a bad connection or short circuit that could damage the laser.

centre output frequency as well as the threshold current and the output power of the laser. Changing the current similarly causes a change in the power of the output radiation as the frequency changes. It was necessary therefore to measure both the output optical power and the output frequency as a function of driving current at various temperatures to fully understand how to control the laser output.

The power measurements were made using a Melles Griot power meter (Broadband 13PEM001) placed close to the output window of the laser mount to minimise absorption losses to atmospheric gases and are plotted in figure 3.3. The laser output power is high, giving over 150 mW at all temperatures tested and over 250 mW at the lowest temperatures combined with the highest driving currents. The threshold current varies with temperature from 600 mA at 10 °C to a little under 500 mA at −15 °C, and the output power for a given driving current increases with decreasing temperature. These effects are expected from the structure of QCLs as described in chapter 1. At 10 °C the power rolls off as the current approaches 1000 mA. This is a sign of the laser chip reaching its gain limit and so the measurements were concluded.

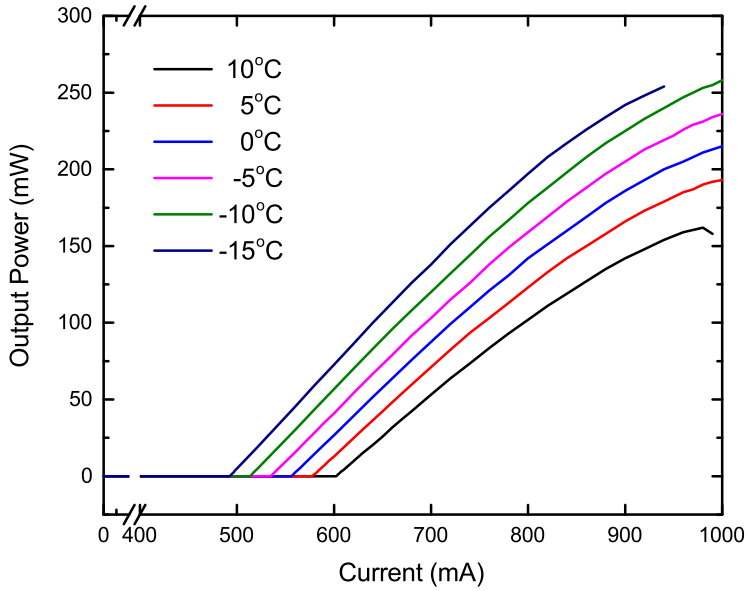

Figure 3.3: The optical power output as a function of increasing applied current is shown at various temperatures. Increasing the current increases the power, as does decreasing the temperature of the laser chip.

Likewise at $-15\,^{\circ}\mathrm{C}$ it became increasing difficult for the temperature controller to keep the chip at a stable temperature beyond 900 mA of supplied current so the measurements were concluded at this slightly reduced limit. Looking at figure 3.2 we see that at 900 mA of supplied current the voltage drop across the laser shows that the dissipated power is over 9 W, most of which is heat that must be soaked up by the heatsink. It is perhaps not surprising that under these circumstances the temperature controller in combination with the TEC was unable to supply the necessary driving current to maintain the low temperature.

The frequency output of the laser was measure by directing the light into a commercial FTIR spectrometer (Perkin Elmer Spectrum 100). The laser current and temperature were set and a scan was made with the FTIR spectrometer between $1895\,\mathrm{cm}^{-1}$ and $1905\,\mathrm{cm}^{-1}$, chosen to cover a range greater than the manufacturer's reported operating frequency range. The current was then changed, keeping the temperature constant and another scan was made, continuing like this over the whole current and temperature range. The resolution of the spectrometer was $0.5\,\mathrm{cm}^{-1}$,

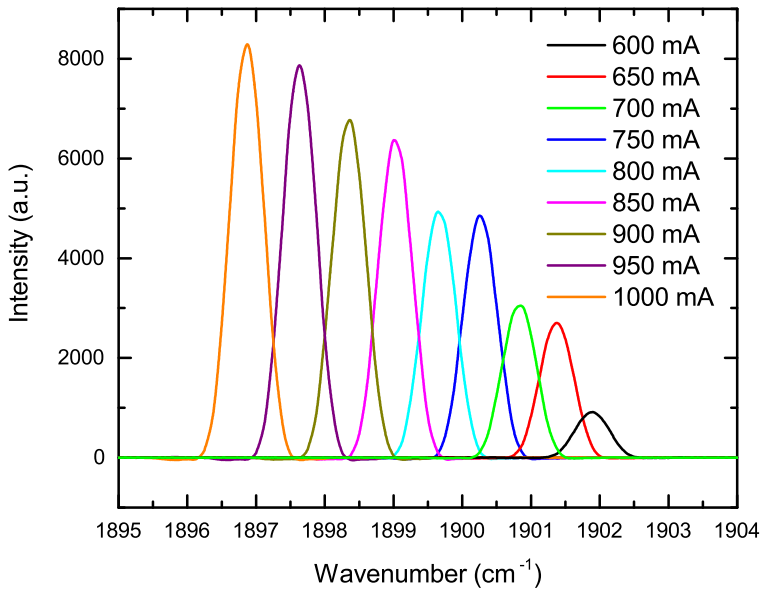

Figure 3.4: The output of an FTIR spectrometer into which the laser beam is directed is shown for various applied currents at a temperature of 0 °C. The output wavenumber decreases with increasing current applied to the laser.

which is significantly larger than the expected linewidth of the laser but much less than the tunability of the laser. The results of the FTIR scans over a range of currents at a chip temperature of 0 °C are shown in figure 3.4.

At each current the spectrum appears as a single feature showing that the laser is (to at least the resolution of the spectrometer) emitting in a single mode. The peak amplitudes of the individual features are related to the output power of the laser. However they are not necessarily linearly correlated since the measured amplitude depends on the response of the spectrometer's detector which is unknown. The amplitudes in figure 3.4 are nevertheless roughly consistent with the powers shown in figure 3.3. Similar plots to figure 3.4 were created for various temperatures to produce tuning curves showing the output frequency as a function of driving current for each temperature, and these tuning curves are shown in figure 3.5.

Increasing the current causes a decrease in the frequency (wavenumber) of the output radiation along with the increase in power shown by figure 3.3. The curves are nearly linear over approximately a $5\,\mathrm{cm}^{-1}$ range at each temperature and the

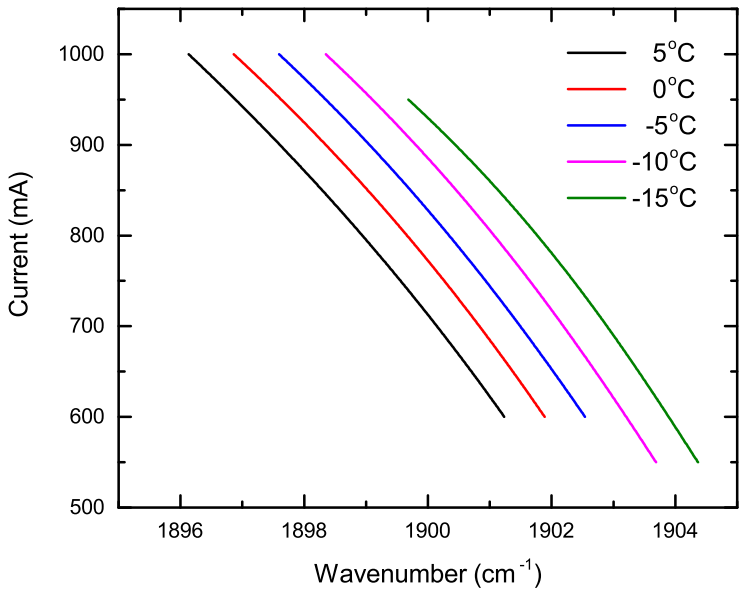

Figure 3.5: Tuning curves as a function of applied current at various temperatures of the laser chip. The output frequency (wavenumber) decreases with increasing current and temperature.

total range over which the laser is shown to emit spans approximately $8\,\mathrm{cm}^{-1}$ from $1896\,\mathrm{cm}^{-1}$ to $1904\,\mathrm{cm}^{-1}$. As the temperature is decreased the output wavenumber increases. The combination of figures 3.3 and 3.5 allows laser conditions to be chosen to best fit the requirements of the experiment.

The beam width of the laser was measured using the knife edge method. A knife edge made from a piece of card was mounted on a translation stage 24 cm from the laser collimation lens and moved through the laser beam with the beam intensity being measured as a function of knife edge displacement. For this method we assume that the collimated laser beam has a Gaussian intensity profile although the actual quantity measured was the total laser power incident on the detector which is the integral of the intensity over the area of the beam. If the beam is blocked to begin with and gradually uncovered then the power measured as a function of knife edge displacement has the form of the error function

$$I(x) = I_0 \int_0^r e^{\frac{-2x^2}{w^2}} \mathrm{d}x, \tag{3.1}$$

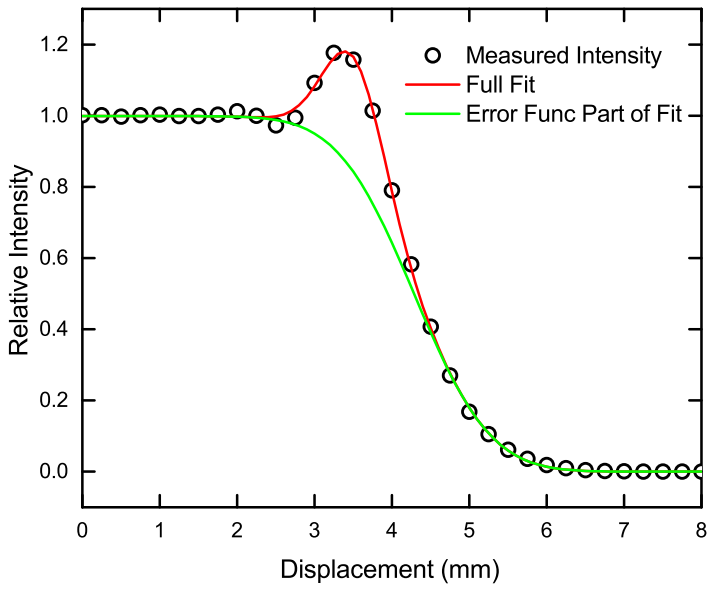

Figure 3.6: The relative intensity of the laser beam as a knife edge is moved through the beam profile. Initially the intensity increases as the knife edge cuts the beam and edge diffraction results in constructive interference. Fitting with equation (3.2) gives the fit shown in red with the error function only part of the fit shown in green. The beam radius measured by the fit is 1.56 mm.

where w is the radius of the beam and x is the knife edge position. Starting from an uncovered beam the function is the complimentary error function $(1 - I(x))$.

Figure 3.6 shows an example of the laser beam width measurements with associated fit. It is immediately obvious that the measured signal does not fit the shape of the complimentary error function. Instead the signal appears to increase as the knife edge begins to cut the laser beam and then falls more sharply than the error function. This behaviour is well known as the knife edge effect and may be understood by applying Huygens' principle. A well defined object, in this case the knife edge, acts as a secondary source creating a new wavefront which propagates from the knife edge. In turn this causes constructive interference which gives rise to the increased intensity. The diffracted wave at the boundary can be approximated by adding in a boundary diffraction wave as per Tay *et al.* [113]

$$I = I_0 \int_x^\infty \frac{1}{w_k} e^{\frac{-2(x-r)^2}{w_k^2}} \mathrm{d}x + B_0 e^{\frac{-2(x-r)^2}{w_b^2}}, \tag{3.2}$$

where w_k is the beam radius taken from the complimentary error function part of the equation and w_b is the width of the Gaussian describing the effect of the boundary diffraction wave with height B_0.

Fitting the data to equation 3.2 gives w_k as the beam radius when the intensity has fallen to $1/e^2 = 0.135$ of the peak value (excluding boundary effects). From this it is simple to calculate the radius under different definitions such as the full width at half maximum. The measured beam radius ($1/e^2$) was 1.56 mm.

3.2 Spectroscopy of Nitric Oxide

The nitric oxide radical has a $^2\Pi$ ground electronic state and the molecular orbital configuration

$$X^2\Pi : (1\sigma)^2 (2\sigma^*)^2 (3\sigma)^2 (4\sigma^*)^2 (5\sigma)^2 (1\pi)^4 (2\pi^*)^1 .$$

Nitric oxide displays four sources of angular momentum: electron spin, S, orbital angular momentum L, rotational angular momentum R and nuclear spin I (the ^{14}N atom has $I = 1$). The spin-orbit interaction scales with the nuclear charge which means that in a molecule such as NO which has low nuclear charges the spin-orbit interaction is weak. The various angular momenta may couple in a variety of ways which are described by a set of limiting cases known as Hund's cases. While any real system is actually a mixture of the five Hund's cases, the NO molecule in low rotational states may be reasonably described under Hund's case (a). In this case the orbital angular momentum L couples strongly to the electrostatic field produced by the nuclear charges such that the magnitude of L is poorly defined and therefore L is no longer considered a good quantum number. Instead its projection onto the internuclear axis $\Lambda\hbar$ is used. The electron spin couples to L via the spin-orbit interaction and therefore indirectly couples to the internuclear axis with a projection of $\Sigma\hbar$ which has multiplicity of $2S+1$. The component of the total electronic angular momentum which lies along the internuclear axis is called $\Omega = |\Lambda + \Sigma|$. The coupling

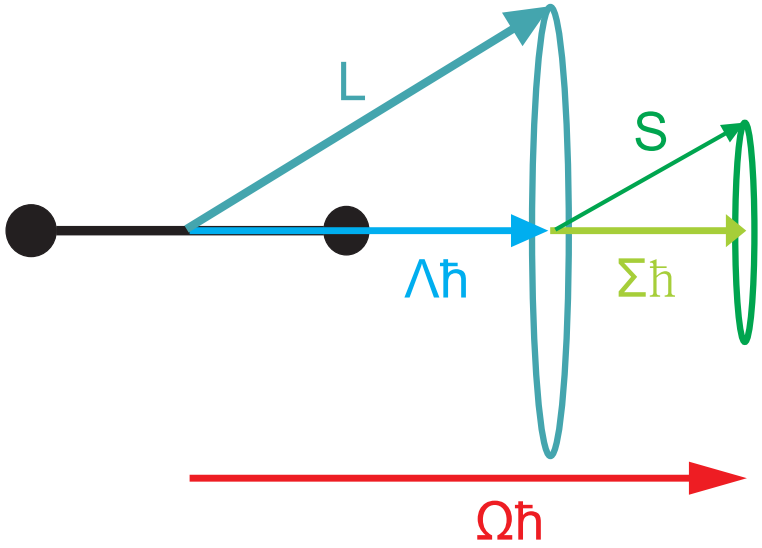

Figure 3.7: A schematic of the angular momentum coupling under Hund's case (a). The orbital angular momentum couples to the electrostatic field produced by the two charges in the molecule with its projection onto the internuclear axis given by $\Lambda\hbar$. The spin then couples indirectly to the internuclear axis with a projection of $\Sigma\hbar$ and the total angular momentum along the internuclear axis is given by $\Omega\hbar$.

is represented in figure 3.7. The set of good quantum numbers under Hund's case (a) coupling scheme is now Λ, S, Σ, J and Ω.

The molecular term symbol is written ${}^{2S+1}\Lambda_{\Omega}$. For NO we have $\Lambda = \pm 1$ and $S = \frac{1}{2}$, which gives $\Sigma = \pm\frac{1}{2}$ so that $\Omega = \frac{1}{2}, \frac{3}{2}$. The spin-orbit interaction causes the ${}^2\Pi_{\frac{1}{2}}$ and ${}^2\Pi_{\frac{3}{2}}$ states to be shifted in energy by $\Delta E = A\Lambda\Sigma$, where A is the spin-orbit coupling constant which for NO is $+123\,\mathrm{cm}^{-1}$ [114]. As such, the lowest energy state is the ${}^2\Pi_{\frac{1}{2}}$ although the splitting is less than the thermal energy k_BT ($\sim$200 cm^{-1} at room temperature) so there is significant population in both spin-orbit states and transitions from both are observed in the room temperature infrared spectrum.

In a stationary molecule the two states $\Lambda = \pm 1$ are degenerate since the two simply correspond to opposing directions of electron rotation about the internuclear axis. When the molecule rotates the electrons are not fully able to follow the motion of the internuclear framework. This electron slip increases with increasing rotational quantum number and causes decoupling of the angular momenta and the partial admixture of Σ like orbital character into the Π orbitals which in turn causes a splitting between the states $\Lambda = \pm 1$. This mixing is visualised in figure 3.8 which

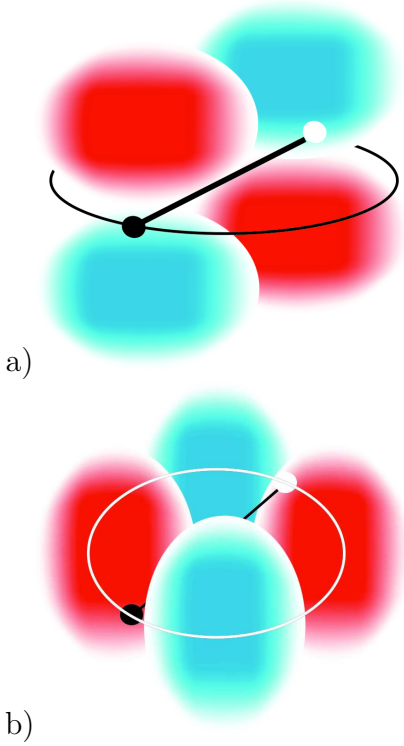

Figure 3.8: An interpretation of Λ doubling showing the effects of electron slip. In a) the molecular framework slips between the nodes of the electronic orbitals whereas in b) the nuclear framework slips into areas of high electron density. b) corresponds to the partial admixture of Σ orbital character. Adapted from [117]

shows how the internuclear axis may slip between the nodes (figure 3.8 a)) of the molecular orbitals or into a region of high charge density (figure 3.8 b)). When the nuclear framework slips into a region of high electron density, this corresponds to a partial mixing of Σ character into the wavefunction. The splitting is known as Λ-doubling and presents as an observed doublet of energy levels for a given quantum number with the components labelled e and f. The e levels are those with parity $+(-1)^{J-\frac{1}{2}}$, whereas those states with parity $-(-1)^{J-\frac{1}{2}}$ are f levels [115]. The Λ-doubling is larger for the $^2\Pi_{\frac{1}{2}}$ fine structure state than for the $^2\Pi_{\frac{3}{2}}$ state and increases with increasing total angular momentum (excluding nuclear spin) J [116]. In the $^2\Pi_{\frac{1}{2}}$ state the difference in transition energies is larger than the Doppler width of the transition and so a doublet is seen in the absorption spectrum, whereas in the $^2\Pi_{\frac{3}{2}}$ state the splitting is less than the Doppler width so the spectrum appears as a singlet unless sub-Doppler techniques are used [114].

The final interaction that determines the high resolution IR spectrum of NO is

the nuclear hyperfine interaction. The most abundant isotope of nitrogen, ^{14}N has a nuclear spin of $I = 1$. This means that the total molecular angular momentum quantum number including nuclear spin F takes values from $J - I$ to $J + I$, which leads to a three-fold splitting of the spectral lines (except for $J = \frac{1}{2}$ where the splitting is two-fold). The splitting is on the order of MHz or smaller and so can only be observed in sub-Doppler experiments, and only then with a sufficiently narrow laser linewidth [118].

The final thing to consider in the spectra of NO are the selection rules for allowed transitions. These are:

$$\Delta\Lambda = 0, \pm 1 \tag{3.3a}$$

$$\Delta S = \Delta\Sigma = 0, \tag{3.3b}$$

$$\Delta\Omega = 0, \pm 1, \tag{3.3c}$$

$$\Delta J = 0, \pm 1, \tag{3.3d}$$

$$\Delta F = 0, \pm 1, \tag{3.3e}$$

$$e \longleftrightarrow e, f \longleftrightarrow f, e \not\longleftrightarrow f. \tag{3.3f}$$

Since this thesis is only concerned with ro-vibrational transitions (in which $\Delta v = 1$) the selection rule for Λ is $\Delta\Lambda = 0$ and so the same can be said for $\Delta\Omega$ given that the spin is not allowed to change ($\Delta S = 0$). The transitions in which J changes by $\Delta J = -1, 0$, and $+1$ are labelled P,Q, and R respectively.

3.3 Direct Spectroscopy

A comparison with the HITRAN database [119] reveals that the strongest NO transitions (those with the largest absorption cross sections) in the frequency region that the Maxion laser emits in are the R(5.5) and R(6.5) fundamental transitions originating in both spin-orbit states. The strongest hot band transitions ($v = 2 \leftarrow 1$) are the R(15.5) and R(16.5) transitions and again both spin-orbit states are available.

Absorptions corresponding to these transitions are easily observable using a short path length cell.

An initial experiment was performed to see the saturation effect of the laser power in a direct absorption experiment on the $R(6.5)_{\frac{1}{2}}$ transition at 19.5 mTorr of NO. In this case the laser beam was directed through a cell with a path length of 84 cm and CaF_2 windows and onto a mercury cadmium telluride (MCT) detector (VIGO PVI-2TE-6). The laser was operated at $-10\,°C$ and 878 mA and the power was measured as close to the front window of the cell as possible. A maximum power of 164 mW was measured prior to the cell and a scan was applied to the current driver of the laser using a function generator (TTi TG1010A) to produce a sine wave with a peak to peak voltage of 1.5 V. Using a germanium etalon with a free spectral range of 500 MHz, the tuning rate of the laser was calculated to be $0.70\,\text{MHz}\,\mu\text{s}^{-1}$. The laser power was attenuated to varying amounts using a polariser (Alphalas MgF_2 Rochon polariser). Measurements were made at various power levels using the same pressure of NO with the lowest power of 2 mW resulting in linear absorption as described by the Beer-Lambert law (equation (2.1)). The results of these measurements are shown in figure 3.9.

The measured decrease in the absorption caused by the power saturation is clear. Using equation (2.22) with α_0 given by the absorbance measured at the lowest power of 2 mW, produces values for the saturation parameter of between 0.09 at 8 mW power and 12.7 at 164 mW power. Starting from equation (2.21) and using the fact that initially all population is in the ground state N_1 (*ie.* $\Delta E \gg k_B T$) the population transferred into the excited rovibrational state is given by $N_2 = \frac{S_0}{2+2S_0}$. The population transferred into the excited state as a function of laser power is plotted in figure 3.10 and is seen to approach the limiting value of 50%.

The saturation parameter may be calculated from the properties of the gas and the measured intensity of the laser using equation (2.15) which may also be expressed as

$$S = \frac{2I\mu^2}{c\epsilon_0 h^2 \Gamma^2}. \tag{3.4}$$

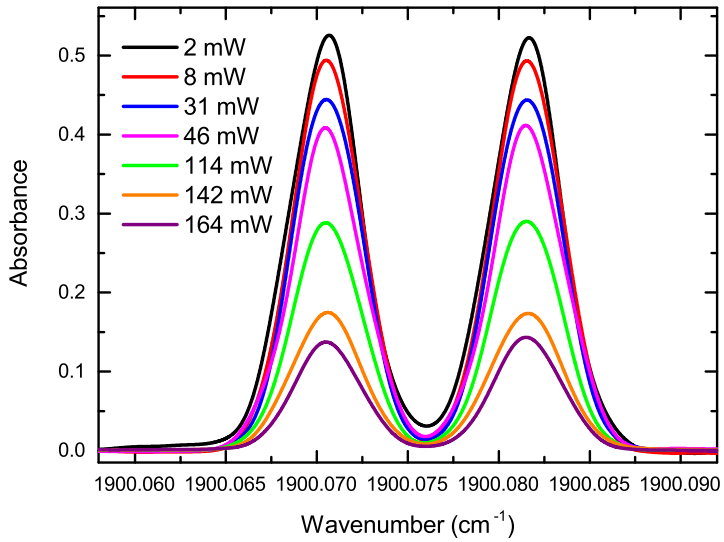

Figure 3.9: The absorption spectrum of 19.5 mTorr of NO with laser powers of between 2 mW and 164 mW. The reduction in the absorption produced by saturation of the transition as the power increases is clearly seen.

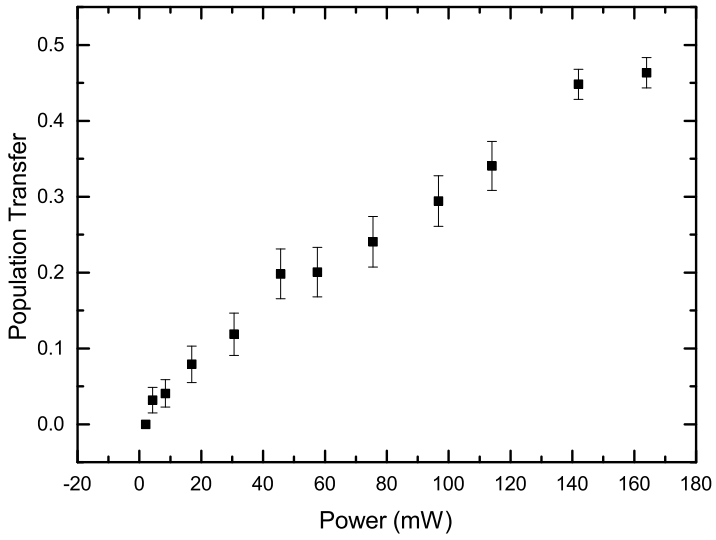

Figure 3.10: Population transfer as a function of laser power. The amount of population transferred increases with increased power as expected, approaching the limiting value of 50%.

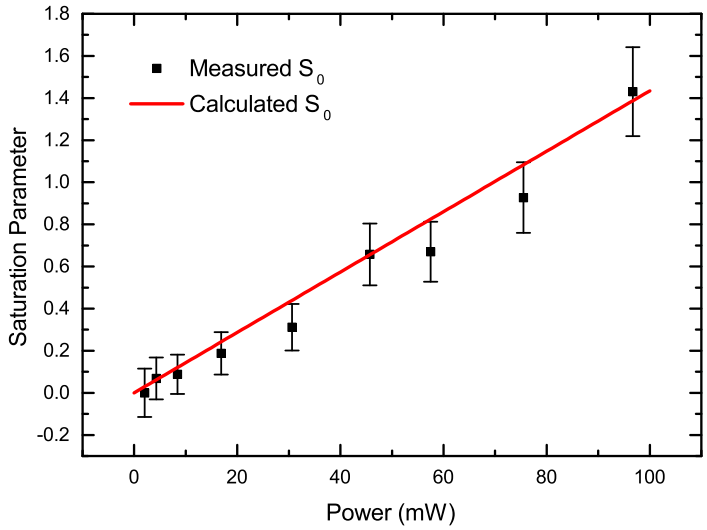

Figure 3.11: The saturation parameter measured in a sample of NO at a pressure of 19.5 mTorr displayed alongside the calculated stauration parameter (red line) using equation (3.4).

Here μ is the dipole moment, the intensity (irradiance) I, of the laser is given by the measured power divided by the area of the laser spot and Γ is the relaxation rate of the system. The relaxation rate is calculated from the transit time broadening (see chapter 2) and the self broadening parameter (0.062 $\mathrm{cm}^{-1}\mathrm{atm}^{-1}$) given by HITRAN and the measured pressure, and the dipole moment is calculated to be 0.056 D (1.87×10^{-31} C m). The calculated saturation parameter is shown alongside the measured saturation parameters and their associated errors in figure 3.11. A very good agreement between the theory and the experimental data is shown. It should be noted that equation (3.4) applies only in the steady state regime in which the interaction time is much greater than the excited state lifetime. In the case of Doppler broadening and a slow frequency scan this condition is well met and the theory agrees well with the experimental data.

3.4 Sub-Doppler Spectroscopy

The observed line profile in direct absorption spectroscopy is a convolution of the Doppler profile convolved with the laser linewidth function. The laser linewidth is

much narrower than the Doppler profile so it is not possible to accurately measure it by direct spectroscopy. The natural linewidths (as described in chapter 2) of these transitions are on the order of kHz which is significantly smaller than the expected linewidth of the laser and so a Lamb dip experiment was performed to give a dip with a linewidth that provides a measurement of the laser linewidth.

3.4.1 Experimental

Rather than retroreflecting the beam as described in section (2.2), the beam was split by a CaF_2 beam splitter which reflected approximately 10% of the power. The strong pump beam and weak probe beam then counter propagated through a 112 cm long cell fitted with Brewster angled CaF_2 windows as shown in figure 3.12. The probe beam was collected onto a detector (VIGO PVMI-3TE-10.6) while the pump beam went to a beam dump.

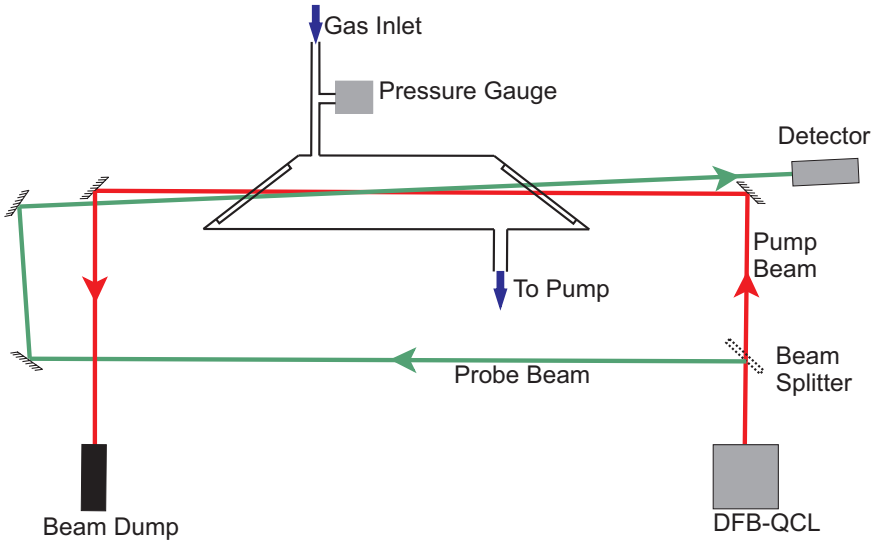

Figure 3.12: Lamb dip experimental setup. The beam is split into 'pump' and 'probe' beams which counter propagate through the cell.

The ideal alignment of the system would have the pump and probe beams perfectly overlapping, however this causes optical feedback into the laser which induces mode hops when the laser is scanned. This effect was observed in the Maxion laser, leading to significantly distorted absorption lines. One method commonly used to

protect lasers from optical feedback is to place an optical isolator in the beam path. These consist of a pair of polarisers, one at each end of a Faraday rotator which itself rotates the polarisation of the light by 45°. Any reflected light entering the isolator is rotated by a further 45° in the same direction and is therefore blocked by the input polariser. Due to the difficulties in finding materials that display the Faraday effect necessary to make an isolator *and* are transparent in the mid-IR it was not possible to purchase an optical isolator for this experiment. It was therefore necessary to slightly uncross the pump and probe beams such that there was sufficient overlap to observe Lamb dips but without causing significant optical feedback.

The laser frequency was scanned by applying a triangular voltage ramp to the current controller using a digital function generator (TTi TG1304). The laser frequency chirp rate is a function of both the frequency and amplitude of the voltage modulation which were both altered to give different chirp rates. The amplitude of the voltage ramp was chosen to ensure that the laser frequency was scanned linearly over the absorption feature. The spectra were recorded using a 400 MHz bandwidth digital oscilloscope (LeCroy WaveSurfer 44MXs-A), though the bandwidth was restricted to 20 MHz by the amplifier built into the detector. All data was recorded on a frequency up-chirp (that is the laser was scanning from low to high frequency) and approximately 100 sweeps were recorded with the data subsequently being re-centered on the minimum of the Lamb dip and averaged in MATLAB to reduce drifts and noise. A frequency scale is established using the positions of the Lamb dips as known fixed frequency points and interpolating across the Doppler broadened background spectrum. The chirp rate was measured by placing a germanium etalon with a free spectral range (FSR) of 500 MHz in the beam path and recording a sweep of the laser. The transmission function of the etalon as the laser frequency is scanned appearing in figure 3.13 shows that the frequency scan is nearly linear and as such the frequency scale is directly given by the spacing of the transmission maxima in the time-domain signals. The change in amplitude of the fringes and the ramped baseline reflect the small change in power of the laser across the current

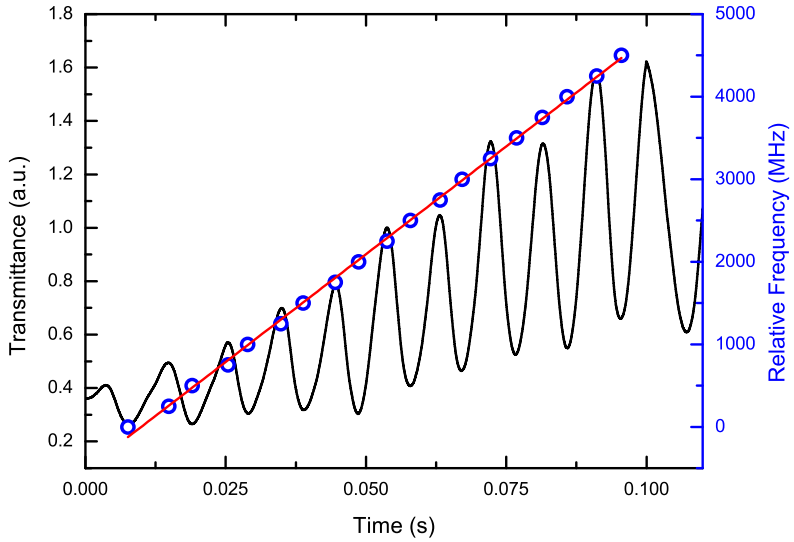

Figure 3.13: The transmission of the germanium etalon during a frequency up-chirp of the laser, shown with a linear fit to the time spacing of the fringes. The frequency spacing is 500 MHz (or 250 MHz between peaks and troughs) giving a frequency chirp rate of 0.053 MHz µs^{-1}. A small secondary oscillation in the fringe amplitudes is likely due to imperfect alignment of the etalon. For the measurtement of the chirp rate, only the spacing of the fringes is relevent.

scan.

3.4.2 Laser linewidth measurements

The Λ-doublet splittings in the R(6.5)$_\Omega$ transitions are *ca.* 330 MHz and *ca.* 26 MHz in the $\Omega = \frac{1}{2}$ and the $\Omega = \frac{3}{2}$ transitions respectively. Hence in an absorption spectrum the R(6.5)$_{\frac{1}{2}}$ transition appears as a doublet whereas in the R(6.5)$_{\frac{3}{2}}$ the splitting is less than the Doppler broadening (*c.a.* 124 MHz) and it appears as a singlet as shown in figure 3.14. There is of course a further splitting due to hyperfine coupling with the nuclear spin of the nitrogen ($I = 1$). Each angular momentum state is thus split into three hyperfine levels, giving a total of six hyperfine levels. The selection rule for transitions between these hyperfine levels is $\Delta F = 0, \pm 1$ where $F = |J + I| \ldots |J - I|$ is the total angular momentum quantum number including nuclear spin.

The laser linewidth was measured using Lamb dip spectroscopy on the NO

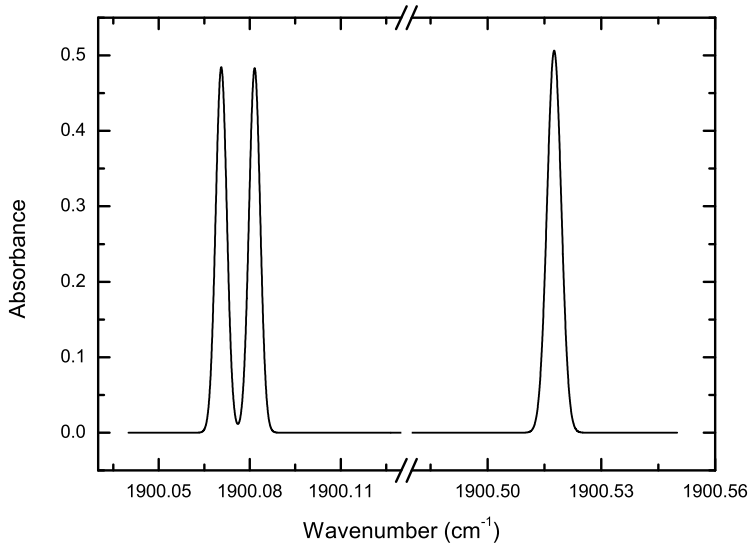

Figure 3.14: Calculated absorption spectrum of NO covering both spin-orbit states of the R(6.5) $v = 1 \leftarrow 0$ transition. The transition originating from the $\Omega = \frac{1}{2}$ spin-orbit state appears as a doublet due to Λ doublet splitting, whereas that from the $\Omega = \frac{3}{2}$ state appears as a singlet as the Λ doublet splitting is less than the Doppler width. The calculations were made using the absorption cross sections given by HITRAN. [119]

$R(6.5)_{\frac{3}{2}}$ $v = 1 \leftarrow 0$ transition. The cell was filled with approximately 8 mTorr of NO and a Lamb dip spectrum was recorded at a laser frequency scan rate of $0.053\,\mathrm{MHz\,\mu s^{-1}}$ with a pump power of 130 mW. Six hyperfine lines were apparent in the resulting spectrum shown in figure 3.15. This data was fitted with equation (2.24) using least squares minimisation in MATLAB. The equation is applied to all six hyperfine transitions with the amplitudes of the Doppler profiles being weighted according the the transition cross sections given by HITRAN [119], and the saturation parameters weighted according to the squares of the respective dipole moments (see equation (3.4)). The overall Doppler lineshape is the sum of the six individual components and the best fit to the data presented in figure 3.15 *a*) is shown in *b*). The Lamb dips are well fit by the Gaussian lineshape in the second term of equation (2.25) with full-width at half-maximum giving a laser linewidth of 800 ± 60 kHz. This compares favourably with linewidths of 21 MHz, [62] 5 MHz, [24] 4 MHz, [59] and 2.5 MHz measured using similar techniques with external cavity QCLs, [21] and with linewidths of 1-10 MHz for DFB QCLs [61, 120–122]. The linewidth is

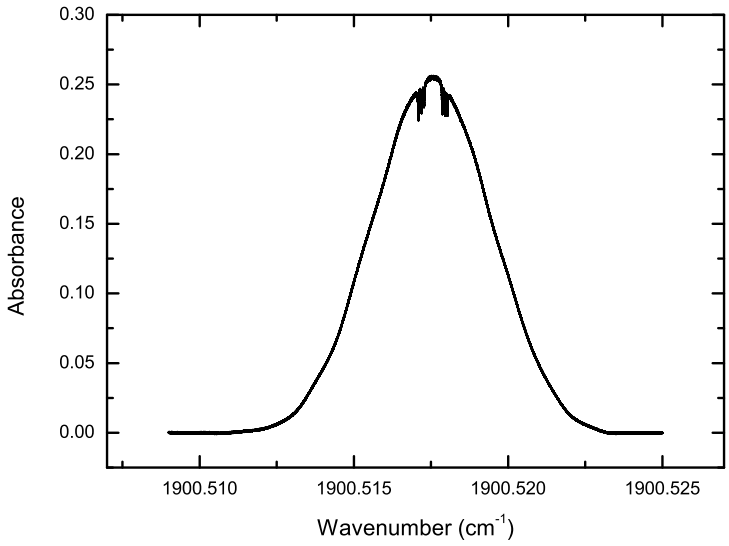

a)

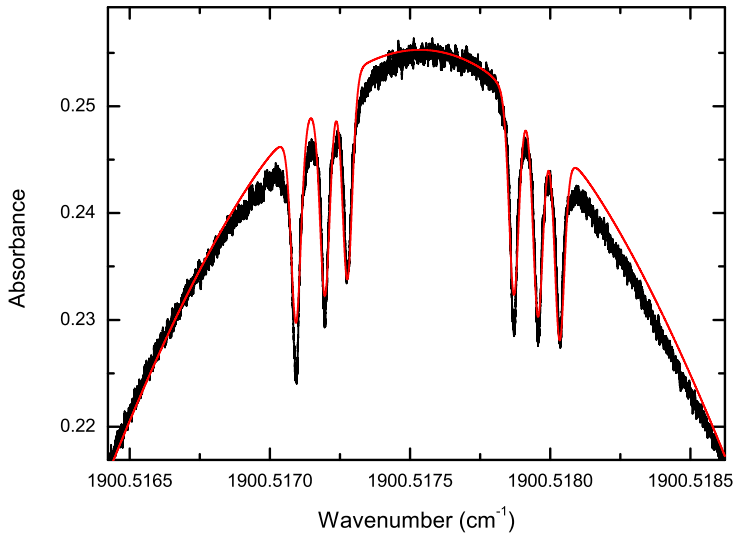

b)

Figure 3.15: Lamb dip spectrum of the NO R(6.5)$_{\frac{3}{2}}$ $v = 1 \leftarrow 0$ transition showing 6 separate Lamb dips corresponding to the strongest 6 hyperfine transitions. The full Doppler profile is shown at a pressure of *c.a.* 8 mTorr and a laser chirp rate of 0.053 MHz μ s^{-1} in a). The fit to the observed spectrum using equation (2.24) which gave a laser linewidth of 800 $\pm$ 60 kHz is shown in b).

limited mainly by supply current noise, since the intrinsic linewidth of QCLs has been shown to be of the order of only a few hundred Hz. [9, 58, 60]

Measurements with an external cavity QCL showed a narrowing of the laser linewidth with increasing scan rate [123] and was attributed to low frequency current noise being reduced at the higher scan rates. The Maxion DFB laser may be easily scanned at almost any rate simply be applying the correct current ramp to the driver using a function generator. The current controller was designed to be a low noise source and so it was expected that the change in linewidth with scan rate would be relatively small. To test this hypothesis, the chirp rate was increased by increasing the frequency of the triangular voltage ramp applied to the current controller with the rest of the experiment unchanged. Instead of observing an obvious change in the linewidth of the laser several other effects which altered the shape of the observed dips were observed and these are now discussed.

3.4.3 Lamb dip shape as a function of chirp rate

The effects detailed in this subsection resulted in the 6 Lamb dips seen on the $R(6.5)_{\frac{3}{2}}$ transition blurring into one another. Although both the $R(6.5)_{\frac{1}{2}}$ and $R(6.5)_{\frac{3}{2}}$ transitions show changes in the size and shape of the Lamb dips, these transient experiments were more easily seen on the $R(6.5)_{\frac{1}{2}}$ transition in which the hyperfine splitting in each Λ-doublet is smaller than or comparable to the laser linewidth. Therefore, as shown in figure 3.16, only a single Lamb dip is seen on each of the Λ-doublet resolved transitions (see figure 3.16). Due to the narrow linewidth of the laser it is however possible to partially resolve one of the hyperfine transitions which has a splitting of 1.02 MHz, in the f component from the other two. In the e component the splitting is much less than the laser linewidth and so only a single dip is observed.

At relatively slow chirp rates of up to approximately $1\,\mathrm{MHz\,\mu s^{-1}}$, the depth of the Lamb dips was observed to increase relative to the size of the absorption signal as the chirp rate increased. Figure 3.17 shows examples of this behaviour. The

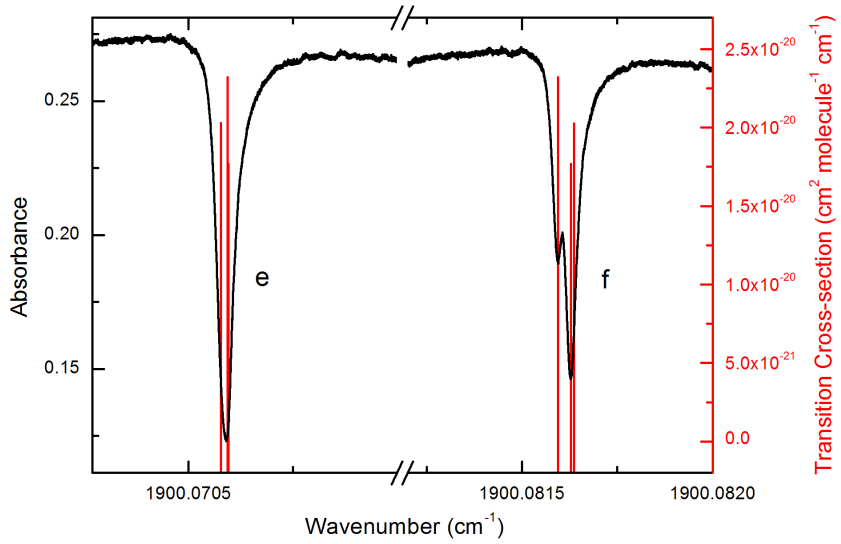

Figure 3.16: Lamb dip spectra of the e and f components of the Λ doublet in the $R(6.5)_{\frac{1}{2}}$ transition of NO with the transition intensities (from HITRAN [119]) of the corresponding hyperfine components shown. Note that the laser linewidth is narrow enough to allow partial resolution of the hyperfine lines in the f component.

Lamb dips were again fitted using equation (2.25). The values of Γ and Δ_l were both fixed parameters in the fitting with Γ calculated from the quadrature addition of the transit time broadening and the collisional broadening and the laser linewidth being fixed at the measured value of 800 kHz. Again all six hyperfine components are summed to give the overall lineshape. The increase in the size of the Lamb dip reflects an increase in the population transferred into the pumped velocity group in the $v = 1$ level as plotted in figure 3.18. The population transfer is seen to increase from around 20% to over 35%, simply by increasing the chirp rate.

This effect of chirp rate on the magnitude of the Lamb dip was previously observed by Hamadani *et al.* in a low pressure sample of NH_3 pumped with a high power N_2O laser [71]. In their study they found that at an appropriately high chirp rate the Lamb dips switched into amplification (*i.e.* from absorption to emission) indicating an inversion of population. This is direct evidence for adiabatic rapid passage (ARP) where the definition of 'rapid' is that the laser is swept through resonance in a time period that is short compared to the collisional relaxation of the gas. In their study the laser intensity was significantly higher (5 W cm^{-2}) than in

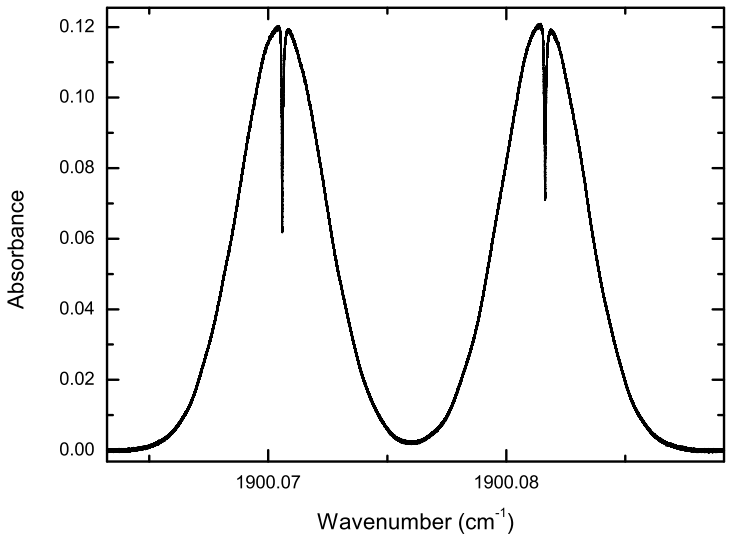

a)

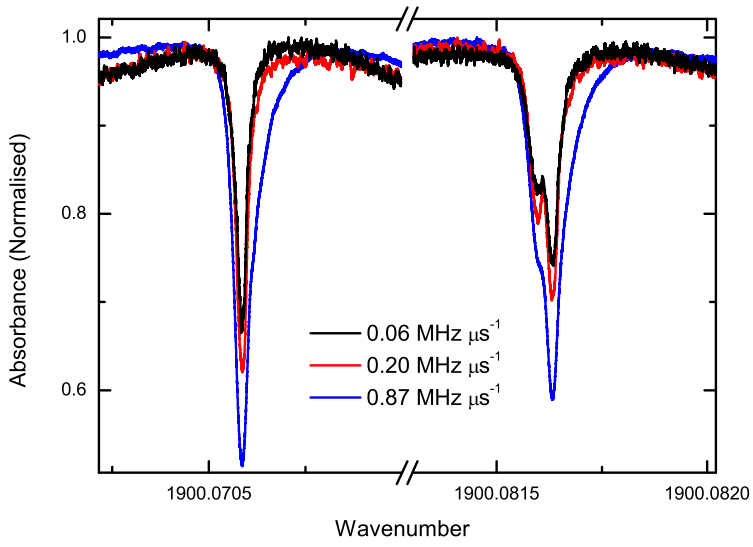

b)

Figure 3.17: The full Doppler profile for the e and f components of the R(6.5)$_{\frac{1}{2}}$ transition with two Lamb Dips is shown in a) for the R(6.5)$_{\frac{1}{2}}$ transition at a chirp rate of 0.87 MHz µs^{-1}. The effect of increasing chirp rate on the size of the Lamb dip is shown in b) with the depth of the dip increasing as the chirp rate is increased.

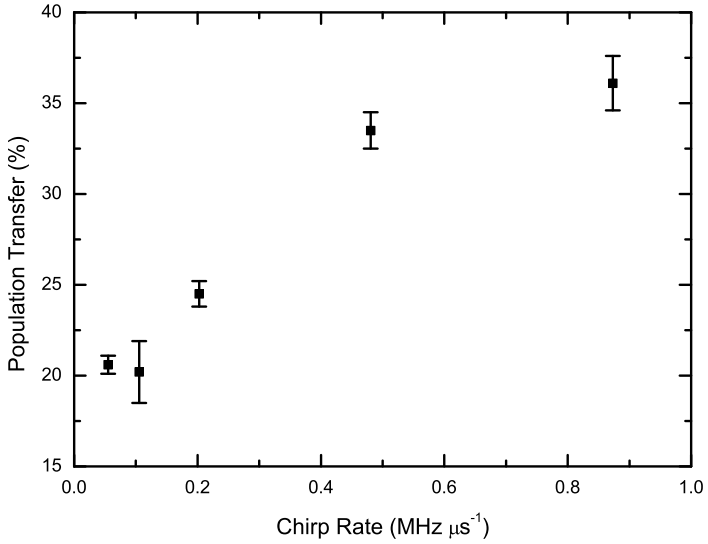

Figure 3.18: Population transfer as a function of chirp rate.

the present study (1 W cm^{-2}), and the dipole moment of their chosen transition was larger at 0.191 D compared with 0.053 D for the transition here studied, explaining why amplification is not seen in our data.

Raising the chirp rate above about 0.9 MHz μs^{-1} however did not lead to further increases in the magnitude of the Lamb dips and in fact they became noticeably asymmetric. The absorbance post-resonance in the probe scan becomes lower than expected for the Doppler profile as shown in figure 3.19. This asymmetry is independent of the direction of frequency scan, *ie.* for the case of a frequency up chirp it occurs to higher frequency than the line centre but on a down chirp the asymmetry lies to lower frequency. The magnitude of the Lamb dip now decreases with increasing chirp rate as the asymmetry increases. The cause of this asymmetry relates to the counter-propagating nature of the experiment. As the probe laser passes through the centre of the Doppler broadened line where $\omega_{probe} = \omega_0$ it begins to interact with velocity groups that have already been pumped. These velocity groups have a significant amount of population in the $v = 1$ state when pumped. The population of the $v = 1$ state decays in the time period between being pumped and being probed but if this time period is short enough then little decay occurs.

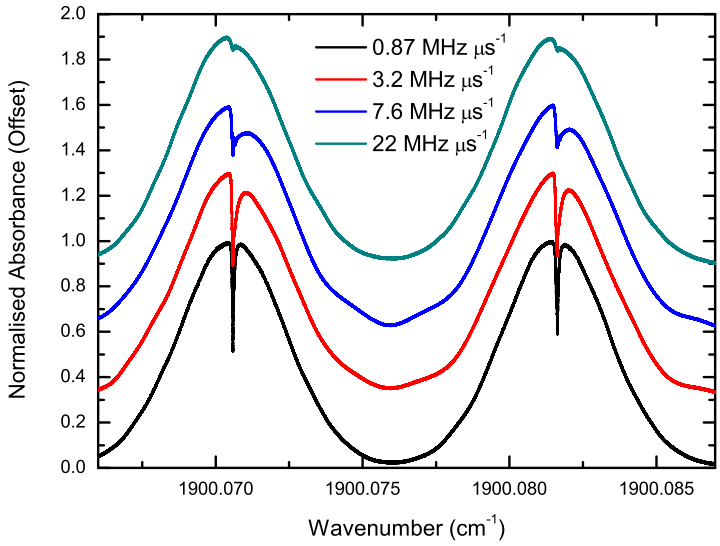

Figure 3.19: Increasingly asymmetric Lamb dip spectra are seen as the chirp rate is increased. All data was taken with 10 mTorr NO and data sets have been offset for clarity.

Hence the population difference in each velocity group ΔN, to which the absorbance is proportional, is reduced compared to those velocity groups that are probed pre-Lamb dip resonance, thereby reducing the absorbance. The length of time between pumping and probing for each velocity group depends on the chirp rate of the laser, thus the faster the laser is scanned, the less time the population in the $v = 1$ state has to decay. This behaviour should be expected to be observed in a system in which the main method of depopulating the upper state is molecular collisions.

As well as a change in the asymmetry with chirp rate, there is a noticeable change with pressure as shown in figure 3.20. The dips get smaller and the spectra more symmetric with increasing pressure, reflecting the increasing importance of collisional relaxation of the $v = 1$ population. In figures 3.19 and 3.20 the Doppler broadened absorption profiles have been normalized to show how the size of the dip changes relative to the background absorption.

The asymmetric line shape, to a first approximation, can be thus fitted using

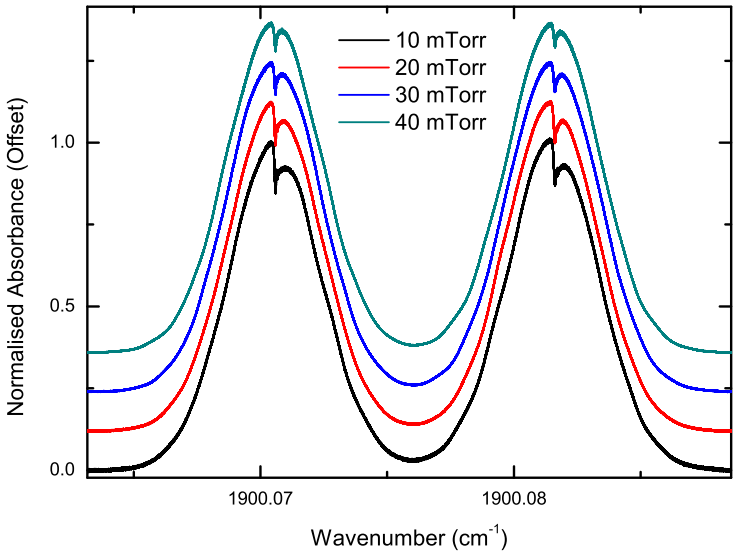

Figure 3.20: The variation in the asymmetric Lamb dip spectra as a function of pressure. As the pressure increases the dips get smaller in proportion to the background absorption profile and become more symmetric. All data was taken at laser chirp rate of 7.7 MHz µs^{-1} and the profiles were normalized and offset for clarity.

equation (3.5),

$$\alpha = \begin{cases} \alpha_0 & t \leq 0 \\ \alpha_0 \left(1 - Ae^{-kt}\right) & t > 0 \end{cases}, \tag{3.5}$$

where $t = \frac{\omega - \omega_0}{r}$ is the time taken between a velocity group being pumped and the probe laser interacting with it, and r is the chirp rate of the laser. A is proportional to the initial amplitude of the Lamb dip, and k is a phenomenological decay constant which quantifies depopulation (and dephasing) of the upper state. Equation (3.5) was convolved with a Gaussian of full-width at half-maximum 800 kHz, representing the laser linewidth function and fitted to the data using least squares fitting in a MATLAB program. An example fit to the e component of the R(6.5)$_{\frac{1}{2}}$ transition at a chirp rate of 18 MHz µs^{-1} is shown in figure 3.21 and shows very good agreement with the overall shape of the absorption line. The decay constant, k, is found to be approximately equal to the collision frequency within the gas sample.

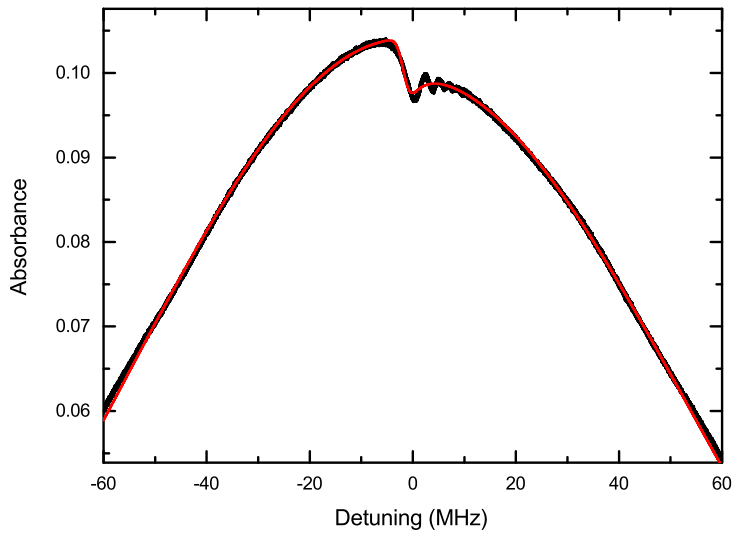

Figure 3.21: A fit to the e component of the $R(6.5)_{\frac{1}{2}}$ transition at a chirp rate of $18\,\mathrm{MHz\,\mu s^{-1}}$ using equation (3.5). The oscillatory structure seen post resonance resembles rapid passage signals as seen using pulsed QCL systems.

3.4.4 Rapid Passage

A closer examination of the Lamb dip reveals oscillations post-resonance is shown in figure 3.21. These oscillations occur *only* after the probe laser has scanned through the line center, to later time in the scan. As with the asymmetric lineshape the oscillations are seen to later time regardless of whether the probe laser is scanning to increasing or decreasing frequency. The oscillatory structure resembles the rapid passage signals seen using chirped pulsed QCLs; the electric field produced by the polarized vibrationally excited molecules interferes with the electric field of the scanning probe laser and causes the measured intensity oscillations. The process happens on a timescale that is short compared with the relaxation time of the system and as such the rapid passage does not appear at very slow laser scan rates below about $4\,\mathrm{MHz\,\mu s^{-1}}$. The rapid passage signature is only visible due to the sub-Doppler laser bandwidth causing significant velocity selection as no such rapid passage occurs when the pump beam is blocked, removing the velocity selective pumping. Because the velocity spread of the pumped molecules is very low (being determined by the laser linewidth) the molecules dephase slowly. Hence even though

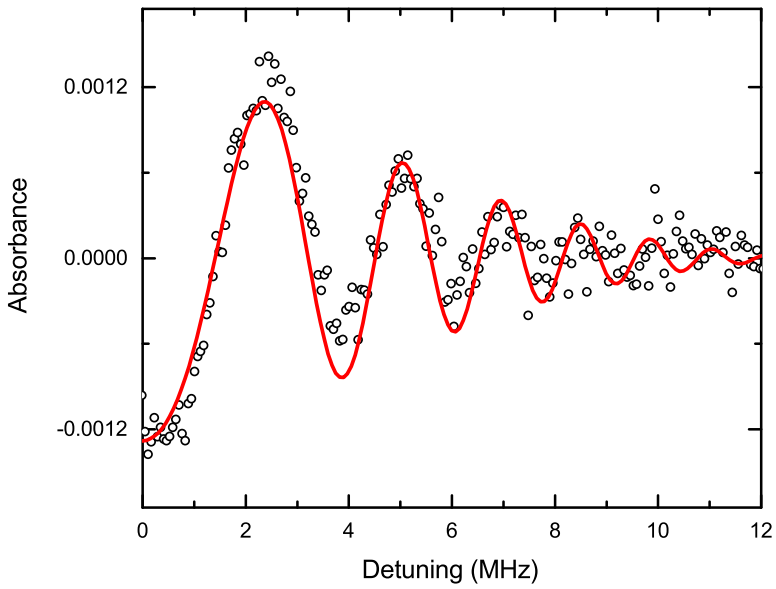

Figure 3.22: The post-resonance data presented in figure 3.21 with the fit using equation (3.5) subtracted. The behaviour of the system was modelled using the optical Bloch equations and the output is shown in red. The agreement with the experimental data is very good.

the laser is scanned slowly compared to the chirp rate of pulsed QCLs (ca. 3 - 4 orders of magnitude difference), the scan is still fast compared with the dephasing time of the pumped velocity group and rapid passage can be observed.

This behaviour has been modelled by solving the optical Bloch equations (2.56) using a MATLAB program [78]. The model takes the properties of the molecular transition such as the dipole moment and longitudinal and transverse relaxation rate constants, and the laser intensity and interaction length and produces a simulation of the expected rapid passage oscillations. Figure 3.22 shows the same data as in figure (3.21) with the fit using equation (3.5) subtracted. The output of our optical Bloch equation model has been applied to the oscillations shown in figure 3.22 and shows good agreement with the experimental data.

The rapid passage signals for the e and f components of the $\mathrm{R}(6.5)_{\frac{1}{2}}$ transition were found to differ in appearance. Moreover, it is seen that the observed difference changes depending on the chirp rate of the laser. In general the observed signal on the e component looks as expected for rapid passage, however on the f component

there is a marked difference; this difference in structure is attributed to the hyperfine splitting. In the e component the signals appear like normal rapid passage signals which oscillate inside a damping envelope. However the f component signals display a distortion from this form. A comparison between the signals measured for the e and f components is shown in figure 3.23. In the f component the splitting as shown in figure 3.16 is sufficiently large that a rapid passage signal beginning on the partially resolved hyperfine transition may be slightly out of phase with that originating from the other two hyperfine transitions. Hence these two signals interfere and cause the change in overall signal shape that is observed. Again this effect was modelled using the optical Bloch equations (2.56) as shown in figure 3.23. The three hyperfine transitions on each Λ-doublet each contribute an oscillating rapid passage signal. These signals are summed and then convolved with a Gaussian with a full width at half maximum of 1 MHz to represent the probing laser linewidth. The results of the simulations are shown in figure 3.23 c) and f) (for the e and f components respectively) and are in good qualitative agreement with the experimental data shown in 3.23 a) and d). It should be noted that these experimental data had the underlying asymmetry subtracted using the best fit from equation (3.5). In addition, the simulations are in good agreement with the chirp rate dependence and shape of the experimental data for both Λ doublet components.

3.4.5 Single velocity group pumping

As stated in section (2.2.3) it is not possible to observe a Bennett hole at any frequency other than the line centre using only one laser. Similarly it is also due to the use of the same laser for pumping and probing that asymmetric lineshapes are observed in our experiments. In order to observe the Bennett hole for velocity groups that have a non-zero component in the direction of laser propagation it is necessary to use two lasers in order to separate out the pumping and probing. To achieve this a second laser was used as the pump. This laser was a Daylight Solutions external cavity QCL (EC-QCL), widely tunable through the use of proprietary electronics

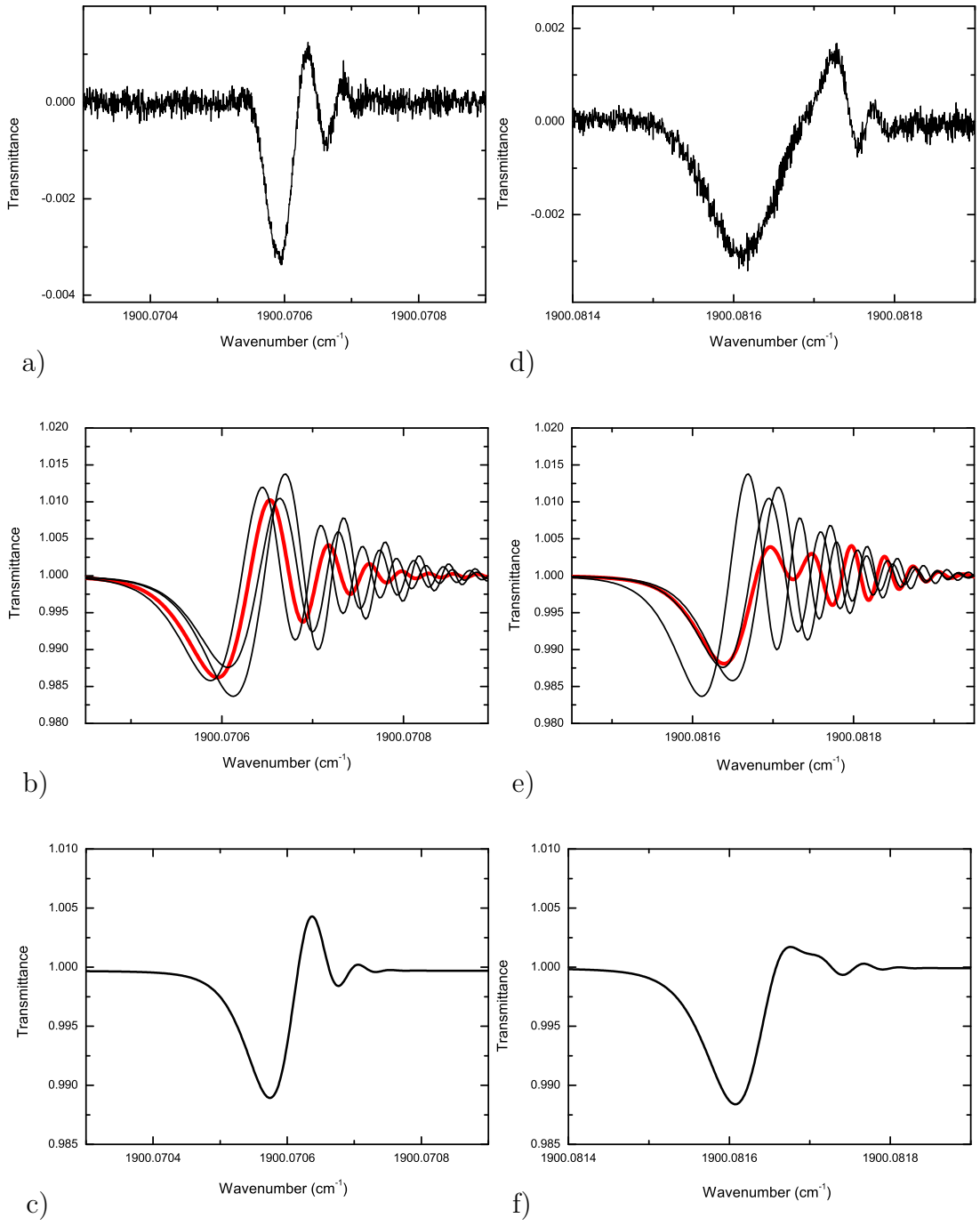

Figure 3.23: Rapid passage signals at a laser chirp rate of 7.7 MHz μs^{-1} and a pressure of 9 mTorr for the $R(6.5)_{\frac{1}{2}}$ transition. a) to c) correspond to the e component and d) to f) to the f component. The experimental data is shown in a) and d) with the asymmetric Doppler profile subtracted. Images b) and e) show the simulations of the rapid passages signals for the three hyperfine components of the respective transitions along with their sum in bold. Finally c) and f) show the signal expected at the detector, calculated by convolving b) and e) with a Gaussian function representing the probe laser linewidth.

supplied with the laser. The external cavity gives this laser a tuning range much greater than the DFB laser, being able to tune between 1776 cm^{-1} and 1962 cm^{-1}, whilst emitting up to 150 mW of optical power. The two beams counter propagated through the same cell as previously used with the EC-QCL tuned to a fixed frequency within the $R(6.5)_{\frac{1}{2}}$ transition and emitting 124 mW. The output frequency of the EC-QCL is set by the angle of a grating in the external cavity which can be tuned through the application of a driving voltage to a piezoelectric transducer (PZT) that is attached to the grating. In order to provide fine adjustment of the output frequency within the Doppler profile of the transition a small DC voltage was applied to the PZT and altered by means of a potentiometer. The DFB laser was scanned over the entire Λ-doublet at a rate of 19 MHz μs^{-1} in the manner previously described. It is noted that even though the scan rate of the laser is greater than that shown to be necessary to see asymmetry in a Lamb dip experiment, no asymmetry is seen in these spectra. A polariser was used to attenuate the output of the DFB laser to 2 mW to reduce saturation effects of the probe laser.

At this tuning rate no rapid passage occurs and because the pump laser is set at a fixed output frequency the asymmetry associated with the finite population decay time is not seen. It was possible to observe Bennett holes across the entire Doppler profile at a pressure of 10 mTorr of NO. Some of these are shown in figure 3.24 and show that the absolute depth of the Bennett hole is proportional to the number of molecules in the relevant velocity group. Due to instabilities in the output frequency of the pump laser it was not possible to average these spectra and the data shown are from single scans over the absorption feature.

The equation used for fitting the Lamb dips, equation (2.25), being a modified form of equation (2.24) clearly only applies in the case where a single laser is used both to pump and probe the transition and thus the dip is always seen at the line centre. For the direct observation of a Bennett hole equation (2.24) is modified

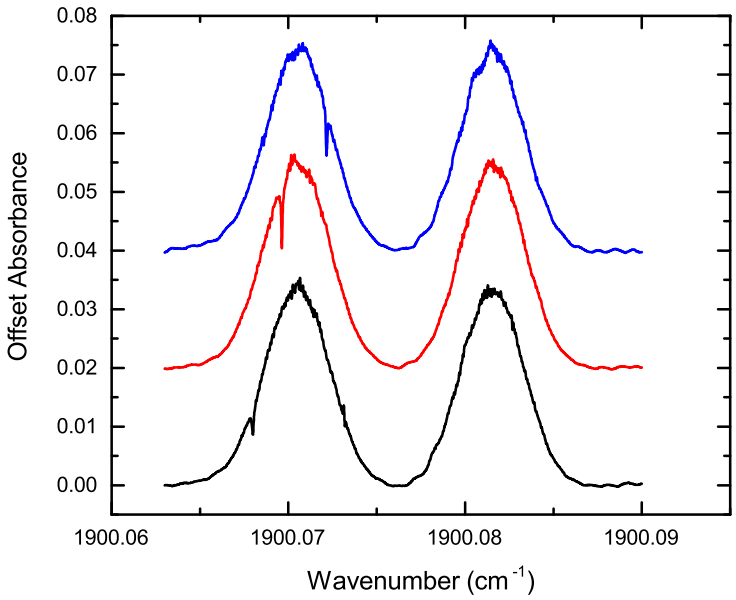

Figure 3.24: Examples of Bennett holes burnt into the e component of the R(6.5)$_{\frac{1}{2}}$ Λ-doublet. Since separate lasers are used to burn the hole in the population and to measure the absorbance it is possible to see the Bennett hole at frequencies other than the line centre of the Doppler broadened transition. These data are not averaged and hence display higher noise than previously shown data.

slightly to

$$\alpha = \alpha_p e^{-\left(\frac{\omega-\omega_0}{\Delta_D}\right)^2}\left[1-\left(1-\frac{1}{\sqrt{1+S_0}}\right)\frac{\Gamma^2}{\Gamma^2+(\omega-\omega_B)^2}\right]. \tag{3.6}$$

Here ω_B is the optical frequency at which the transition is being pumped. Convolution with the laser linewidth function then allows the measured spectra to be fitted as shown in figure 3.25. This shows a Bennett hole burnt into the e component of the Λ-doublet which is well fit using equation (3.6). As with the fits to the Lamb dip spectra shown earlier in this chapter, all six hyperfine lines were taken into account to fit the overall lineshape. The fit suggests a population transfer of 28% which is comparable to that seen in the Lamb dip experiments.

Given this interpretation of the data, it should be possible to see rapid passage oscillations without the asymmetry by using a separate laser to pump a single velocity group within the Doppler profile. To this end a single velocity group within

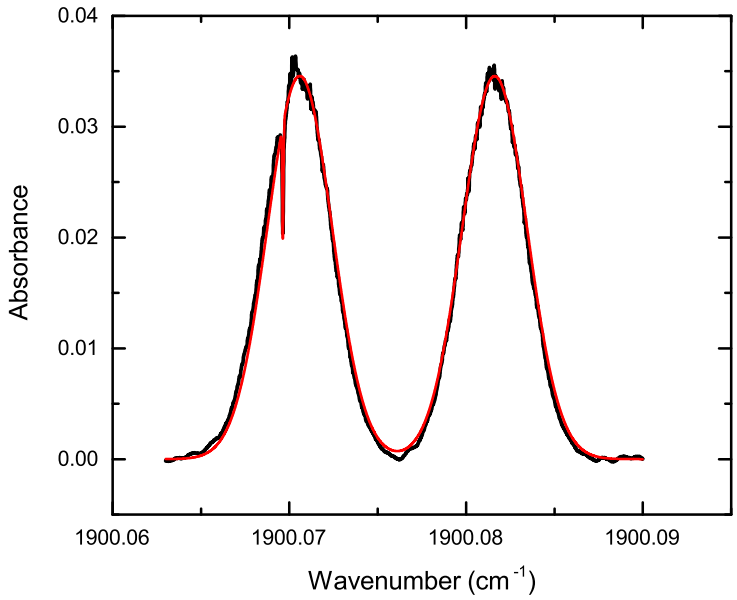

Figure 3.25: A Bennett hole burnt into the e component of the Λ-doublet of the $R(6.5)_{\frac{1}{2}}$ transition in 10 mTorr of NO. The fit returns a population transfer of 28%. Again the data is not averaged and so appears noisier than previously shown data.

the Doppler profile of the $R(6.5)_{\frac{1}{2}}$ transition was pumped using a fixed frequency supplied by the external cavity QCL [124].

Increasing the scan rate of the probe laser to 60.5 MHz µs^{-1} it was possible to observe rapid passage on a Bennett hole without the underlying asymmetry associated with a single laser Lamb dip type experiment. The asymmetry in the Doppler profile is due to the simultaneous frequency scan of pump and probe beams in a counter-propagating setup with significant population transfer induced by the QCL, while the rapid passage oscillations are due to the induced polarisation of the pumped molecules beating with the chirping laser field. Again due to frequency instability of the pumping external cavity QCL it was not possible to perform any averaging on the recorded data, however the lack of asymmetry in the Doppler profile makes the rapid passage oscillation even more pronounced. Figure 3.26 shows a velocity group with a small component in the direction of laser propagation being pumped within the f component of the Λ doublet resolved transition. Rapid passage oscillations are clearly seen however the asymmetry caused by pumping all velocity sets before

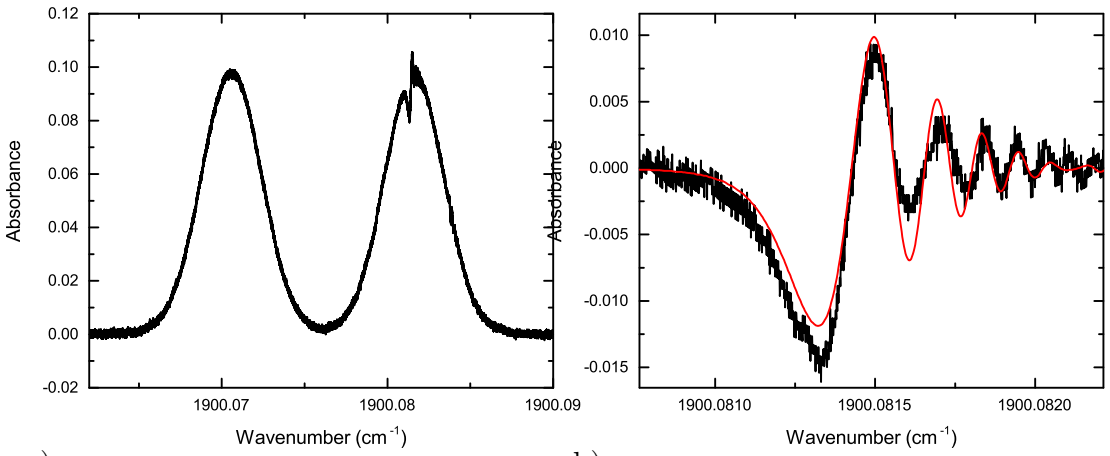

Figure 3.26: The absorption signal seen (a)) when a separate fixed frequency (Daylight) QCL is used to pump a single velocity group within the R(6.5)$_{\frac{1}{2}}$ transition. The pumped velocity group has a non-zero, small velocity component in the direction of propagation and so the dip caused by the hole burnt into the ground state population is not centered within the Doppler profile. b) shows a fit to the rapid passage oscillations using using the optical Bloch equations.

probing them is not.

The external cavity laser, used here as the pump, has a linewidth of *ca.* 2 MHz as determined previously using Lamb dip spectroscopy [21,124]. Therefore the velocity group pumped by this laser is slightly larger than that pumped by the Maxion laser in the single laser Lamb dip experiments. Again the optical Bloch equations were solved to model the behaviour of the system and the resulting simulation is shown in figure 3.26 b). Once more the agreement is good.

3.5 Conclusions

In this chapter a high power distributed feedback continuous wave quantum cascade laser was characterised by measuring its electrical properties as well as its optical output properties. The output frequency range was measured using Fourier transform Infra-red spectrometry. The spectroscopy of NO (a strong absorber in the output frequency range of the laser) was explained and the laser was used to perform direct spectroscopy which showed the power saturation of a single ro-vibrational transition.

The linewidth of the laser was determined to be 800 ± 60 kHz through Lamb dip spectroscopy. The effects of rapid passage on Lamb dips were investigated and initially increasing chirp rates were found to favour population transfer, in good agreement with Hamadani's work on adiabatic rapid passage with a chemical laser in which the efficiency of the population transfer from the initial state into the excited vibrational state can be controlled by the laser chirp rate [71]. Whilst amplification was not observed, population transfer efficiencies of up to 35% were measured which could be controlled by the laser chirp rate. Increasing the chirp rate further has allowed for rapid passage effects to be demonstrated in a Lamb dip experiment using a narrow linewidth, high power single mode quantum cascade laser.

The absorption signals were observed to display asymmetric lineshapes, owing to the rate at which the probe laser is chirped through resonance with previously pumped velocity groups. If this rate is much higher than the rate at which the upper state is depopulated then an asymmetric lineshape results reflecting the degree of initial population transfer. This same condition is also necessary to observe rapid passage oscillations on the Lamb dip. The RP oscillations were only observable due to the narrow laser linewidth and their structure is affected by the hyperfine splitting in the transition. Finally it was shown that it was possible to remove the asymmetry effect from the spectra by pumping a single velocity group using a second laser at a fixed frequency. By this method it was possible to observe hole burning across the Doppler profile and to observe rapid passage within the Doppler profile but without the asymmetry associated with the single laser experiment. All of the experimental data are well corroborated by simulations based on the two-level optical Bloch equations which were introduced in chapter 2.

Chapter 4

Pump-Probe Spectroscopy with CW QCLs

The final experiments presented in chapter 3 began to incorporate two separate QCLs in a counter-propagating experimental arrangement to perform velocity selective saturation experiments on a single rotational-vibrational transition within the $v = 1 \leftarrow 0$ band of NO. This chapter utilises the extended tuning ranges of the two lasers to perform pump-probe type experiments over pairs of ro-vibrational transitions covering the $v = 1 \leftarrow 0$ and $v = 2 \leftarrow 1$ bands. The velocity selective pumping demonstrated in chapter 3 allows the observation of rapid passage effects in the probe beam when interrogating the ladder state (see figure 2.9). The effects of varying both the rate at which the probe laser is chirped and the gas pressure will be investigated. In addition, a noise source was applied to one of the lasers in order to broaden its linewidth with direct consequences for the observation of RP oscillations. These results corroborate our conclusions regarding the importance of velocity dephasing given in chapter 3. Two-colour polarisation spectroscopy is also demonstrated, with a two-detector methodology allowing observation of both the absorption and the dispersion of the velocity selected sample. Finally some of the results of the chapter will be simulated using a three-level model based on the density matrix equations of chapter 2.

4.1 Hot Band Rapid Passage from a Velocity Selected Sample

In the final part of chapter 3 two QCLs were used with one being used to pump a sub-Doppler velocity group within the $v = 1 \leftarrow 0$ ro-vibrational transition of NO, and the other scanned over the full Doppler profile of the same transition. The operating range, particularly of the EC-QCL, which outputs light between 1776 cm^{-1} and 1962 cm^{-1}, allows these lasers to be tuned such that one pumps a rotationally resolved transition within the fundamental vibrational band whilst the other, probe laser, is tuned to the corresponding ladder state transition in the $v = 2 \leftarrow 1$ hot band. Furthermore, as the lasers both have similar powers, the lasers can each be used as the pump and the probe on different transitions. For example, the DFB-QCL is able to pump the R(5.5) and R(6.5) transitions originating in both spin-orbit states. It is also able to act as the probe investigating the R(15.5) and R(16.5) transitions, again in both spin-orbit states. The EC-QCL has a tuning range that covers all of these transitions as well as the appropriate ladder state transitions. For example if the DFB-QCL is used to pump the $\mathrm{R}(6.5)_{\frac{1}{2}}$ transition, the EC-QCL may be tuned to the $\mathrm{R}(7.5)_{\frac{1}{2}}$ hot band transition or the $\mathrm{P}(7.5)_{\frac{1}{2}}$ hot band transition. If the DFB-QCL is used to probe the $\mathrm{R}(15.5)_{\frac{3}{2}}$ hot band transition then the EC-QCL would be tuned to the $\mathrm{R}(14.5)_{\frac{3}{2}}$ fundamental or the $\mathrm{P}(16.5)_{\frac{3}{2}}$ fundamental transition.

The two lasers have different linewidths with the DFB-QCL having a linewidth of 800 kHz as measured by Lamb-dip spectroscopy in the previous chapter. The EC-QCL has a linewidth of 2 MHz as measured in previously published work [21,123–125] meaning that when used as the pump laser, the EC-QCL pumps a velocity group more than twice as wide (in frequency space) as would the DFB-QCL. Both lasers were therefore used to pump the fundamental transition in order to demonstrate the effects of this increased velocity sampling.

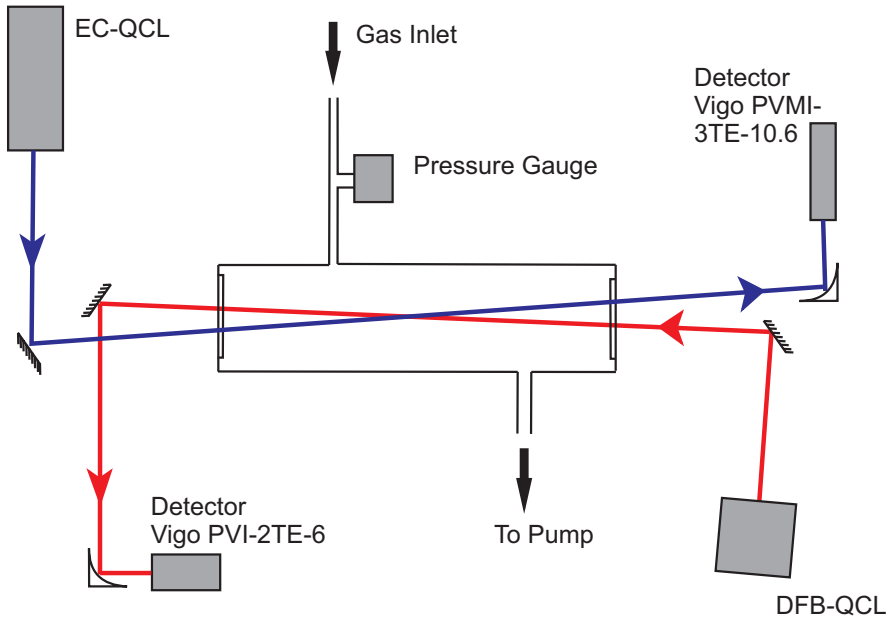

Figure 4.1: Schematic of the experimental setup. The lasers counter-propagate through an 84 cm long gas cell filled with a low pressure of NO and the signals are monitored by focusing with off axis parabolic mirrors onto HgCdTe detectors.

4.1.1 Experimental

The two laser beams counter-propagate with a small uncrossing angle (*ca.* 0.5°) through an 84 cm long absorption cell containing a low pressure of NO gas (5 - 500 mTorr). After passing through the cell both beams are focussed by off-axis parabolic mirrors onto two 20 MHz bandwidth thermoelectrically cooled mercury cadmium telluride detectors, the EC-QCL onto a VIGO PVMI-3TE-10.6 and the DFB-QCL onto a VIGO PVI-2TE-6, see figure 4.1.

When the EC-QCL was used as the pump laser, its frequency was scanned by applying a sine wave modulation (at a frequency in the range 5 to 40 Hz) to the piezo-electric transducer (PZT) attached to its external grating. This modulation signal was derived from a TTi function generator (TG230) and resulted in (near) linear laser chirp rates in the range 20 to 150 $\mathrm{Hz\,ns^{-1}}$ (measured using a 500 MHz etalon). In this case, a triangular current modulation was then applied to the DFB laser using a second TTi function generator (TG1304) with frequency ramps selected from the range 10 kHz to 75 kHz. Within a single current sweep, the total

frequency scan range was 1.6 GHz, producing chirp rates ranging from 30.5 kHz ns^{-1} to 265.5 kHz ns^{-1}. The three orders of magnitude ratio between the two laser chirp rates implies that the pump laser remains quasi-static during a single frequency scan of the probe laser. In some experiments the roles of each laser were reversed and the corresponding chirping conditions will be presented later in the text as appropriate. The PZT in the EC-QCL cannot respond to high frequency signals (> 100 Hz) and so in order to modulate the output frequency to produce the chirp rates required to see rapid passage, it is necessary to apply the modulation signal to an internal bias tee which modulates the driving current to change the frequency output.

The absorption signals from both lasers are collected and recorded by a 2.5 gigasample/s, 400 MHz bandwidth digital oscilloscope (LeCroy Wavesurfer 44MXs-A). During each frequency scan of the pump laser, which encompasses the fundamental absorption transition, a pre-selected number of probe laser scans are recorded and averaged in order to increase the signal to noise ratio. A MATLAB program is used to separate the data taken on the frequency up chirps from the down chirps. The individual sweeps are then aligned onto the most intense spectral feature. This process accounts for small drifts in the probe laser frequency as well as small amounts of phase instability in the function generator output.

4.1.2 Results: Rapid Passage from a Velocity Selected Sample

In all of the experiments, the pump and probe lasers share a common intermediate state. As a first example, consider the case where the R$(14.5)_{\frac{1}{2}}$ $v = 1 \leftarrow 0$ transition of NO was pumped using the EC-QCL while the DFB laser probed the R$(15.5)_{\frac{1}{2}}$ $v = 2 \leftarrow 1$ transition. Figure 4.2 shows the multiple scans of the probe laser as the pump laser is tuned slowly over the Doppler profile of the fundamental transition. The data shown are obtained at a pressure of 50 mTorr. Throughout the Doppler broadened absorption profile, the narrow bandwidth (~ 2 MHz) pump laser excites a velocity group within the NO gas sample into the $v = 1$ level according to equation (2.3). As shown in figure 4.2 i-iii, the magnitude of the transient absorption signals

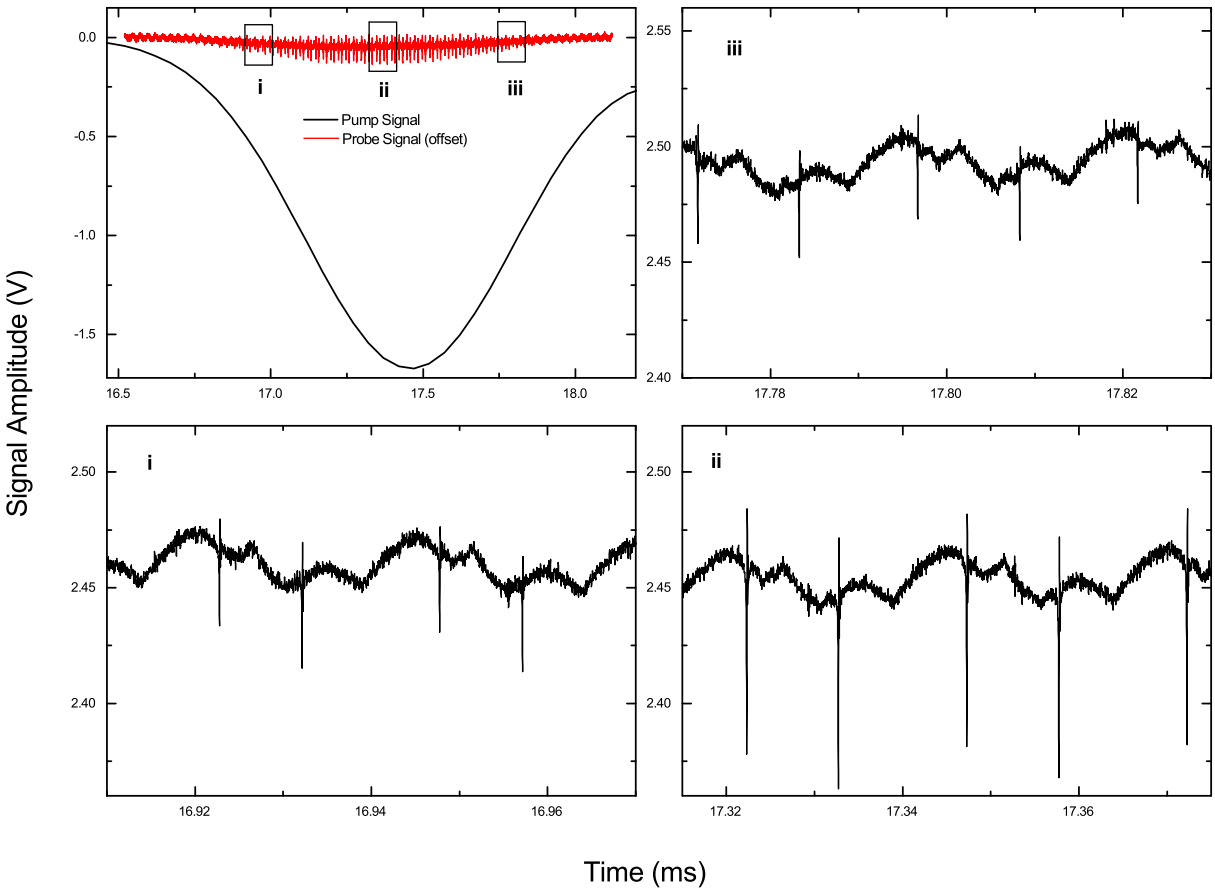

Figure 4.2: Example signals obtained from the probe scan as the pump laser is slowly tuned across the Doppler profile of the R(14.5)$_{\frac{1}{2}}$ $v = 1 \leftarrow 0$ transition of NO. The amplitude of the rapid passage signals mirrors the instantaneous magnitude of the absorbance of the pump. The decay period of the oscillations is constant regardless of the amplitude. The data shown was taken at a pressure of 50 mTorr.

measured by the probe are directly related to the frequency dependent absorption induced by the sub-Doppler pump laser. The amplitudes of the rapid passage signals is therefore proportional to the number of molecules being pumped into the $v = 1$ state. When the pump laser is off-resonance with the $R(14.5)_{\frac{1}{2}}$ transition, no transient signal is observed in the probe scan. The bandwidth of the pump laser is sufficiently small compared to the frequency separation between transitions probing different Λ-doublets of the ground rovibrational level that the e and f components can be considered separately. It can be seen in figure 4.2.i-iii that there is significant baseline noise as the probe laser is scanned over a range of 1 GHz, and this is due to the weak optical feedback from uncoated optics that propagate back into the laser and etalons formed by the front window of the detector. However, the periodicity of these effects is sufficiently different from that of the transient absorption signals to be discriminated and not to affect the conclusions of the work.

Figure 4.3 shows a zoom in on a single transient signal captured by the probe laser over a reduced time period of *ca.* 1 µs, and the transient signal after being averaged over the full Doppler width of the transition. Both signals show clear oscillatory structure characteristic of rapid passage. The averaged signal, derived from 50 individual sweeps of the probe laser, retains the characteristics of the single sweep, the oscillations being in phase and having the same coherence lifetime - see later. The averaging does result in a lower overall amplitude than for the single shot data, which was taken with the pump laser pumping close to the absorbance maximum, but improves the signal to noise ratio by a factor of approximately 7 (the square root of the number of averages). The coherent excitation produced by the pump laser results in a polarised ensemble of velocity selected molecules. When the probe laser comes into resonance with the pumped velocity group, these vibrationally excited molecules interact with the probe field to generate the transient signal. RP occurs when the probe laser radiation is swept through the molecular transition in a time period which is fast compared with the relaxation time for the system. The probe field then induces an oscillating polarization density within the vibrationally

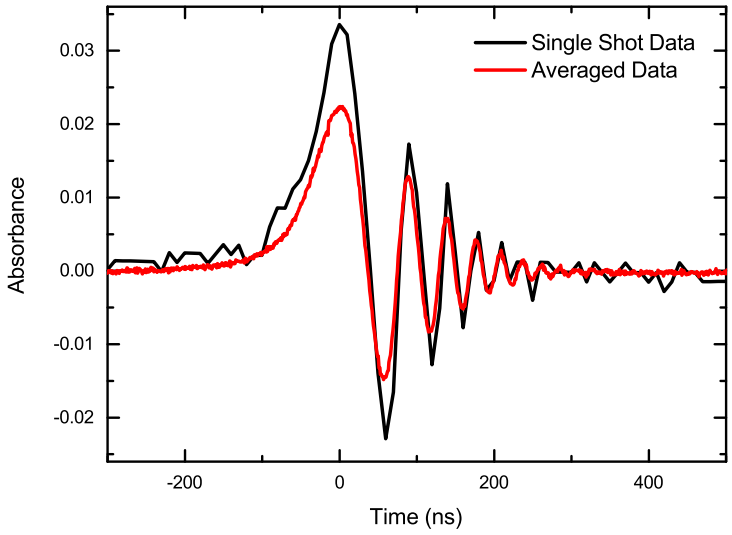

Figure 4.3: Rapid passage signal for 50 mTorr of NO obtained at a pump chirp rate of $0.149\,\mathrm{kHz\,ns^{-1}}$ and a single pass of the probe at a scan rate of $145.5\,\mathrm{kHz\,ns^{-1}}$. The averaged signal is derived from 50 individual sweeps of the probe laser through resonance and shows that both the overall shape and the decaying oscillatory structure are unaltered by the averaging process.

excited subset of molecules which interferes with the electric field of the swept laser radiation and leads to asymmetric absorption profiles [71].

The averaged RP traces were suitable for fitting in order to determine the RP decay time and to this aim, the functional form given in equation 4.1 was used, in which k is the probe laser chirp rate and τ is a phenomenological decay constant [78, 126].

$$A(t) = A_0 e^{\frac{-t}{\tau}} \sin\left(\frac{k}{2}t^2\right) \tag{4.1}$$

The function applies only in the post resonance regime so does not fit the initial part of the absorption, but rather starts at the first absorption maximum. The fit of equation 4.1 to the experimental data was made using a Nelder-Mead simplex algorithm to extract a value for τ, as well as the associated errors calculated from the square roots of the diagonals of the covariance matrix.

An example of a fit to the averaged data is shown in figure 4.4 and the returned best fit value for τ is 112.4 ± 2.5 ns. The decay rate constant of the RP signal, $(\frac{1}{\tau})$, is determined by both the decay rate of the population in the upper state and

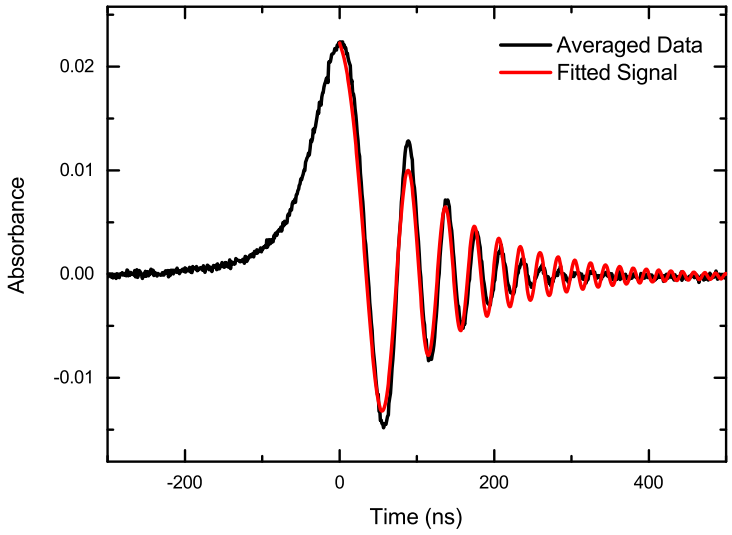

Figure 4.4: Averaged rapid passage signal from figure 4.3 shown with a fit using equation (4.1). The equation accurately fits the form of the rapid passage and returns a decay period of $\tau = 112.4 \pm 2.5$ ns.

the decay rate of the dipole moment polarisation, with rate constants $\frac{1}{T_1}$ and $\frac{1}{T_2}$ respectively [67]. At pressures of a few tens of mTorr, the average time between collisions is a few µs and is comparable to the time taken for the probe laser to complete one frequency up or down scan. This time period is an order of magnitude longer than the timescale over which RP signals are observed. Therefore the decaying shape of the RP signal is predominantly determined by dephasing of the dipole moment polarisation rather than by collisional relaxation. The fits return values for the decay constant τ, with the oscillation frequencies being determined by the (known) chirp rate of the probe laser. In the following subsections the effect of probe laser chirp rate and gas pressure on the decay period of the rapid passage signal are investigated with a general decrease in coherence time being shown as both parameters are increased.

4.1.3 Effect of laser chirp rate

The effect of varying the chirp rate of the probe laser on the RP signals was investigated. Firstly the EC-QCL pump laser was set to scan over the $\mathrm{R}(14.5)_{\frac{1}{2}}$ $v = 1 \leftarrow 0$

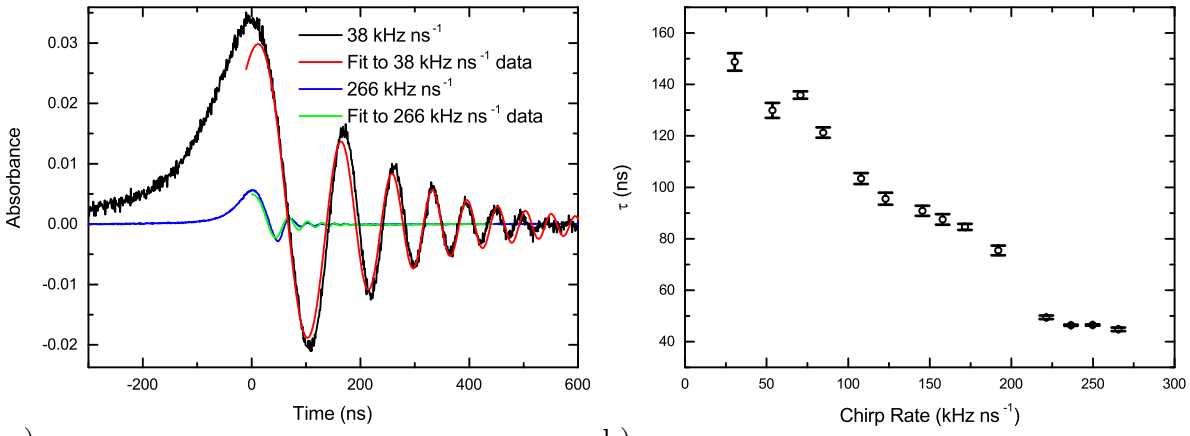

Figure 4.5: a) Rapid passage signals and the corresponding best fits for probe chirp rates of 38 kHz ns^{-1} and 266 kHz ns^{-1} with a pressure of 50 mTorr of NO. b) Decay constants obtained from the fitting of the experimental rapid passage signals as a function of probe laser chirp rate using equation (4.1).

transition at a rate of 0.149 kHz ns^{-1} and an output power of 80 mW. The DFB-QCL was used as the probe at a power of 66 mW and chirped at a selection of rates within the range 30 to 266 kHz ns^{-1}. As can be seen in figure 4.5 a) the amplitude of the RP signals decreases as the probe chirp rate is increased. Effectively, the probe electric field couples less efficiently to the transition dipole moment for the R(15.5)$_{\frac{1}{2}}$ $v = 2 \leftarrow 1$ hot band transition, resulting in the measured transient absorption being reduced. A similar effect is seen when working with pulsed QCL systems [127].

The post resonance parts of the transient signals are well fit by equation (4.1) to yield reliable decay constants, τ. The set of measurements shown in figure 4.5 b) indicates the decrease of τ as the chirp rate increases and reflects the fact that the probe laser interacts with a progressively larger range of velocity groups per unit time, leading to more rapid Doppler dephasing of the RP signal. Furthermore, as the probe chirp rate increases, τ decreases to a lower limit of *ca.* 50 ns; this is the limit imposed by the 20 MHz bandwidth of the detector.

In order to increase the degree of population transfer and minimise the Doppler dephasing of the RP signal, similar measurements have been conducted for which the function of each laser is reversed, *i.e.* the DFB-QCL becomes the pump and the EC-QCL, the probe. Due to the limited tunability of the DFB-QCL, the NO

transitions used in this case are different to those studied above. The pump laser was tuned to the $R(6.5)_{\frac{1}{2}}$ $v = 1 \leftarrow 0$ transition at $1900.1\,\mathrm{cm}^{-1}$ while the probe laser was scanned over the $P(7.5)_{\frac{1}{2}}$ $v = 2 \leftarrow 1$ band at $1822.3\,\mathrm{cm}^{-1}$. The powers of the pump and probe lasers were 201 mW and 116 mW respectively and the pressure in the cell was 50 mTorr.

The corresponding data for this case where the DFB is the pump and the EC-QCL is the probe is shown in figure 4.6 a). Here the pump scan rate was $0.036\,\mathrm{kHz\,ns}^{-1}$, while the probe was scanned at rates from 20 to $486\,\mathrm{kHz\,ns}^{-1}$. The decay constant, τ, again decreases as a function of increasing probe laser chirp reaching the aforementioned limit of about 50 ns at the highest chirp rate as shown in figure 4.6 b). However, in this case the limiting value isn't reached until the chirp rate is twice as large as before. In addition, the values of τ at low chirp rates are higher than those for which the EC-QCL was the pump, e.g. at a chip rate of $50\,\mathrm{kHz\,ns}^{-1}$ the τ values are 150 ns and 130 ns respectively. The variation of τ with probe laser chirp rate is also smoother than when using the EC-QCL as the pump laser. Both effects directly reflect the narrower linewidth and higher power of the DFB compared to the EC-QCL; in particular, the lower linewidth of the DFB-QCL pumps a narrow range of velocities which leads to a slower dephasing of the rapid passage signals.

Rapid Passage from the $\Omega = \frac{3}{2}$ Spin-Orbit State

The DFB-QCL was tuned to the $R(6.5)_{\frac{3}{2}}$ $v = 1 \leftarrow 0$ transition at $1900.5\,\mathrm{cm}^{-1}$ in which the hyperfine splitting is greater than in the transitions for which $\Omega = \frac{1}{2}$. In this case the EC-QCL was tuned to the $P(7.5)_{\frac{3}{2}}$ $v = 2 \leftarrow 1$ transition at $1821.4\,\mathrm{cm}^{-1}$. The pump laser was chirped at a rate of $0.055\,\mathrm{kHz\,ns}^{-1}$ with a power of 201 mW and the probe laser was scanned at rates between 11 and $259\,\mathrm{kHz\,ns}^{-1}$. The pressure of NO was again kept at 50 mTorr.

In chapter 3 it was shown that the differing hyperfine structure of the e and f components of the Λ-doublet resolved transitions led to differences in the measured

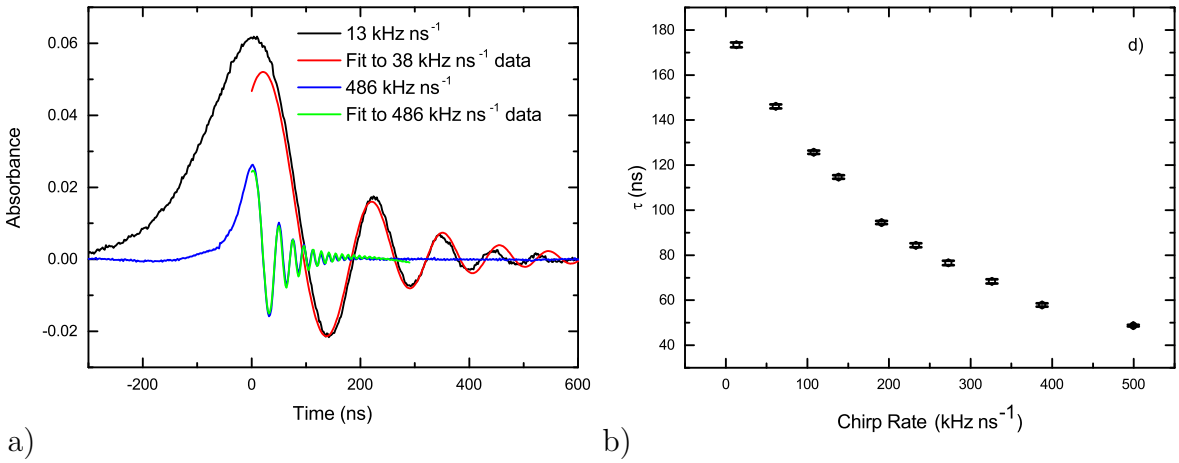

Figure 4.6: a) Rapid passage signals on the P(7.5)$\frac{1}{2}v = 2 \leftarrow 1$ hot band of NO and their fits taken at 50 mTorr of NO. b) The decay constants obtained by the fitting of the experimental rapid passage signals as a function of the chirp rate of the probe laser.

rapid passage structures. For the probe transition used here the splittings between hyperfine transitions are significantly larger than in the $\Omega = \frac{1}{2}$ spin-orbit state; in the f component the splittings between transition lines are 2.4 MHz and 2.6 MHz and in the e component they are 2.4 MHz and 3.2 MHz respectively. The f component transitions lie to slightly lower frequency than the e component transitions so for a frequency down-chirp the probe laser encounters these splittings in the opposite order to that given. These splittings are large enough that the rapid passage signals from each hyperfine component interfere significantly with each other. The level of interference is dependent on the chirp rate of the probe laser as shown by figure 4.7

It can be seen that at the highest chirp rates the rapid passage signals look like the rapid passage signals previously shown, however at slower chirp rates significant interference is seen. Similarly at the same chirp rates there is also a difference in the shape of the RP signals seen between the up and down-chirps which is indicative of the underlying hyperfine structures interacted with. It should be noted that the dephasing times are fast enough that the RP signals only derive from a single Λ-doublet component. These observations show the high resolution nature of our measurements.

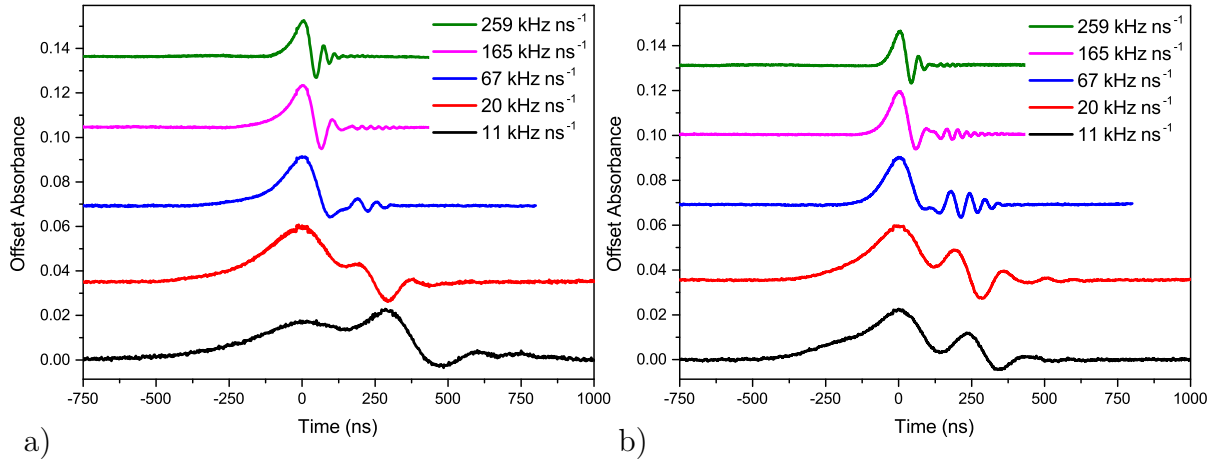

Figure 4.7: The averaged rapid passage signals from the P(7.5)$_{\frac{3}{2}}$ $v = 2 \leftarrow 1$ transition at various chirp rates as given in the insets. a) shows the data taken on the frequcney down-chirp and b) on the frequency up-chirp. The differences in the rapid passage shapes are due to the underlying hyperfine structure which differs between the up and down chirps as the splittings in the e and f components differ. The signals are offset for clarity.

4.1.4 Effect of sample pressure

The previously described experiment was repeated at several different NO pressures within the range 7.5 to 300 mTorr to investigate the effects of collisional dephasing on the system. In this case, the EC-QCL pump (tuned to the R(14.5)$_{\frac{1}{2}}$ fundamental) was chirped at 0.149 kHz ns^{-1} with a power of 81 mW, and the probe (tuned to the R(15.5)$_{\frac{1}{2}}$ hot band) chirped at 145.5 kHz ns^{-1} with a power of 41 mW. The maximum amplitude of the rapid passage absorption, A_0 (see equation(4.1)), is plotted as a function of pressure in figure 4.8. It can be seen that the signal amplitude rises sharply to a maximum around 50 mTorr before the increasing pressure causes it to fall again. This behaviour is due to the competition between the absolute number of polarised molecules interacting with the electric field and the collisionally induced dephasing. Both properties increase with increasing pressure with the collisional dephasing beginning to dominate beyond about 50 mTorr of NO.

As the pressure of NO increases, there are more collisions per unit time and collisions begin to make a greater contribution to the relaxation of the system. Hence, the magnitude of the oscillations within the RP signal decreases and so

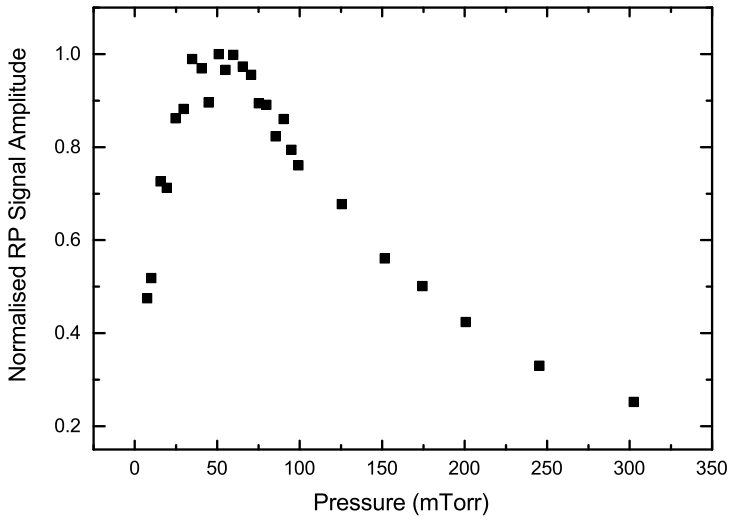

Figure 4.8: The maximum amplitude of the rapid passage absorption as a function of pressure. The data have been normalised to the largest absorption at around 50 mTorr.

does the decay time with increased pressure. This behaviour is shown in figure 4.9 a). In figure 4.9 b) the RP decay time as function of sample pressure for both the e and f components of the R$(15.5)_{\frac{1}{2}}$ $v = 2 \leftarrow 1$ probe transition is plotted showing the decrease in dephasing time with increasing pressure. In both cases at low pressure, collisional relaxation is not the limiting factor determining the value of τ but instead it is the spread of velocities that the probe interacts with. Figure 4.9 also shows a clear difference in the values of τ for the e and f Λ-doublet components (for a given pressure) with the RP signals for the e-component dephasing faster than those of the f-component. The reason for this behaviour is that the three most intense hyperfine components of the transition probing the e Λ-doublet are split by a greater amount (0.27 and 0.63 MHz) than the hyperfine components related to the f-component (0.21 MHz), giving faster damping of the signal. As expected both transitions exhibit the same decay constant in the high pressure limit. Taking the reciprocal of the time constant gives a rate $\gamma = \frac{1}{2\pi\tau}$, for the coherence relaxation in the system. The gradient of lines fit to a plot of γ against the sample pressure, as shown in figure 4.10 give rate constants of 2.9 ± 0.2 MHz Torr^{-1} for the e component and 3.4 ± 0.3 MHz Torr^{-1} for the f component. Published

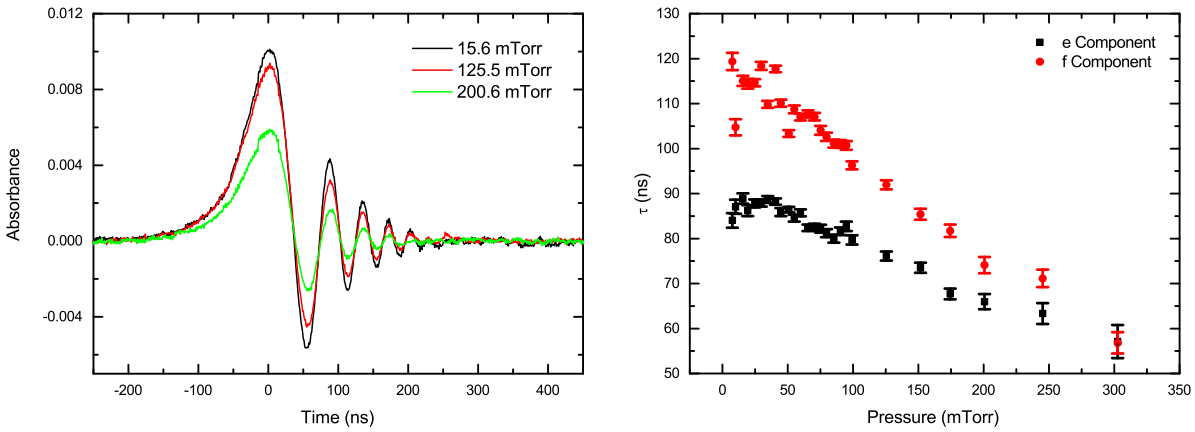

a) b)

Figure 4.9: a) A comparison of rapid passage signals measured at different gas sample pressures as shown. b) Decay constants obtained from the fitting of the rapid passage signals as a function of pressure of NO.

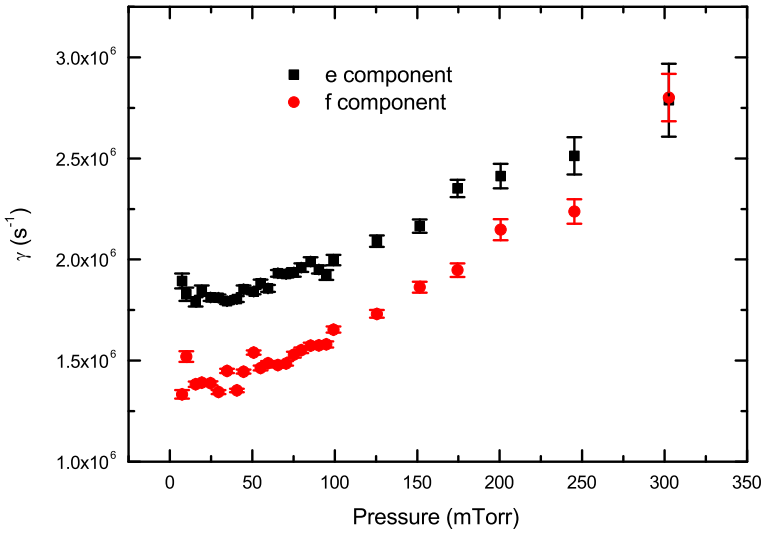

Figure 4.10: Decay rate $\gamma = \frac{1}{2\pi\tau}$, obtained from the fitting of the rapid passage signals as a function of pressure of NO. The gradients of lines fit to these data give rate constants of 2.9 ± 0.2 MHz Torr^{-1} for the e component and 3.4 ± 0.3 MHz Torr^{-1} for the f component.

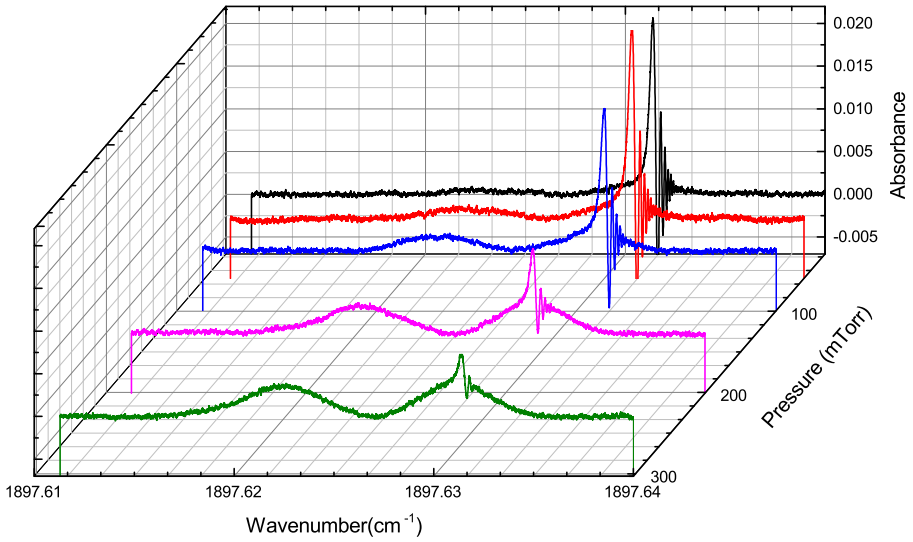

Figure 4.11: Absorption profiles of the R(15.5)$_{\frac{1}{2}}$ $v = 2 \leftarrow 1$ hot band transition of NO at different pressures.

measurements of the transverse (polarisation) relaxation rate by free induction decay using microwave coherent spectroscopy in OCS gave values of 5.25 ± 0.5 MHz Torr^{-1} [128] for the $J = 2 \leftarrow 1$ transition in the ground vibrational state and $5 - 6$ MHz Torr^{-1} across various rotational and vibrational states [129]. Measurements of linewidth self broadening in OCS gave similar values of 5.7 ± 0.2 MHz Torr^{-1} for the $J = 3 \leftarrow 2$ transition [130] and 6.03 ± 0.05 MHz Torr^{-1} for the $J = 2 \leftarrow 1$ transition [131]. The population transfer during these published experiments is small and so the decay of the signals is a measure of the transverse relaxation of the system in the absence of longitudinal (population) relaxation. Our measurements show good agreement with published data on similar systems, we note however, that the rate constants calculated here are affected by both the hyperfine structure of the transitions and the laser chirp rate (as shown in figure 4.6) meaning that our experiments do not provide a pure measurement of the transverse relaxation rate.

At all of the pressures studied, the Doppler absorption profile of the R(15.5)$_{\frac{1}{2}}$ $v = 2 \leftarrow 1$ hot band is significantly more intense than that expected from a thermal distribution. Figure 4.11 shows evidence that population is transferred from the initial velocity selected Λ-doublet level into both a range of velocity groups within the

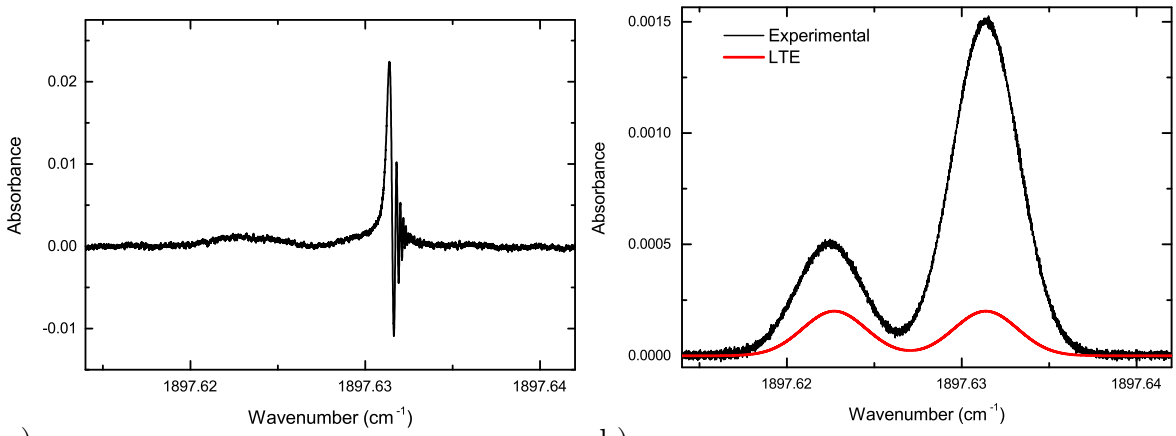

Figure 4.12: a) The R(15.5)$_{\frac{1}{2}}$ hot band absorption signal for a 59.6 mTorr sample of NO. b) Doppler profile of the data presented in a), with the RP signal removed. Also shown in b) is the calculated absorption profile for the same pressure of NO under local thermal equilibrium (LTE) conditions.

same level and into the near-degenerate opposite Λ-doublet level through collisions. If the pump laser is blocked, this background absorption profile disappears. Figure 4.12 shows the Λ-doublet profile of the hot band transition at 59.6 mTorr of NO in a) and the same in b) with the RP signal removed. For comparison, the profile calculated using HITRAN data for local thermal equilibrium conditions at the same pressure is also shown. As the pressure is increased the populations of the two Λ-doublet components become more equal (see figure 4.11), showing the effect of increased velocity redistribution and inelastic energy transfer. For comparison, in order to observe a maximum absorption of the same magnitude observed at 200 mTorr ($\sim 3 \times 10^{-3}$) without the pump beam, calculation, using absorption cross-section data from the HITRAN database, indicates that the cell would need to be filled with 900 mTorr of NO [119].

4.2 Linewidth Broadening with an External Noise Source

To further confirm the hypothesis that the laser linewidth influences the dephasing time of the rapid passage signals through velocity selecting the pumped sample a noise source was added to the DFB-QCL. The noise generator (RFDesign Noise Brick 3) produced white noise in the range 50 kHz to 500 MHz and was amplified once (Mini Circuits ZKL-1R5 amplifier) then passed into a bias tee.

The DFB-QCL was tuned to the e component of the $\mathrm{R}(6.5)_{\frac{1}{2}}$ $v = 1 \leftarrow 0$ Λ-doublet resolved transition and operated at a fixed frequency while the EC-QCL was tuned across the $\mathrm{P}(7.5)_{\frac{1}{2}}$ $v = 2 \leftarrow 1$ transition either at a slow rate of $0.34\,\mathrm{kHz\,ns^{-1}}$ using a function generator (TTi TG1304) output applied to the PZT or at a faster rate of $24.6\,\mathrm{kHz\,ns^{-1}}$ using the function generator output applied to the internal bias tee of the EC-QCL. The beams counter propagated through a 70 cm long cell in the same configuration as in figure 4.1 with a gas pressure of 43.5 mTorr. The detectors used were again a Vigo PVI-2TE-6 for the pump beam and a Vigo PVMI-3TE-10.6 for the probe. Approximately 100 scans were taken both with and without the noise generator attached to the DFB-QCL and averaged in the same manner as previously described.

Figure 4.13 shows the level of linewidth broadening caused by applying the noise source to the DFB-QCL and determined under conditions of slow scan rate. The noise source was amplified by approximately 27 dB and by 30 dB to produce the broadened lines (red and green) shown in figure 4.13. The signals were fit using Gaussians to give full widths at half maxima of the resonance features of 6.00 ± 0.01 MHz (no RF applied), 20.01 ± 0.02 MHz (RF amplified by 27 dB) and 26.96 ± 0.03 MHz (RF amplified by 30 dB). For the faster scan rate, shown in figure 4.14, this near five-fold broadening of the linewidth has clear consequences for the rapid passage. Without noise applied to the laser the signal appears as expected, *ie.* a normal rapid passage signal. However with the broader laser linewidth the rapid passage is

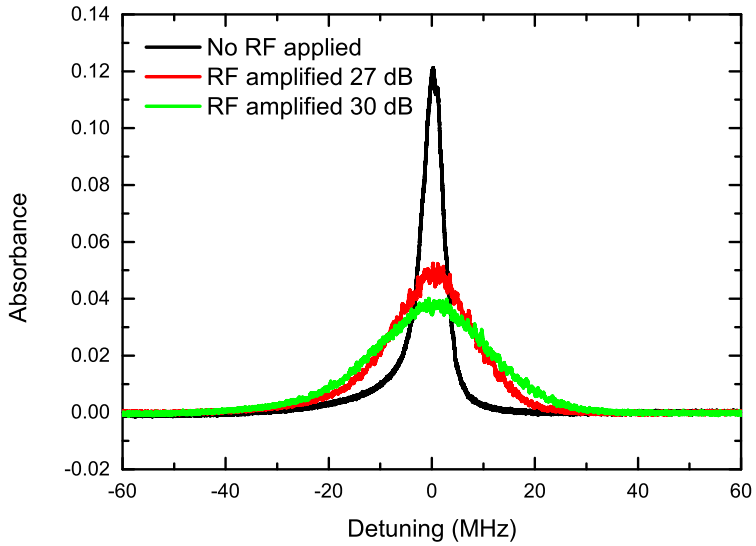

Figure 4.13: The effect of applying white RF noise to the pump DFB-QCL is shown. The black line shows the signal when no noise is applied with the red and green lines showing the signal when increasing amounts of amplified RF noise is applied to the pump laser. Fitting the signals with Gaussians yields linewidths (FWHM) of 6.00 ± 0.01 MHz, 20.01 ± 0.02 MHz and 26.96 ± 0.03 MHz respectively.

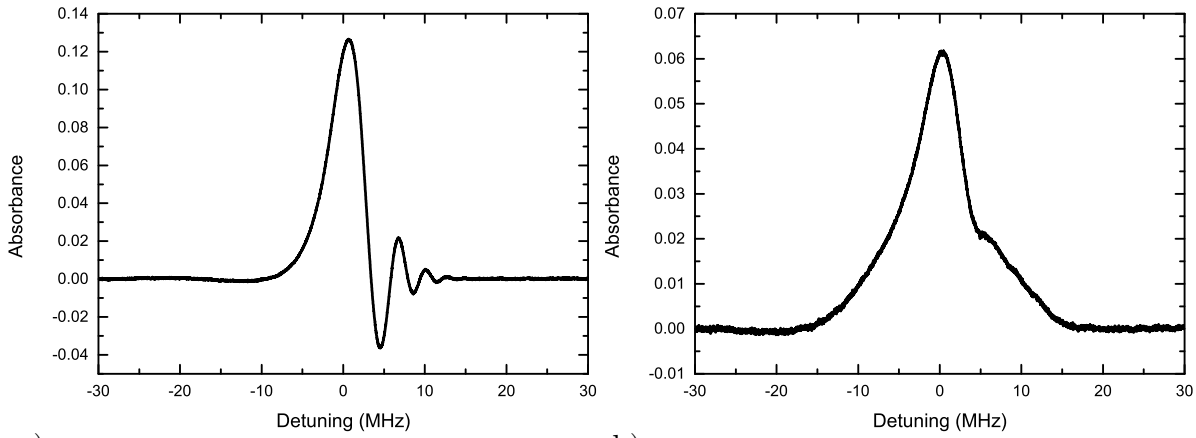

a) b)

Figure 4.14: The effect on the rapid passage shown in a) of the increased linewidth caused by applying noise to the pump laser is shown in b). The increased width of the pumped velocity group causes the oscillations to be completely damped out.

dephased far more quickly due to the larger velocity spread and is consequently no longer seen, confirming our conclusions about the importance of velocity dephasing in transient spectroscopy.

4.3 Two-Colour Polarisation Spectroscopy

In chapter 2 polarisation spectroscopy (PS) was described as a Doppler-free technique similar to Lamb-dip saturation spectroscopy. While PS has traditionally utilised strong electronic transitions originating from ground state atomic and molecular species, [132] Carr *et al.* [133] have recently extended PS to excited electronic states, observing Autler-Townes splitting in excited states of a low pressure sample of atomic cesium and Kulatunga *et al.* [134] achieved the same with rubidium vapour. The reduction in the Doppler background led to experiments of the type described in the preceding section being performed as polarisation spectroscopy experiments. Moreover by using an analysis polariser set at 45° and two detectors detecting the transmitted and reflected parts of the beam after this polariser allows both the absorption and the Doppler-free dispersion to be measured [135].

The signal expected for a beam transmitted through the analysis polariser I_{tr} was given in chapter 2 by equation (2.26) and is restated here

$$I_{tr} = 2I_0 e^{-\bar{\alpha}L} \left|\sin\theta\cos\phi + \cos\theta\sin\phi\right|^2 . \tag{4.2}$$

The reflected part of the signal I_{ref}, is then given by

$$I_{ref} = 2I_0 e^{-\bar{\alpha}L} \left|\cos\theta\cos\phi - \sin\theta\sin\phi\right|^2 . \tag{4.3}$$

The sum of the two signals is trivial being given by equation (2.1) whereas the difference signal is given by

$$\Delta I = I_0 e^{-\bar{\alpha}L} \left(\xi + \left|\sin\left(\theta+\phi\right)\right|^2 - \left|\cos\left(\theta+\phi\right)\right|^2\right), \tag{4.4}$$

where θ is the uncrossing angle, ϕ was given in chapter 2 by equation (2.27) and ξ accounts for the non-ideal behaviour of the analysis polarizer. At an uncrossing angle of 45° the differential signal yields a purely dispersive signal as the amount of the saturated absorption lineshape seen by each detector is equal and so cancels. The only remaining contributions to the signal come from those parts of the electric field that have been rotated by the polarised pumped gas.

By applying polarisation spectroscopy to the pump-probe setup described in this chapter, it cannot properly be said to be removing the Doppler broadened component since the experiment seeks to pump a sub-Doppler velocity group into the excited state and probe this. However as demonstrated in the previous section population is transferred into nearby velocity groups so the technique maintains this usefulness with the added benefit of slightly increasing the signal to noise ratio. As will be shown in section 4.3.2 at slow probe laser chirp rates the summed signal gave a measurement of the pure absorption signal which showed the velocity selection induced by the pump beam whereas the difference signal gave a classic dispersion lineshape. Increasing the chirp rate again led to the observation of rapid passage which was seen in both the absorption and dispersion signals.

4.3.1 Experimental

The experiment utilises the same two cw QCLs operating at 5 µm in the same counter-propagating configuration in a 70 cm long glass cell filled with a low pressure sample of NO (10 - 100 mTorr). In this case the EC-QCL was used as the pump field, and the DFB-QCL was used as the probe. The pump laser was circularly polarized using a $\frac{\lambda}{4}$ waveplate (Alphalas) and its frequency tuned to a fixed frequency within the $R(14.5)_{\frac{1}{2}}$ $v = 1 \leftarrow 0$ transition. This time the pump laser was not scanned as the experimental time was shorter than the length of time it took the laser to drift from the transition frequency. The 2 MHz laser linewidth resulted in velocity selective excitation into the $v = 1$ state, which was subsequently probed by the linearly-polarised probe laser. The probe laser frequency was continuously scanned

across the $R(15.5)_{\frac{1}{2}}$ $v = 2 \leftarrow 1$ transition at a selection of scan rates using the output from a TTi function generator (TG1304) to supply a triangular waveform to the laser driver. Within a single linear current sweep, the total frequency scan for this laser was between 3 and 5 GHz, producing chirp rates ranging from $0.1\,\mathrm{kHz\,ns^{-1}}$ to $248\,\mathrm{kHz\,ns^{-1}}$. After exiting the cell the probe beam passed through an analysis polarizer (Alphalas Rochon polariser) set with its transmission axis at 45° to that of the probe laser and both the transmitted and reflected beams were then focussed by off-axis parabolic mirrors onto two thermoelectrically cooled mercury cadmium telluride detectors (both VIGO PVMI-3TE-10.6). Similar detectors were used, such that the measured signal intensities of the reflected and transmitted beams were well-matched. The PS signals were collected and recorded by a 2.5 gigasample/s, 400 MHz bandwidth digital oscilloscope (LeCroy Wavesurfer 44MXs-A). The signal to noise is further improved by averaging over 50 scans in the same manner as previously described in this chapter.

The key quantity in equation (4.4) is the complex phase factor ϕ which accounts for both the circular dichroism, $\Delta\alpha$, and the optical birefringence, Δn, of the velocity selected sample which is induced by the circularly polarized pump laser, and is defined generally as

$$\phi(\omega) = \frac{\omega}{2c}\left(L\Delta n(\omega) + \Delta b_r\right) + i\left(L\frac{\Delta\alpha}{4} + \frac{\Delta b_i}{2}\right), \tag{4.5}$$

where L is the path length of the light in the sample, ω is the frequency of the probe and Δb_r and Δb_i account for possible contributions to birefringence and the dichroism coming from the cell windows, respectively. The parameters $\Delta\alpha$ and Δn are related to the probe laser detuning $(\omega - \omega_0)$, and the dephasing rate γ, through equations (4.6) and (4.7) respectively [88, 133]

$$\Delta\alpha = \frac{\Delta\alpha_0\gamma^2}{\gamma^2 + (\omega - \omega_0)^2}, \tag{4.6}$$

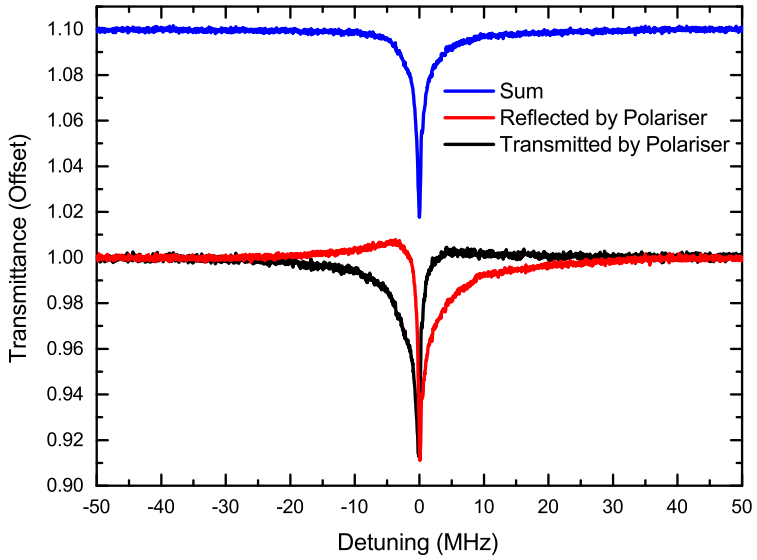

Figure 4.15: Polarization signals obtained at a pressure of 36 mTorr and probe chirp rate of $0.92\,\mathrm{kHz\,ns^{-1}}$. The pure absorption signal is shown offset and shows the velocity selection induced by the pump beam. The full width at half maximum of the summed signal is 1.5±0.2 MHz.

$$\Delta n = \Delta\alpha_0 \frac{c}{\omega_0} \frac{\gamma^2 (\omega - \omega_0)}{\gamma^2 + (\omega - \omega_0)}. \tag{4.7}$$

Substituting these into equation (4.5) yields equation (2.27).

4.3.2 Results

Figure 4.15 shows both the transmitted and reflected parts of the beam after the analysis polariser with a gas pressure of 36 mTorr and a probe chirp rate of $0.92\,\mathrm{kHz\,ns^{-1}}$. Also shown is the sum of these two parts, giving the total absorption and demonstrating the velocity selective pumping with a full width at half maximum of 1.5±0.2 MHz.

The difference signal for the transmitted and reflected signals shown in figure 4.15 is shown in figure 4.16. The data shows clear resolution of the expected dispersion line shape. Also shown is a fit to the data using equation (4.4) and a method of least squares minimisation. The fit shown in figure 4.16 yields a linewidth of 1.7 ± 0.3 MHz. It should be noted that while this simple line shape function fits the overall profile reasonably well under these conditions of slow probe scan rate, the

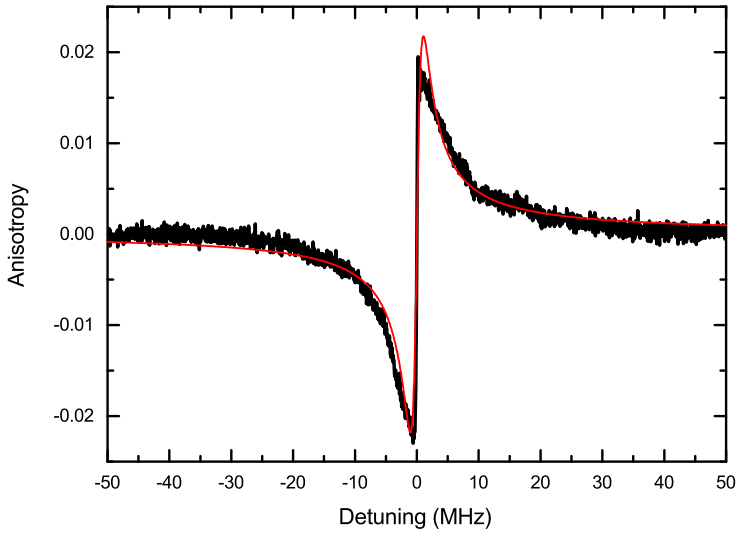

Figure 4.16: The difference signal derived from the transmitted and reflected signals shown in figure 4.15. The expected dispersion line shape is well resolved and a fit to it using equation (4.4) is also shown, yielding a linewidth of 1.7 ± 0.3 MHz.

data around the central resonance consistently displays a slightly steeper gradient than that predicted by the fit. This effect may be due to the lasers being in perfect 2-photon resonance at line centre but it seems that any strong coherence effect is dampened by the inherent jitter in the unstabilised laser fields under the slow scanning conditions. As will be shown below, the effect of two-photon coherence is more readily apparent in the data obtained when the probe laser chirp rate is increased as was the case in the data presented earlier in this chapter.

Figure 4.17 shows the evolution of the PS signals as the chirp rate of the probe laser is increased to *ca.* $15\,\mathrm{kHz\,ns^{-1}}$. It is clear that both the absorptive and dispersive PS signals develop oscillatory structure as the chirp rate of the probe laser increases. This structure is again due to rapid passage in which the probe laser is tuned through resonance on a time scale which is short compared to the relaxation time of the system as demonstrated previously in this chapter. A fit to the RP signal shown in figure 4.17c) is shown in figure 4.18 and yields a decay period of ~ 200 ns. This is consistent with the chirp rate of $15.2\,\mathrm{kHz\,ns^{-1}}$ which is slower than any of the data points reported in section 4.1.3 and follows the upward trend of decay

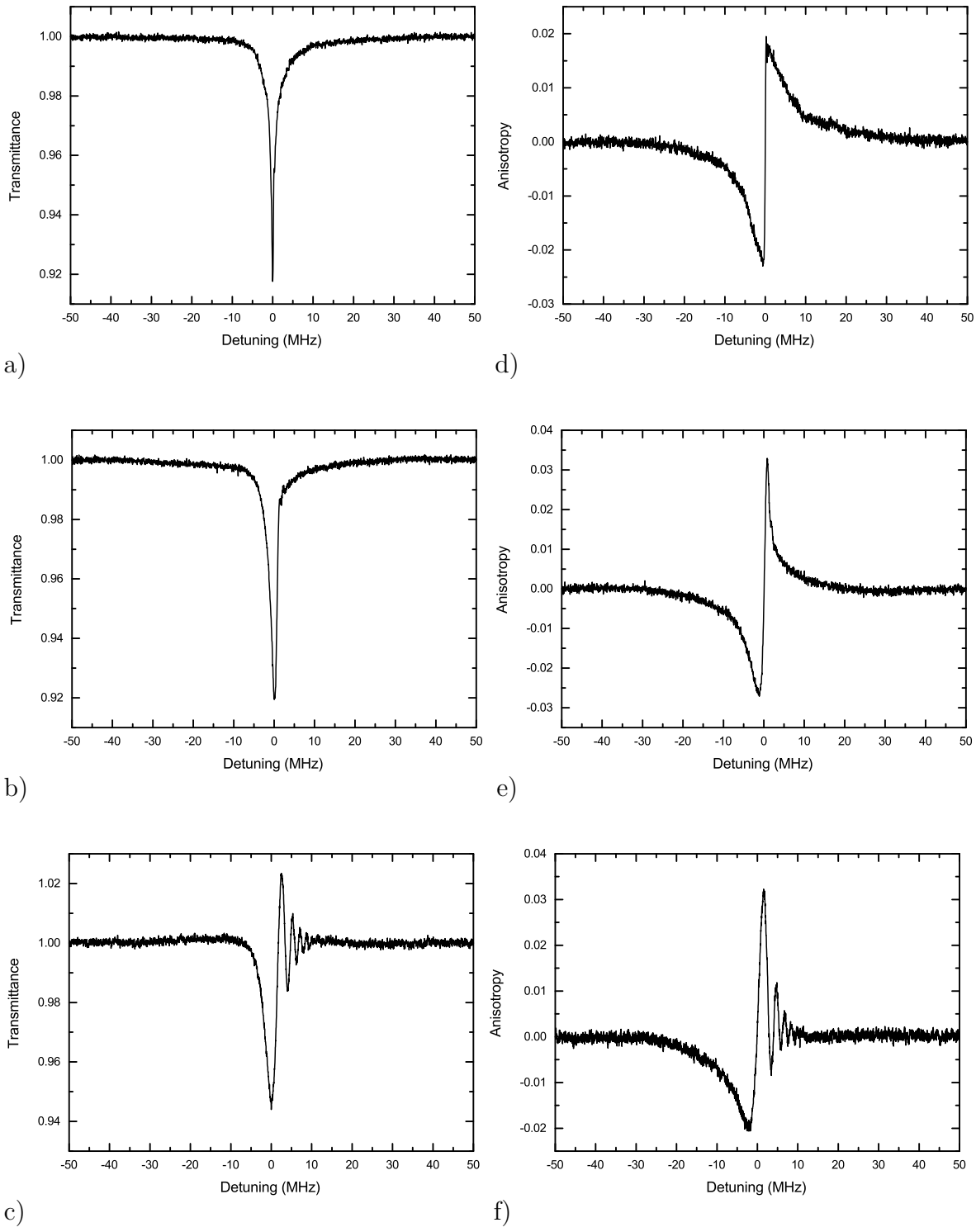

Figure 4.17: Polarisation signals (both absorption and dispersion) as a function of probe laser chirp rate obtained at a pressure of 36 mTorr. The chirp rates increasing from top to bottom are 0.92, 4.1 and 15.2 $\mathrm{kHz\,ns^{-1}}$. a) to c) show the absorption while d) to f) show the dispersion. As the chirp rate increases rapid passage effects become apparent in both the absorption and the dispersion with a phase difference of $\frac{\pi}{2}$ between the two.

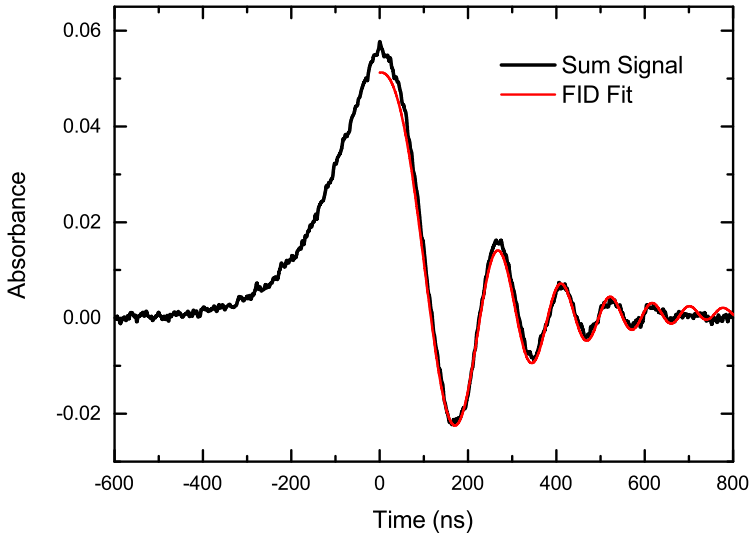

Figure 4.18: A fit to the RP signal shown in figure 4.17c) using equation (4.1) yields a decay period of ~ 200 ns.

period with decreasing chirp rate. As expected from the optical Bloch equations, the absorption signal and dispersion signal are out of phase by $\frac{\pi}{2}$.

Polarisation spectroscopy has been used as a modulation free laser stabilisation technique since it gives an error-type signal (*ie.* the signal has opposite sign depending upon whether the laser frequency is above or below the target frequency) as the laser moves away from resonance. In this two laser technique it is therefore possible that the dispersion signal derived from the probe laser signal at slow chirp rates (which correspond to slow drifts of the laser frequency) could allow two lasers to be locked in two-photon resonance. The pump laser would be free to drift but assuming those drifts are slow then the detuning of the two-photon resonance caused by this drift would cause an error signal in the probe laser which could be fed back to lock the probe into two photon resonance with the pump.

4.4 Simulations using the 3-Level Density Matrix

In the previous chapter a rapid passage signal was simulated by solving the two-level optical Bloch equations as shown in figure 3.22. With the extension of the system

to include a high power narrow bandwidth probe laser tuned to a ladder state transition, it is pertinent to consider the optical response of the system in terms of three coupled levels. The density matrix for a three level system coupled by two photons was given in chapter 2; specifically the equations of motion were given by equations (2.66). Throughout these pump-probe experiments it has been assumed that over the time period of the rapid passage signals the pump laser frequency has remained static or quasi static while the probe laser is scanned. Therefore in equations (2.66) the Stokes detuning Δ_{12} and the two-photon detuning Δ_{02} are time varying quantities with their rates of change equal to the chirp rate of the laser. A MATLAB program was created to solve numerically these equations of motion for a three level system, giving the populations and coherences at each time point over which the integration is performed.

The 3-level model takes as inputs the measured properties of the system (laser powers, P, probe laser chirp rate, gas pressure, laser linewidths, Δ_{pump} and Δ_{probe}, beam radii, r), along with broadening parameters (Γ_{01} and Γ_{12} respectively for the pump and probe transitions) and the Einstein A coefficients which are used to calculate the transition dipole moments, μ (taken from the HITRAN database [119]). The Rabi frequencies, Ω, are calculated from these inputs, as are the decay constants for the two transitions,γ_{01} and γ_{12}, and for the 2-photon combination, γ_{02}. These latter four quantities are given by

$$\Omega = \frac{\mu\sqrt{4P}}{\pi r^2 c\epsilon_0 \hbar}, \tag{4.8}$$

$$\gamma_{01} = \sqrt{\Delta_{pump}^2 + \Gamma_{01}^2}, \tag{4.9}$$

$$\gamma_{12} = \sqrt{\Delta_{probe}^2 + \Gamma_{12}^2}, \tag{4.10}$$

$$\gamma_{02} = \sqrt{\Delta_{pump}^2 + \Delta_{probe}^2}. \tag{4.11}$$

The system of ordinary differential equations (2.66) describing the components of the density matrix is set up in a MATLAB program and solved using one of MAT-

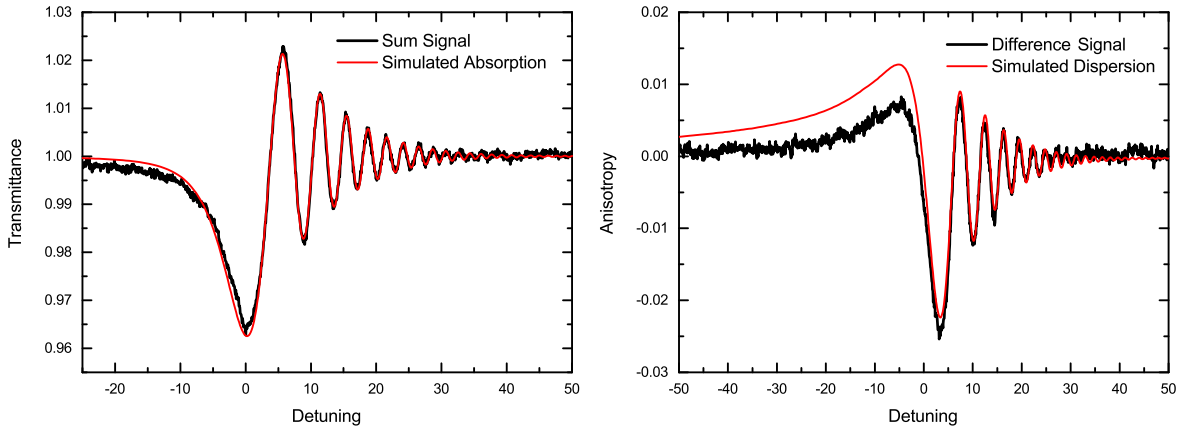

a) b)

Figure 4.19: The absorption a), and dispersion b), signals from a PS experiment at a pressure of 36 mTorr. The EC-QCL pumps the R(14.4)$_{\frac{1}{2}}$ fundamental and the DFB-QCL probes the R(15.4)$_{\frac{1}{2}}$ hot band transition. The three-level simulations (red lines) are shown to accurately model the behaviour of both parts of the signal.

LAB's proprietary ODE solvers, ode23. The diagonal elements of the 3x3 density matrix describing the system are the populations of each of the three levels while the off-diagonal matrix elements are the coherence terms. The term of interest for the pump-probe experiments demonstrated in this chapter is the complex coherence term between the first and second excited ro-vibrational levels. The imaginary part of this term gives the absorption and the real part gives the dispersion.

Figure 4.19 shows the pure absorption and dispersion signals produced in the PS experiment with the lasers tuned as described in the PS section, at a pressure of 36 mTorr along with the corresponding parts of the ρ_{12} coherence term from the 3-level simulation. The input powers for the simulation were 60 mW for the pump and 100 mW for the probe with laser linewidths of 2 MHz and 0.5 MHz (consistent with a narrowing of the linewidth over a short measurement time scale) respectively. The chirp rate used for the simulation was $72\,\mathrm{kHz\,ns^{-1}}$ which is consistent with the chirp rate measured using a germanium etalon of $69\,\mathrm{kHz\,ns^{-1}}$. There is excellent agreement between the three-level simulation and the experimental data. The decay of the rapid passage oscillations is faster in the three-level model in comparison with a two-level model as one would expect with an extra decay channel. This is shown

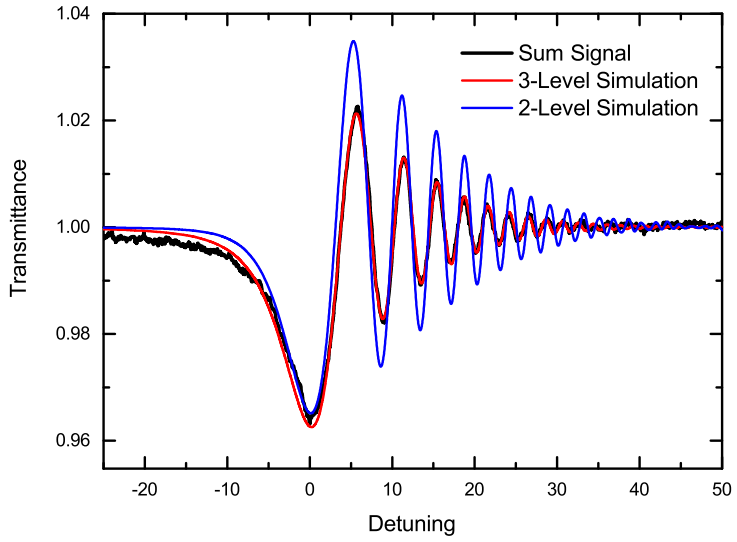

Figure 4.20: A comparison of the two-level model with the three-level model under the same conditions as 4.19. The oscillations are accurately modelled by both simulations but the decay period is far longer in the two-level model than in the three-level one, with the three-level model being the more accurate.

by running the two-level model with a Doppler width equal to the pump beam width and using the same conditions for the probe beam as in the three-level model. Figure 4.20 demonstrates how the extra decay channel in the three-level model leads to a faster dephasing time and a better fit to the experimental data. The oscillation frequency is well matched by both simulations however showing that this is primarily determined by the chirp rate of the probe laser under these conditions.

For completeness figure 4.21 shows the evolution of the populations of the three ro-vibrational states as the probe laser is scanned. The model starts by assuming that all the population is in the ground state, but by the time the probe beam has scanned far enough to begin to come into two-photon resonance the populations in the ground and first excited state have become equal at the incoherent limit of 50%. The model predicts 38% population transfer into the second vibrationally excited state. This section has shown that the field oscillations seen in pump-probe spectroscopy on velocity selected samples are accurately modelled by solving the density matrix for a three level system and further highlights the use of QCLs for non-linear spectroscopy and coherent state preparation.

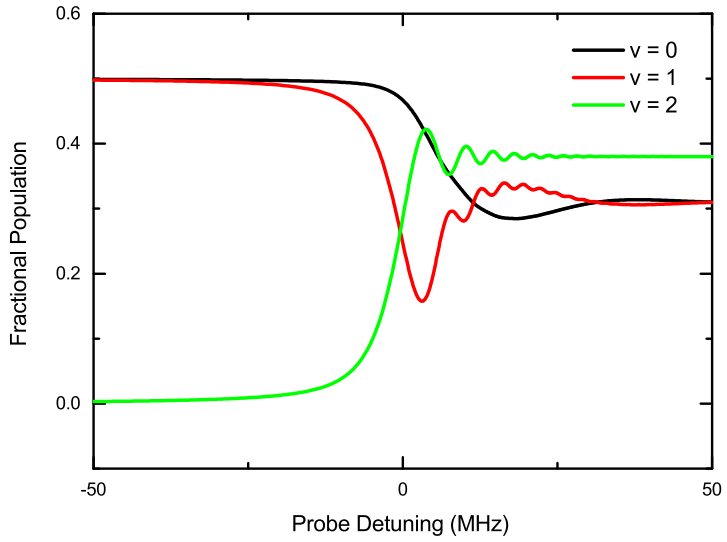

Figure 4.21: Showing the evolution of the populations in the three vibrational levels as the probe laser tunes through resonance. The model predicts 38% population transfer into the $v = 2$ level.

4.5 Conclusions

This chapter has detailed the results from pump-probe experiments conducted on low pressure samples of NO utilizing two high power cw quantum cascade lasers. The lasers were tuned to the individual rotationally resolved transitions within the $v = 1 \leftarrow 0$ (pump) and $v = 2 \leftarrow 1$ (probe) vibrational bands and there is clear evidence of velocity selective pumping. The reduced velocity spread in the excited $v = 1, J$ states compared to the Doppler width, allowed clear rapid passage structures to be observed in the hot band transient absorption spectra. The effects of altering chirp rate and gas pressure in the transient signals were investigated. It was found that the RP signals decay faster in time as both the chirp rate of the probe laser and the pressure of NO was increased. This indicates that both velocity dephasing and collisional processes are important contributors to the form of the RP signals. Evidence of velocity redistribution was readily seen (and population transfer into the near-degenerate opposite Λ-doublet component through collisions in the gas) with the amount of absorption in both the pumped and unpumped components measured to be markedly greater than that expected under local thermal equilibrium. This

indicates a high degree of population transfer caused by the strong pumping.

The hyperfine structure of the NO molecule was shown to have a large impact on the structure of the rapid passage when the lasers were tuned to the $\Omega = \frac{3}{2}$ transitions in which the energy differences between pairs of hyperfine levels is greater than in the $\Omega = \frac{1}{2}$ transitions. This increased spacing caused rapid passage signals originating from each hyperfine transition to interfere causing unusual line shapes. As the chirp rate increased the rapid passage signals attained the shape that is expected for a single transition as the size of the velocity group the probe laser interacted with per unit time increased to include all the hyperfine transitions.

A radio frequency noise source was applied to the DFB-QCL which was then used as the pump laser to demonstrate the effect of broadening the laser linewidth. The applied noise was shown to broaden the size of the pumped velocity group by almost 5 times - indicative of the same increase in the laser linewidth. When the probe laser chirp rate was increased it was seen that the larger velocity group being pumped led to far more rapid dephasing to the extent that no rapid passage was seen, further confirming the importance of velocity dephasing for transient spectroscopy.

A polarisation spectroscopy experiment was also demonstrated using the same ladder state transitions. The pump beam was circularly polarised and the rotation of the probe beam by the polarised vibrationally excited sub-Doppler velocity group was monitored through the use of an analysis polariser whose transmission axis was set at 45° to the polarisation direction of the probe laser beam. Two detectors were employed to monitor the transmitted and reflected parts of the beam after the analysis polariser, allowing both the absorptive and dispersive parts of the signal to be recorded. At low laser scan rates this technique has applications in modulation-free laser stabilisation and may allow two lasers to be locked to two-photon resonance. At faster probe chirp rates rapid passage effects again became evident and have been observed in the purely dispersive component of the signal for the first time. The absorptive and dispersive components were seen to be $\frac{\pi}{2}$ out of phase as expected.

Finally a model was developed that solves the three-level density matrix with

two photons coupling the levels. The model was shown to be in good agreement with experimental data and gave both the absorptive and dispersive components of the complex coherence for the probe beam. The model also gives the expected population transfer which for the experimental conditions given was 38%. These initial pump and probe studies highlight the the potential utility of the set-up when combined with multi-pass cells, for detailed studies of both inelastic and elastic collisional processes and velocity changing effects, especially given the wide spectral tunability afforded by external cavity QCLs.

Chapter 5

Mid-IR Pulse Generation for Coherent Population Transfer

The data presented in chapter 4 quantified the temporal decay of the coherent rapid passage signals observed from a velocity selected sample probed with a rapidly swept probe field and prepared under conditions of constant pump intensity. The focus now turns to the temporal decay of the coherent transient signal once the pump has been switched off. To this end an acousto-optic modulator (AOM) was incorporated into the experimental setup. The AOM was used as a fast switch to give a well defined time period over which the fundamental ro-vibrational transition was pumped in a pump-probe experiment similar to those described in chapter 4. The ability of an AOM to create a pulse from a cw laser opens up the possibility to perform the coherent population transfer technique known as STIRAP which was described in chapter 2. In the second part of this chapter the properties of the two lasers used previously in this thesis, along with the measured and literature values for the properties of the transitions involved, are used to simulate the use of STIRAP to achieve a high level of population transfer between ro-vibrational levels in NO. A necessary condition for STIRAP to be successful is that the lasers must be in two-photon resonance with the three-level system. It is therefore necessary to stabilise the lasers in order that this condition be met and the final part of this chapter

details two attempted methods for stabilising output frequency of the EC-QCL.

5.1 Amplitude Modulation in a Pump-Probe Experiment

5.1.1 Characterisation of a Mid-IR Acousto-Optic Modulator

The AOM (Isomet AOM (1208-6-4M)) contains a piece of germanium as the optical medium and is anti-reflection coated at 5.3 µm. Attached to one side of the germanium crystal is a piezoelectric transducer (PZT) which produces sound waves that propagate through the germanium and are absorbed on the other side. The sound waves create moving planes of expansion and compression, causing the refractive index of the germanium to change periodically. [136] The incident laser beam is scattered by these planes in a manner analogous to Bragg diffraction in crystals as shown schematically in figure 5.1. Since the diffraction occurs from moving sound waves rather than static crystal lattice planes, the frequency of the scattered light is Doppler shifted by the frequency of the applied sound wave. The normal to the AOM crystal surface is tilted at the Bragg angle θ to the propagation direction of the incident laser beam such that the diffracted beam emerges with a separation angle between the diffracted (first order) and unaffected (zeroth order) parts of the beam of 2θ. The required Bragg angle is a function of the wavelength of the incident light, λ, the frequency of the sound waves, f and the acoustic velocity of the medium, V

$$\theta = \frac{\lambda f}{2V}. \tag{5.1}$$

The intensity of the diffracted light is dependant on the intensity of the applied sound waves with the peak intensity being reached at the saturation power P_{sat}

$$P_{sat} = \frac{k\lambda^2 H}{2LM_2}, \tag{5.2}$$

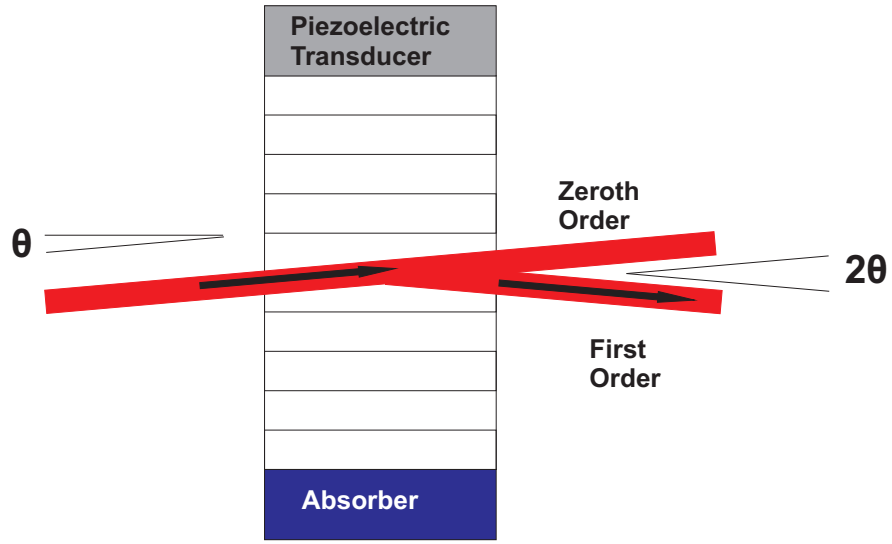

Figure 5.1: A schematic of an AOM. The piezoelectric transducer produces a sound wave which propagates through the optical crystal and produces planes of varying refractive index from which the laser wavefront is diffracted.

where k is the transducer conversion loss (typically near unity [137]), L is the interaction length, H is the electrode height and M_2 is known as the figure of merit (approximately 170 for Ge [138]). The diffraction efficiency decreases as the acoustic power is increased beyond P_{sat} and typically this power is tuned by adjusting a potentiometer on the driver to set the maximum drive power. The power can then be switched digitally from zero to full power or may be controlled by analogue modulation to change the intensity of the first order beam. Power attenuation by this method does not change the laser linewidth or polarisation and therefore offers a distinct advantage over power tuning by injection current modulation or use of a polariser.

The switching speed of the AOM is limited by the transit time of the sound wave across the beam waist within the germanium crystal with the rise time t_r, of the first order being given by

$$t_r = 0.65\frac{d}{V}, \tag{5.3}$$

where d is the beam diameter (measured at the width at which the beam intensity falls to $\frac{1}{e^2}$ of its peak intensity) and V is the acoustic velocity. Evidently then the switching speed may be increased by focussing the beam into the AOM; even faster

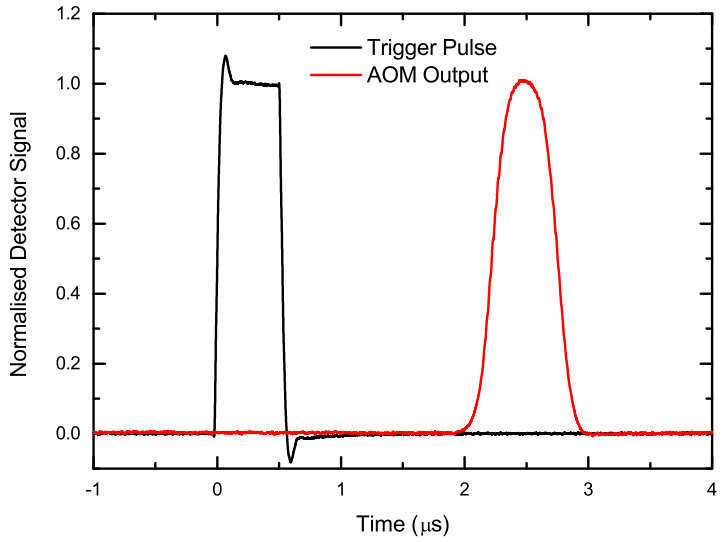

Figure 5.2: AOM output pulse produced by applying a 0.5 µs trigger pulse to the driver.

switching would require an elector-optic modulator which is not readily available in the mid-IR region.

The AOM was mounted on a rotation stage (Thorlabs PR01/M) and the angle tuned to give maximum diffraction efficiency, defined as the ratio of power diffracted into the first order to total incoming power. A digital function generator (TTi TG1304) provided a square wave voltage input to the radio-frequency driver (Isomet RFA151) which output a 50 MHz signal to the AOM PZT. The drive power was set to P_{sat} by observing the power in the first order beam and increasing the drive power until the output power began to decrease before rolling the drive power back to P_{sat}. The diffraction efficiency was measured to be 91% in good agreement with the manufacturer's stated efficiency.

The rise time of the AOM was measured using a 2 mm beam radius with the function generator supplying a 0.5 µs long trigger pulse. As shown in figure 5.2 the timescale over which the AOM transmission of the first-order beam rises from zero to full power was measured to be 506 ± 9 ns, in close agreement with the manufacturers' specification. The frequency offset between the zeroth and first-order beams should be 50 MHz and this was confirmed by the following experiment:

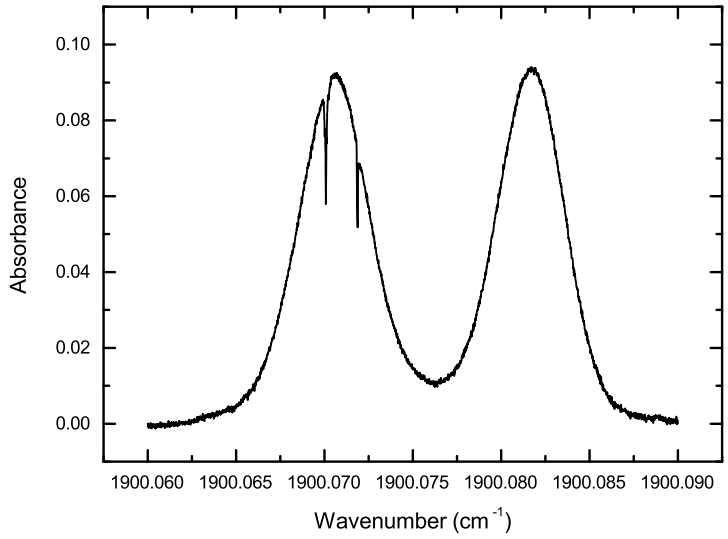

Figure 5.3: Two Bennett holes in the Doppler profile of the $R(6.5)_{\frac{1}{2}}$ $v = 1 \leftarrow 0$ transition of NO showing the 50 MHz frequency offset between the zeroth and first order beams transmitted through the AOM. The first order beam burns the hole at the higher frequency.

the EC-QCL output, resonant with the fundamental $R(6.5)_{\frac{1}{2}}$ transition, was directed into the AOM, and two Bennett holes were burnt into a low pressure NO sample using both the zeroth and first-orders of the modulated EC-QCL beam. The Bennett holes were observed by aligning both orders with the counter-propagating DFB probe which was scanned across the same $R(6.5)_{\frac{1}{2}}$ transition. A frequency scale was set using the known separation of the $R(6.5)_{\frac{1}{2}}$ Λ-doublet components so that the 50 MHz offset between the zeroth and first orders could be experimentally verified as 49.6 ± 0.9 MHz. The widths of the Bennett holes shown in figure 5.3 correspond to the pump laser linewidth of *ca.* 2 MHz, and demonstrate that the AOM does not change the linewidth of the modulated IR radiation.

5.1.2 Amplitude modulating the pump pulse - decay of the transient signal

With the experiment set up as shown in figure 5.4, the pump (DFB-QCL) laser frequency was fixed on resonance with the $R(6.5)_{\frac{1}{2}}$ $v = 1 \leftarrow 0$ transition while the

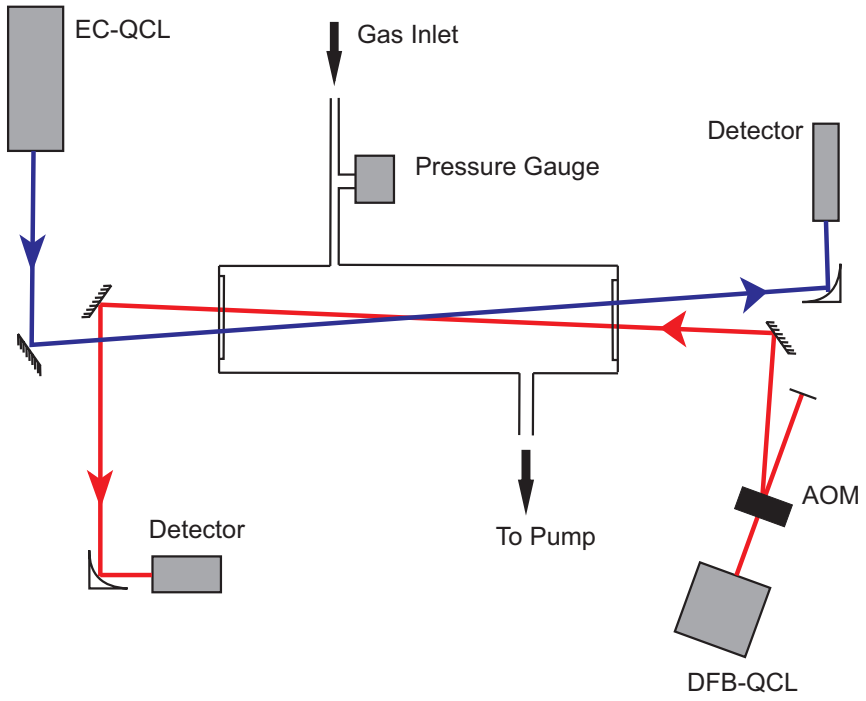

Figure 5.4: Experimental setup used for all amplitude modulation experiments. The setup is the same as for the pump probe experiments presented in chapter 4 with the exception that an AOM has been added to the DFB-QCL beam line to act as a fast switch.

probe (EC-QCL) laser was tuned to the ladder state $P(7.5)_{\frac{1}{2}}$ $v = 2 \leftarrow 1$ transition. The pump beam was aligned such that only the first order diffracted beam passed through the gas cell and was counter-propagated with respect to the probe beam. The pump beam was then turned on and off using the AOM. The frequency of the probe was scanned at a rate of $236\,\mathrm{kHz\,ns^{-1}}$ using a TTi function generator (1010A) applying a voltage ramp to the internal bias tee of the laser. The phase of the probe scan was altered in time thereby allowing the velocity selected sample to be probed at a variety of time delays after the AOM had been switched off as shown in figure 5.5. The time delay is defined as the period between the pump power falling to half its maximum and the time point corresponding to the maximum amplitude of the coherent transient signal. The data in figure 5.5 were obtained at a pressure of 50 mTorr and the signals shown for each time delay are an average of 100 scans.

The experiment was performed using several NO pressures and the maximum

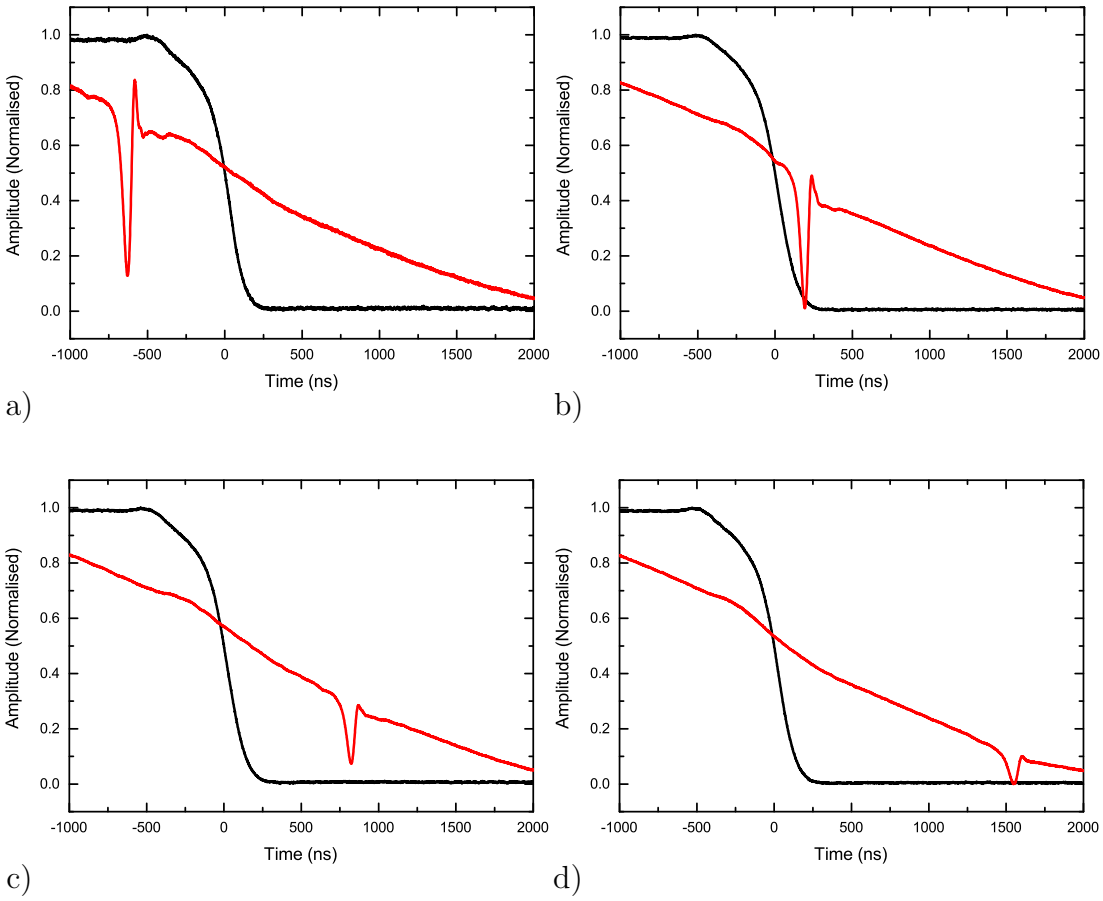

Figure 5.5: Showing the absorption in the hot band transition at several time delays after the pump beam has been switched off. a) 630 ns before the pump is turned off, b) 190 ns after the pump is turned off, c) 820 ns after the pump is turned off and d) 1550 ns after the pump is turned off. The time delay is defined as the period between the pump power falling to half its maximum and the time point corresponding to the maximum amplitude of the coherent transient signal. The switching off of the pump beam is shown in black with the corresponding probe scans being the red lines.

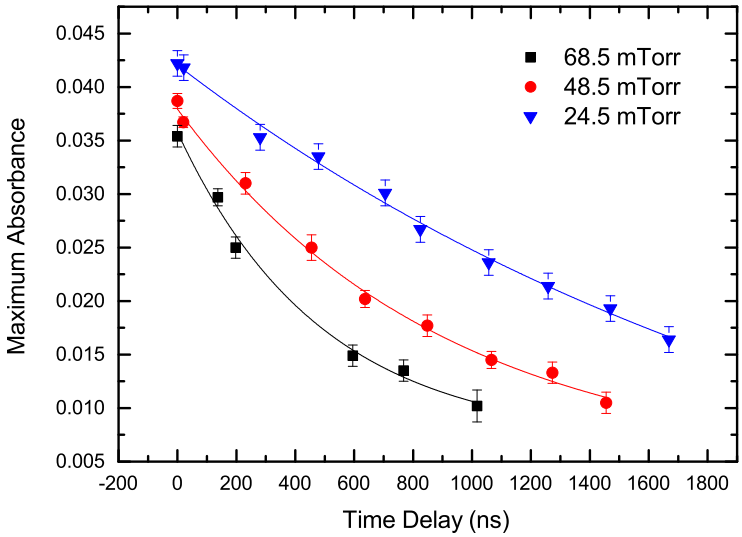

Figure 5.6: The maximum absorbance of the transient signal is plotted against the delay time between switching off the pump and sweeping through resonance. Exponential decays are fitted as shown to give decay periods τ of 2405 ± 645 ns (24.5 mTorr pressure), 895 ± 124 ns (48.5 mTorr) and 486 ± 120 ns (68.5 mTorr).

absorbance is plotted against time delay for several representative pressures in figure 5.6. The decay in the measured maximum absorbance with increasing time delay is fit using an exponential decay as shown to give time constants τ, which reflect the combined polarization and population relaxation of the system. At pressures of 24.5 mTorr and 34.5 mTorr the time constants were found to be 2405 ± 645 ns and 1583 ± 518 ns respectively. These compare well with values of 2458 ns and 1745 ns respectively calculated from the self broadening parameter given by HITRAN [119]. At higher pressures however, the measured time constants are a little lower than the values expected from HITRAN. For example at 48.5 mTorr the measured decay period is 895 ± 124 ns compared with a calculated 1242 ns using HITRAN and at 68.5 mTorr the decay period is 486 ± 120 ns compared with 879 ns, although since we likely measure a combination of the depolarisation and population decay times as the molecules potentially also undergo velocity redistribution this is perhaps unsurprising.

The width of the absorption features is seen to increase at increasing delay times indicating velocity redistribution. It should be noted that since the width of the

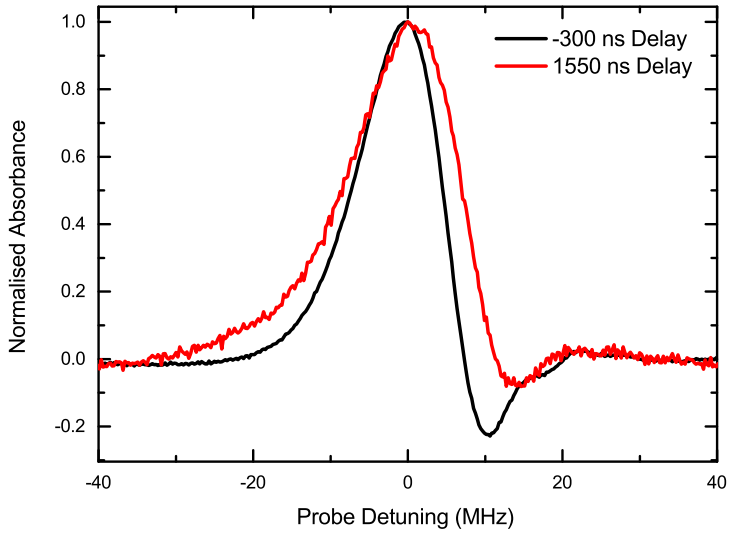

Figure 5.7: Coherent transient signals before and after the pump beam has been extinguished.

signal increases on the same time scale as the decrease in signal amplitude, that this effect is not easily seen in all of our data and as such we show only the clearest example. This is shown in figure 5.7 in which the widths of signals measured 300 ns before the pump is turned off and 1550 ns after the pump is switched off are compared. In figure 5.7 the absorbances have been normalised in order to emphasise the linewidth change. Figure 5.8 shows how both the maximum absorbance and the width of the signals changes with increasing delay time. The measured width is the full width at half maximum of the absorbance signals. The linewidth measured while the pump laser is on, is 11.5 MHz and represents the narrow sub-Doppler velocity group prepared by the pump laser which is then broadened by the effective linewidth of the fast-chirping probe laser. The resolution limit, $\Delta\nu$, of a fast chirping laser with a chirp rate k (Hz s^{-1}) is given by [74, 139].

$$\Delta\nu = \sqrt{Ck} \tag{5.4}$$

where C is a constant of order unity. At the measured chirp rate and with a pumped velocity group of 2 MHz width, the effective linewidth of the probe laser is calculated

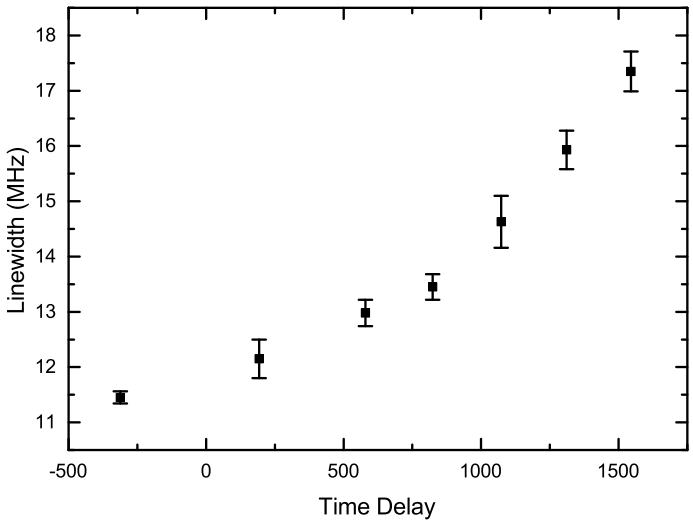

Figure 5.8: The evolution of the width of the coherent transient signals as a function of time after the pump pulse has been extinguished. The total observed linewidth is a quadrature sum of the velocity profile width and the effective laser linewidth.

to be 11.3 MHz; this is consistent with a value of C of 0.541 which falls between the values for Gaussian (0.441) and rectangular time windows (0.886). The observed linewidth of the transient signal is then interpreted as the quadrature sum of the true width of velocity profile in the $v = 1$ state and the effective laser linewidth. The data therefore indicate that the velocity profile in the $v = 1$ state broadens from 2 MHz (while the pump laser is on) to 13 MHz at a time delay of approximately 1.5 µs i.e. at a rate of $6.45\,\mathrm{MHz\,\mu s^{-1}}$.

These preliminary measurements indicate that similar studies within multi-pass cells are capable of providing details of speed dependent collisional processes. For example, the inherent velocity selection afforded by QCLs can be combined with two colour polarization spectroscopy to provide information about state-to-state differential scattering cross-sections for both elastic and inelastic collisions of vibrationally excited molecules in their ground electronic state, and to measure the degree of polarization retention during inelastic energy transfer [140, 141].

5.2 Simulating STIRAP by Solving the Three-Level Density Matrix

The initial foray into fast amplitude modulation of QCLs as presented in the previous section paves the way towards attempting to achieve Stimulated Raman Adiabatic Passage (STIRAP) in the NO system. The theory of this technique was presented in chapter 2 and involves the pump and Stokes laser beams being pulsed in a counter-intuitive order. To summarise, the technique involves the molecules being subject to partially overlapping (in time) pulses of laser radiation, the frequencies of which correspond to the fundamental (pump) and hot band (Stokes) transitions. The pulses are ordered such that the Stokes beam is seen before the pump beam (with some overlap in time) and results in population being put into an eigenstate of the three-level time dependent Hamiltonian (equation (2.65)) which contains only the ground $v = 0$ state and the $v = 2$ state (equation (2.67b)). As long as the adiabatic following condition (equation (2.70)) is met, the population in the ground state will be transferred entirely into the $v = 2$ state.

In a similar manner to the simulations presented in chapter 4, the three-level density matrix equations of motion (2.66) can be solved to model STIRAP. In this case however, the detuning is held constant and instead the Rabi frequencies of both the pump and Stokes lasers become time dependent as the intensity of the lasers is modulated. The equations (2.66) are solved numerically by writing a MATLAB program to set up the equations and perform the integration. The pulses were programmed to have a Gaussian temporal shape $\Omega(t) = \Omega e^{\left(\frac{-t}{\tau}\right)^2}$ with a pulse width τ and the program alters the time delay between the pulses to investigate the optimum delay time for population transfer. Figure 5.9 shows the calculated total population transfer into each of the vibrational levels of NO as a function of the delay between the pump and Stokes pulses with negative delay corresponding to the pump pulse occurring before the Stokes pulse in time. The pulse lengths τ were 1 µs for both pulses, the shortest pulse length achievable with the AOM in the previous section.

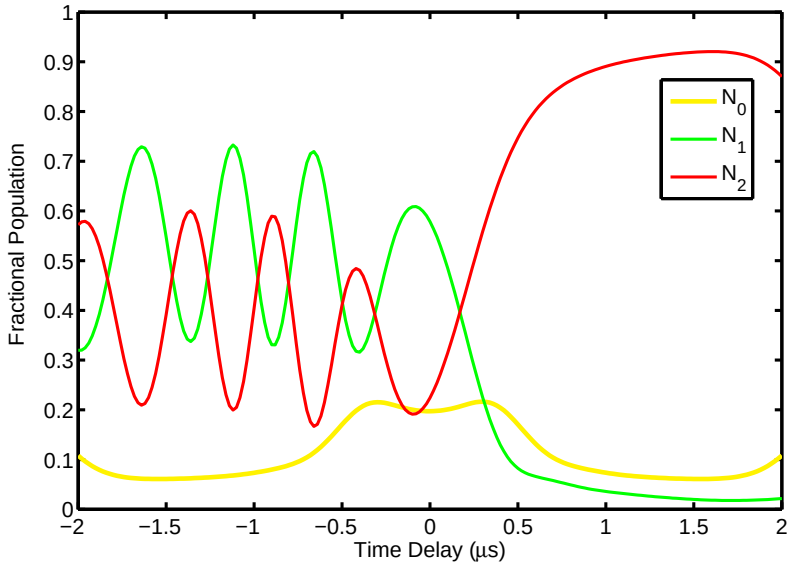

Figure 5.9: The calculated final total population in each vibrational level of the system for changing delay times between the 1 µs pulses. Positive delay times correspond to the counter-intuitive pulse ordering in which the Stokes pulse occurs before the pump pulse. A maximum transfer of 92% occurs for a delay of 1.6 µs.

The input parameters for the model are the Rabi frequencies of the pump and Stokes pulses which were calculated from the measured properties of the lasers (output power, beam radius) and HITRAN values for the simulated transitions (Einstein A factor, transition frequency) along with detuning values for both beams and the dephasing rate which is assumed to be equal for all states. The low tuning range (relative to the EC-QCL) of the DFB-QCL limits the choices of ladder states to attempt STIRAP with and the transitions that have been simulated here are the $\mathrm{R}(6.5)_{\frac{1}{2}}$ $v = 1 \leftarrow 0$ being pumped with the DFB-QCL with the Stokes resonant with the $\mathrm{R}(7.5)_{\frac{1}{2}}$ $v = 2 \leftarrow 1$. The Rabi frequencies were calculated as 14.8 Mrad s^{-1} for the pump and 11.6 Mrad s^{-1} for the Stokes. The detuning values are taken to be the measured linewidths of the lasers (0.8 MHz and 2 MHz respectively) and the dephasing rate was taken to be the self broadening rate at a pressure of 10 mTorr of NO which is 213 kHz. At negative delay times (the intuitive pulse ordering) figure 5.9 shows that population transfer is very sensitive to the pulse timing with the transfer oscillating between the target ($v = 2$) and intermediate ($v = 1$) states depending on the delay time. However with the counter-intuitive pulse sequence (positive delay

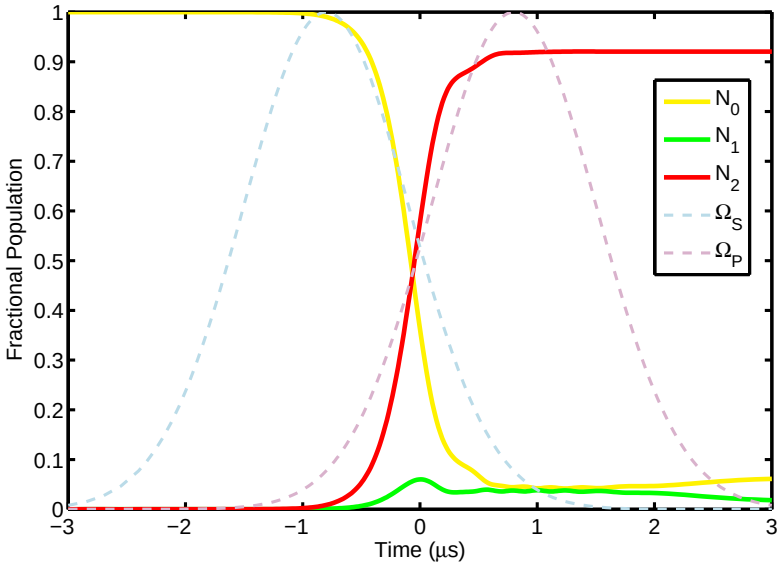

Figure 5.10: The temporal evolution of the populations in the three vibrational levels for the most efficient pulse delay of 1.6 µs. The populations evolve smoothly with little population occupying the intermediate state and the system ends with 92% of the population in the $v = 2$ state.

times), the population transfer into the target is consistently high over a broad range of delay times with little population remaining in either the $v = 0$ or $v = 1$ states.

The maximum population transfer calculated occurs at a pulse delay of 1.6 µs and predicts a total transfer of 92% into the $v = 2$ level. The temporal evolution of the ro-vibrational state populations as the pulses occur is shown in figure 5.10. This shows that only a very small proportion of the total population enters the $v = 1$ level during the process and that the population, which initially starts in the $v = 0$ level is smoothly transferred into the $v = 2$ level. At negative delay times the population transfer into the $v = 2$ state reaches as high as 60% for precisely defined pulse timings, but with positive delays the accuracy of the pulse timing is far less critical with a larger population transfer occurring for a wide range of delay times.

A limitation of the three-level model is that it ignores the fact that the rotational levels are $(2J + 1)$-fold degenerate in the absence of a strong magnetic field. To address this limitation we turn to a more complicated system of equations given by Mukherjee and Zare [142], who treat the Stokes beam as being composed of two opposite circularly polarised components. They then use a graphical method

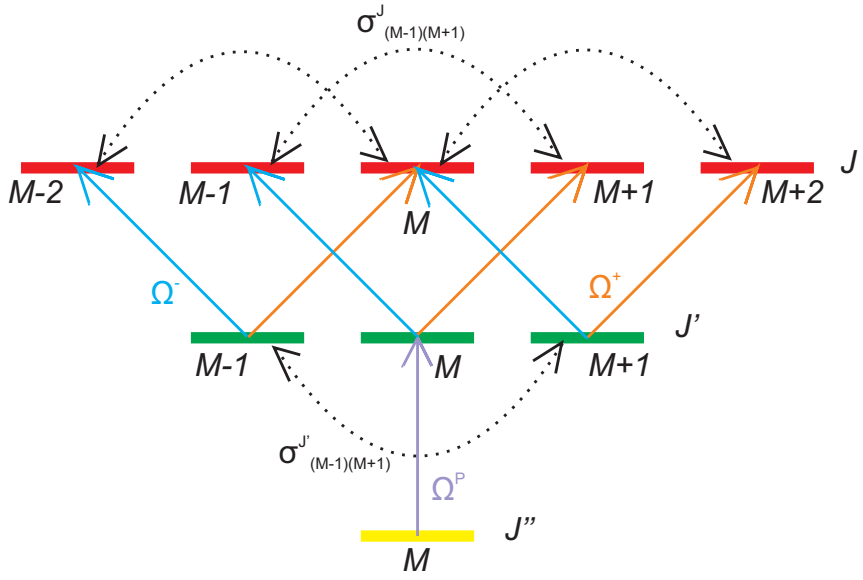

Figure 5.11: A diagram showing a selection of M states, the driving fields, and the coherences between the states. The labels use the notation used by Mukherjee and Zare [142]. J'' corresponds to a rotational state within the ground vibrational state, J' to a rotational state in the $v = 1$ and J to a rotational state in the $v = 2$.

illustrated in figure 5.11 to calculate the coherences between Zeeman levels of the rotational states of the system. The time evolution of the populations (in the notation used by Mukherjee and Zare) are given by

$$\dot{\rho}_M^{J''} = 2\Re\left(i\Omega^P_{(J'',M)(J',M)}\sigma_{(J',M)(J'',M)}\right), \tag{5.5a}$$

$$\dot{\rho}_M^{J'} = 2\Re\left(i\Omega^{P*}_{(J'',M)(J',M)}\sigma_{(J'',M)(J',M)} - i\Omega^{+*}_{(J',M)(J,M+1)}\sigma_{(J',M)(J,M+1)} - i\Omega^{-*}_{(J',M)(J,M-1)}\sigma_{(J',M)(J,M-1)}\right), \tag{5.5b}$$

$$\dot{\rho}_M^{J} = 2\Re\left(i\Omega^{+*}_{(J,M-1)(J,M)}\sigma_{(J,M-1)(J,M)} + i\Omega^{-*}_{(J',M+1)(J,M)}\sigma_{(J',M+1)(J,M)}\right), \tag{5.5c}$$

where J'' denotes rotational level within the ground vibrational state, J' the intermediate state and J the target second ro-vibrationally excited state. The single

photon coherences are given by;

$$\begin{aligned}\dot{\sigma}_{(J',M)(J,M+1)} + i\Delta_S \sigma_{(J',M)(J,M+1)} &= i\Omega^{+}_{(J',M)(J,M+1)} \left(\rho^{J}_{M+1} - \rho^{J'}_{M}\right) \\ &\quad + i\Omega^{-}_{(J',M)(J,M-1)} \sigma^{J}_{(M-1)(M+1)} \\ &\quad - i\Omega^{-}_{(J',M+2)(J,M+1)} \sigma^{J'}_{(M)(M+2)} \\ &\quad + i\Omega^{P*}_{(J'',M)(J',M)} \sigma_{(J'',M)(J,M+1)}, \qquad (5.6a) \\ \dot{\sigma}_{(J',M)(J,M-1)} + i\Delta_S \sigma_{(J',M)(J,M-1)} &= i\Omega^{-}_{(J',M)(J,M-1)} \left(\rho^{J}_{M-1} - \rho^{J'}_{M}\right) \\ &\quad + i\Omega^{+}_{(J',M)(J,M+1)} \sigma^{J}_{(M+1)(M-1)} \\ &\quad - i\Omega^{+}_{(J',M-2)(J,M-1)} \sigma^{J'}_{(M)(M+2)} \\ &\quad + i\Omega^{P*}_{(J'',M)(J',M)} \sigma_{(J'',M)(J,M-1)}, \qquad (5.6b) \\ \dot{\sigma}_{(J'',M)(J',M)} + i\Delta_P \sigma_{(J'',M)(J',M)} &= i\Omega^{P}_{(J'',M)(J',M)} \left(\rho^{J'}_{M+1} - \rho^{J''}_{M}\right) \\ &\quad - i\Omega^{+*}_{(J',M)(J,M+1)} \sigma_{(J'',M)(J',M+2)} \\ &\quad - i\Omega^{-*}_{(J',M)(J,M-1)} \sigma_{(J'',M)(J,M-1)}, \qquad (5.6c)\end{aligned}$$

and the coherences between Zeeman levels by;

$$\begin{aligned}\dot{\sigma}^{J'}_{(M)(M+2)} + \gamma_m \sigma^{J'}_{(M)(M+2)} &= i\Omega^{+}_{(J',M)(J,M+1)} \sigma_{(J,M+1)(J',M+2)} \\ &\quad - i\Omega^{-*}_{(J',M+2)(J,M+1)} \sigma_{(J',M)(J,M+1)}, \qquad (5.7a) \\ \dot{\sigma}^{J}_{(M)(M+2)} + \gamma_m \sigma^{J}_{(M)(M+2)} &= i\Omega^{-*}_{(J',M+1)(J,M)} \sigma_{(J,M+1)(J',M+2)} \\ &\quad - i\Omega^{+}_{(J',M+1)(J,M+2)} \sigma_{(J,M)(J',M+1)}. \qquad (5.7b)\end{aligned}$$

Finally the two-photon coherences are given by;

$$\begin{aligned}\dot{\sigma}_{(J'',M)(J,M-1)} + i\Delta_2 \sigma_{(J'',M)(J,M-1)} &= i\Omega^{P}_{(J'',M)(J',M)} \sigma_{(J',M)(J,M-1)} \\ &\quad - i\Omega^{-}_{(J',M)(J,M-1)} \sigma_{(J'',M)(J',M)}, \qquad (5.8a) \\ \dot{\sigma}_{(J'',M)(J,M+1)} + i\Delta_2 \sigma_{(J'',M)(J,M+1)} &= i\Omega^{P}_{(J'',M)(J',M)} \sigma_{(J',M)(J,M+1)} \\ &\quad - i\Omega^{+}_{(J',M)(J,M+1)} \sigma_{(J'',M)(J',M)}. \qquad (5.8b)\end{aligned}$$

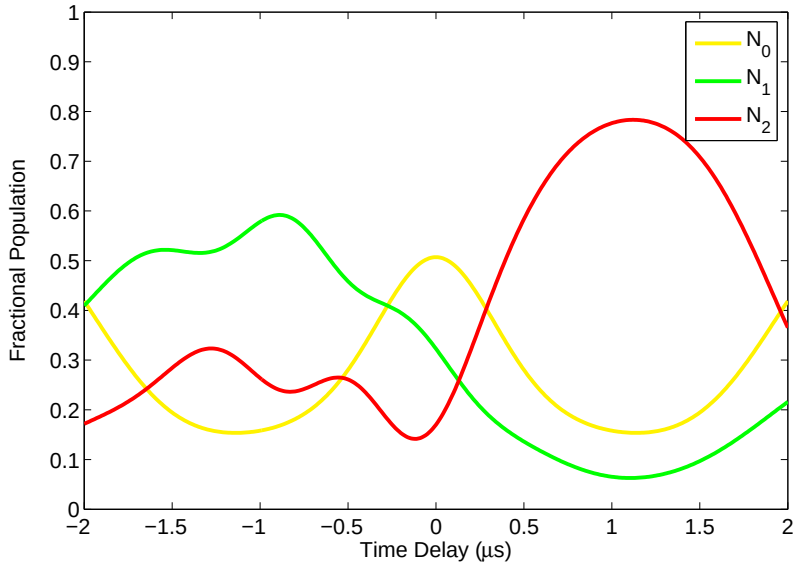

Figure 5.12: The final populations in each of the three vibrational states with various time delays between the pump and Stokes pulses. Negative delays correspond to the pump laser interacting with the system before the Stokes and positive time delays to the counter intuitive pulse ordering. The maximum transfer into the $v = 2$ level is found with a time delay of 1.12 µs which is slightly longer than the 1 µs duration of the pulses. The process is very robust to errors in this time delay as greater than 50% transfer occurs for pulse delays of between 0.5 µs and 1.5 µs.

The Rabi frequencies, Ω, are dependant on the Zeeman level and are modified by the Clebsch-Gordan coefficients, and are given by

$$\Omega^{P}_{(J'',M)(J',M)} = \frac{\mu_{01}E_P}{\hbar}\sqrt{\frac{(J-M-1)(J+M-1)}{(2J-1)(2J-3)}}, \tag{5.9a}$$

$$\Omega^{+}_{(J',M)(J,M+1)} = \frac{-\mu_{12}E_S}{\sqrt{2}\hbar}\sqrt{\frac{(J+M)(J+M+1)}{2(2J-1)(2J+1)}}, \tag{5.9b}$$

$$\Omega^{-}_{(J',M)(J,M-1)} = \frac{\mu_{12}E_S}{\sqrt{2}\hbar}\sqrt{\frac{(J-M)(J-M+1)}{2(2J-1)(2J+1)}}. \tag{5.9c}$$

These equations were again solved numerically in the MATLAB programming environment. The input parameters for this model were the same as for the three-level model and the pulse shapes were again Gaussian with a pulse width of 1 µs. Figure 5.12 shows the total population transfer into each of the vibrational levels as a function of the delay between the pump and Stokes pulses and shows a significant difference from the three-level model. Now, the maximum population transfer into

$v = 2$ is 78.3% and occurs with a pulse delay of 1.12 µs. This time delay is approximately 0.5 µs slower than for the simpler three-level case but is roughly as expected as studies have found that the optimum time delay is roughly equal to the pulse length [143]. The technique is quite robust, in that the timing does not need to be very precise to achieve appreciable population transfer; greater than 50% transfer is achieved into the $v = 2, J = 8.5$ state for pulse delays of between 0.5 µs and 1.5 µs. At negative delay times (intuitive pulse ordering) the maximum population transfer is only 32.3% with a time delay of −1.27 µs, slightly higher than in the incoherent limit, in which the maximum population transfer would be 25%. The population transfer as a function of time is shown for the optimum pulse delay in figure 5.13. As evidenced by the smoothness of the curves the population is being transferred adiabatically; no oscillations occur as they would in Rabi cycling. The dephasing and the Zeeman coherences mean that not all of the population is initially prepared in the so-called dark state as described in chapter 2. This means that some of the population is left in both the ground and middle states, reducing the overall efficiency from 100%. However a population transfer of 78% is still significant.

The model calculates the populations of each of the $(2J + 1)$ individual Zeeman levels and these are shown in figure 5.14. The population is symmetrically distributed around $M = 0$ but weighted towards higher $|M|$, *ie.* the population in the $v = 2, J = 8.5$ state is aligned. This alignment is expected as the two circularly polarised components of the linearly polarised Stokes beam have equal intensities; if they were unequal then the populations would be skewed to one side (either positive or negative M) and the system would be oriented. The density matrix components also allow us to calculate the orientation and alignment parameters which describe the angular momentum polarisation. These parameters are defined by [144, 145]

$$A_q^{(k)} = \frac{c(k)}{\langle JM| J^2 |JM\rangle^{\frac{k}{2}}} \left\langle J_q^{(k)} \right\rangle, \tag{5.10}$$

where $J_q^{(k)}$ are spherical tensors of rank q and order k. The tensor rank q runs from $-k$ to k and a k value of 0 signifies a unipolar operator. A k value of 1

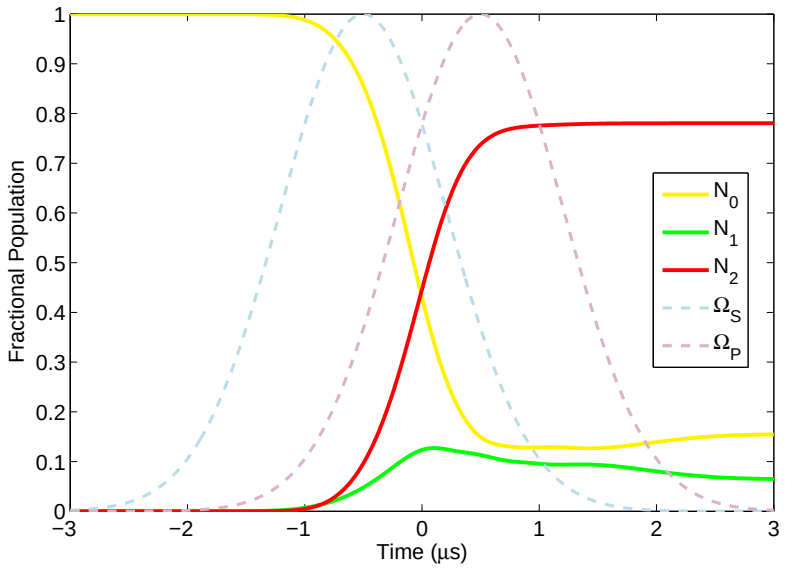

Figure 5.13: The temporal evolution of the populations of the three ro-vibrational levels as a function of time shown with the most efficient pulse delay (1.12 µs). The shapes and timings of the pulses are shown with the pulse heights normalised. The population is transferred smoothly into the $v = 2$ with only a little population escaping into $v = 1$.

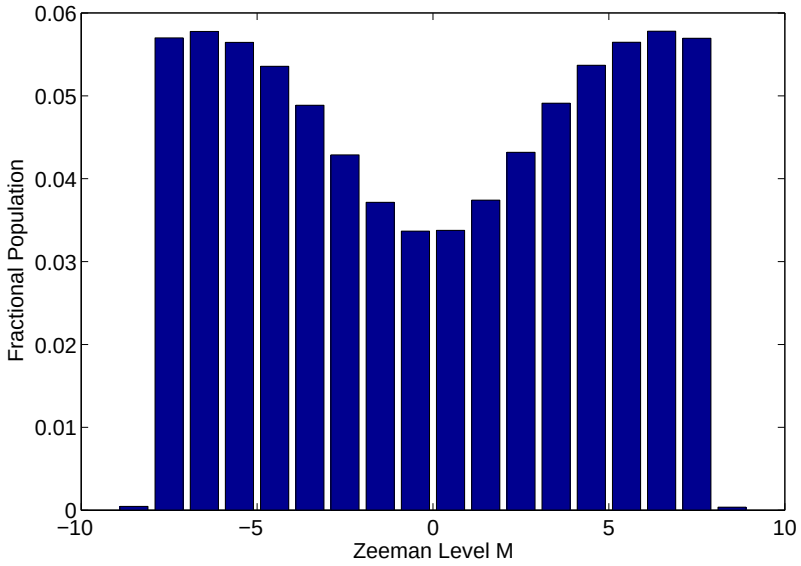

Figure 5.14: The final distribution of population among the M states of the $v = 2, J = 8.5$ level for the most efficient pulse delay.

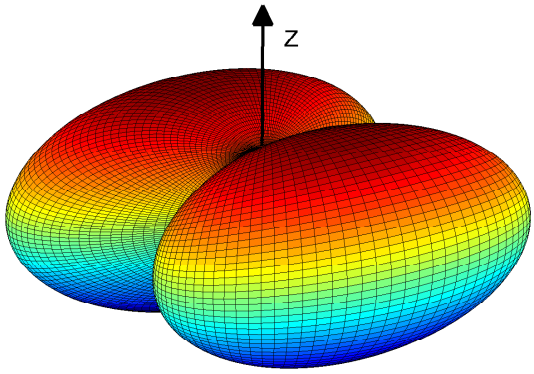

Figure 5.15: The spatial distribution of the angular momentum for the most efficient pulse delay as calculated from the alignment parameters $A_0^{(2)} = -0.075757$ and $A_{\pm 2}^{(2)} = -0.17477$.

is associated with dipolar operations, and $k = 2$ is associated with quadrupolar operations. Since the excitation modelled produces equal populations in $|J, M\rangle$ and $|J, -M\rangle$, the molecule does not become oriented and so the orientation parameter $A_{0,\pm 1}^{(1)} = 0$. The Zeeman coherence however, breaks the cylindrical symmetry and leads to non-zero second order components of the spherical tensor operator $J_q^{(2)}$. These are given by

$$\left\langle J_{\pm 1}^{(2)} \right\rangle = 0, \tag{5.11a}$$

$$\left\langle J_0^{(2)} \right\rangle = \frac{1}{\sqrt{6}} \sum_M \rho_{MM} \left[3M^2 - J\left(J+1\right) \right], \tag{5.11b}$$

$$\left\langle J_{\pm 2}^{(2)} \right\rangle = \frac{1}{2} \sum_M \rho_{MM-2}^J \left[\sqrt{J\left(J+1\right) - \left(M-2\right)\left(M-1\right)} \times \sqrt{J\left(J+1\right) - M\left(M-1\right)} \right]. \tag{5.11c}$$

The spatial distribution of the angular momentum polarisation is then calculated from equations (5.11) using

$$P(\theta, \phi) = \frac{1}{4\pi} \left[1 + \frac{5}{2} A_0^{(2)} \left(3\cos^2\theta - 1 \right) + 5\sqrt{\frac{3}{2}} A_2^{(2)} \sin^2\theta \cos 2\phi \right], \tag{5.12}$$

where θ is the polar angle and ϕ is the azimuthal angle. For the simulation shown in figure 5.13 the corresponding alignment parameters are $A_0^{(2)} = -0.075757$ and $A_{\pm 2}^{(2)} = -0.17477$ which give the overall spatial distribution of the angular momentum shown in figure 5.15. Applying circularly or eliptically polarised light to one of the transitions would result in unequal populations in $|J, M\rangle$ and $|J, -M\rangle$ leading to orientation.

In conclusion this model which incorporates Zeeman coherences and uses measured values of the properties of our lasers even under realistic conditions inside an absorption cell, predicts a significant amount of population transfer (78%). Two AOMs could readily produce the necessary pulses with the cw lasers. In addition such vibrationally excited samples will be formed with well defined angular momentum polarisation.

5.3 Laser Stabilisation

Since achieving two-photon resonance is paramount to STIRAP working, and since neither the DFB-QCL or the EC-QCL is frequency stabilised, it was deemed necessary to attempt to stabilise at least one of the lasers. Lasers of all types exhibit various kinds of noise. The noise may exhibit as frequency fluctuations, phase fluctuations or intensity changes and may be caused by multiple sources such as electrical noise from the current supply or temperature variations. It is possible to counter these fluctuations by applying some kind of feedback to the laser. For example Borri *et al.* have locked a DFB-QCL to a Lamb-dip and used an optical frequency comb synthesizer to measure the absolute frequency to kHz precision. [146]

The basic laser stabilisation setup includes some method by which the fluctuations are measured followed by feedback electronics that convert the measured (fluctuating) signal into a signal to send back to the laser to adjust the output back to the desired state. A schematic of this is shown in figure 5.16. Various methods exist for measuring a change in output frequency of the laser. These generally rely on a measurement that results in an amplitude variation that is proportional to the

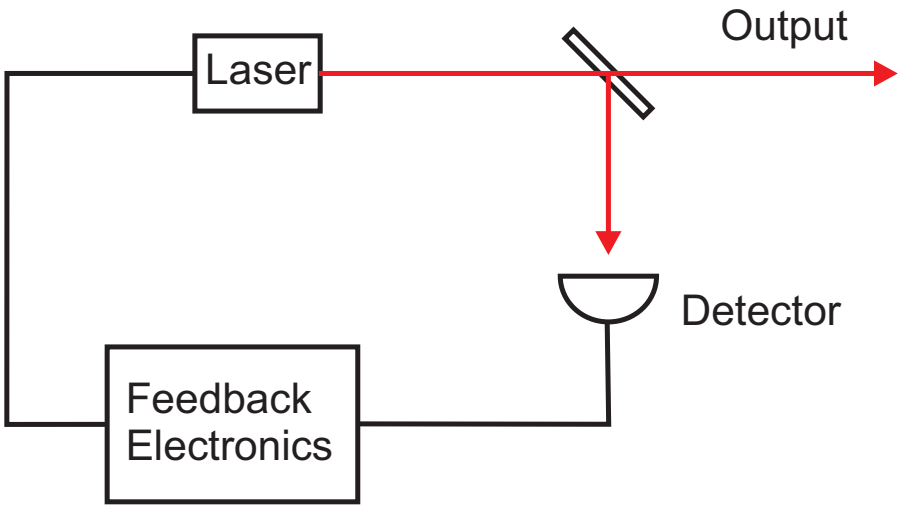

Figure 5.16: A schematic of the basic active stabilisation setup. A detector measures some change in the laser output properties and feedback electronics convert the detector signal into a signal to feed back to the laser to return it to its original output properties.

change in frequency. This may be produced for example by measuring the transmission of a stable reference cavity [147], by measuring the transmission through an absorption cell or by using an interferometer [148]. Many methods rely on modulation of the laser frequency or phase to produce the error signal required to calculate the detuning from the desired frequency [88]. This may broaden the linewidth of the laser, a trait that is undesirable in the kinds of coherent spectroscopy studied in this thesis. Many stabilisation methods are also unable to distinguish between amplitude modulation of the laser and frequency modulation since they rely on the phase difference between different frequencies altering the amplitude of the signal.

Several modulation free techniques exist that deal with the linewidth broadening problem, the most common being Pound-Drever-Hall (PDH) locking in which a stable Fabry-Perrot cavity is used in conjunction with a phase modulator [149, 150]. The phase modulator allows optical sidebands to be added to the laser light which are then directed into the cavity. The reflected light is monitored and the signal demodulated to produce an error signal. The error signal is an odd function, unlike the transmission function of the cavity, which allows a measurement of both how far off resonance the laser is (through its magnitude) but also whether the frequency is higher or lower than resonance (through its sign). The error signal is then fed back

to the laser to return it to resonance. PDH locking is insensitive to laser amplitude fluctuations but requires both complex, expensive electronics and expensive cavity mirrors. For a laser that must be resonant with a certain molecular transition, it would also be necessary to very accurately tune the cavity length.

It was suggested in chapter 4 that two-colour polarisation spectroscopy could be used to lock the two lasers into two-photon resonance; the PS signal is of the correct form for an error signal, being an odd function of detuning with a zero crossing on (two-photon) resonance. Furthermore, the technique is modulation free since the error signal is a direct function of the laser detuning. An attempt was made to stabilise the EC-QCL (as the Stokes or probe laser) by this method and is summarised below.

5.3.1 Experimental: Measuring the Frequency Stability of the DFB-QCL

The experimental setup was largely the same as for the experiments presented in chapter 4 with a few modifications. The probe beam was circularly polarised this time and the chosen transitions were the $\mathrm{R}(6.5)_{\frac{1}{2}}$ $v = 1 \leftarrow 0$ and the $\mathrm{P}(7.5)_{\frac{1}{2}}$ $v = 2 \leftarrow 1$. The same detectors were used as before (VIGO PVMI-3TE-10.6).

Initially the probe laser was scanned across the hot band transition while the pump laser was fixed within the fundamental transition from the e component Λ-doublet. The cell was filled with 150 mTorr of NO and the signals at both detectors were recorded on a 400 MHz oscilloscope (LeCroy Wavesurfer 44MXs-A). The sum of the two detector signals once again gave the absorption signal, which contained both a Doppler absorption component due to the continuous pumping and velocity redistribution in the $v = 1$ level, and an increased absorption around the two-photon resonance as shown in figure 5.17. By comparing the position of the narrow absorption spike to the positions of the maxima of the Doppler broadened incoherent components, it was possible to measure the detuning of the pump beam over time.

Figure 5.18 shows the detuning of the pump (DFB-QCL) over a period of ap-

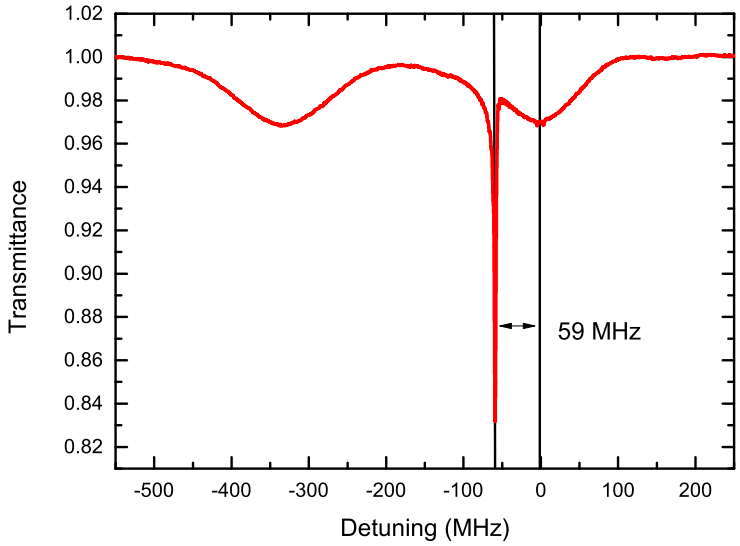

Figure 5.17: Illustrating the detuning of the pump laser. The Doppler profile of the hot band transition is clearly visible and a sharp decrease in the probe transmittance is seen when the probe laser tunes through two-photon resonance. The detuning of the pump laser is measured as shown.

proximately 40 minutes. The detuning oscillates at a rate of about 2 mHz; the mean detuning is -70 MHz indicating that the laser was not tuned to the centre of the pump resonance, although this does not affect the rate at which the laser changes frequency. The oscillating nature of the frequency change indicates that this is not caused by random noise but is most likely due to the TEC cycling causing small ($< 1°$C) changes in the temperature. The width of the detuning keeps the pump laser within the Doppler profile of the transition which has a FWHM of approximately 120 MHz. Moreover the slow changes mean that over the time scale of the coherent phenomena studied, the laser appears to be quite stable. It is therefore reasonable to assume that two-photon resonance could be maintained using two colour polarisation spectroscopy for an appreciable time.

Figure 5.19 shows the difference signal obtained at a pressure of 150 mTorr with a 100 kHz low pass filter. The width of the signal, determined peak-to-peak, is 4 MHz and there is a clear and smooth zero crossing so that it is possible to distinguish positive detuning (higher frequency than desired) from negative. The signal shown appears very suitable for laser frequency stabilisation, although amplitude changes

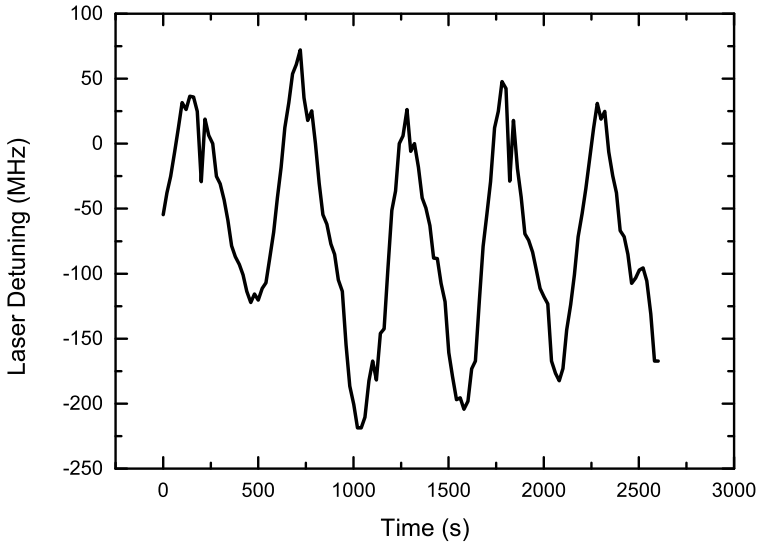

Figure 5.18: The stability of the pump laser over time. The mean detuning is -70 MHz and the detuning oscillates at approximately 2 mHz. This cycling is most likely due to the TEC cycling causing small temperature variations.

in the lasers may result in the amplitude of the signal changing.

A new cell was therefore built and a portion of the probe power (*ca.* 7 mW) was split from the main beam using a ZnSe window as a beam splitter. The pump beam was passed through the new cell and the low power probe beam was passed through a $\frac{\lambda}{4}$ waveplate and then counter propagated through the cell. The probe beam then passed through an analysis polariser and the two components were picked up by the same detectors as previously used. A differential amplifier was built to take the detector outputs, invert one and output the combination which gives the error signal. It was intended to send the error signal to the piezo of the EC-QCL, which has a maximum frequency response of 100 Hz. Unfortunately at this refresh rate the instability of the laser proved to be larger than the 4 MHz width of the error signal and as such it was not possible to stabilise the EC-QCL using this method.

5.3.2 Experimental: Stabilising Using a Scanning Etalon

Another method was then chosen to stabilise the EC-QCL over a long (several minutes) time period, through feedback to the output grating PZT. Figure 5.20

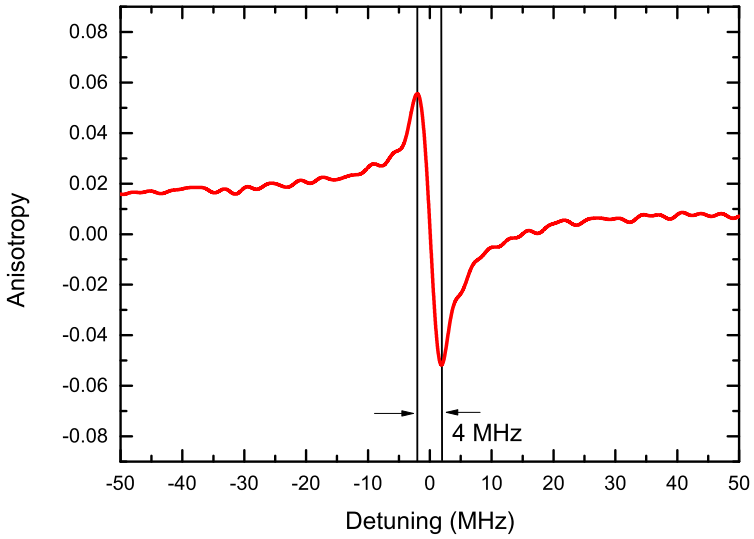

Figure 5.19: The polarisation spectrum for a setup in which the probe beam has been circularly polarised rather than the pump beam. The width of the central zero crossing is 4 MHz.

shows schematically how a scanning etalon (Spectra-Physics SP5945) was used to provide feedback to the laser. The confocal etalon contains a beam splitter, two mirrors and a scanning KBr plate that rotates in order to change the optical path length. The scanning plate is mounted to a motor that is driven at 5 kHz by a lock-in amplifier (Stanford Research Systems SR830). The signal received at the detector is demodulated by the lock-in amplifier to provide an error signal to the laser.

The free spectral range (FSR) of the scanning etalon was measured in the absence of modulation by scanning the EC-QCL over approximately 2 GHz and comparing the output of a Ge etalon with 500 MHz FSRto the output of the scanning etalon. The result is shown in figure 5.21 and comparison between the two gives an FSR of 294.6±17 MHz. The finesse of the scanning etalon, defined as the FRS divided by the width of an individual fringe (measured at 70 MHz FWHM) is approximately 4. While this is very low, it does mean that the error signals are much wider than the 4 MHz width measured using polarisation spectroscopy, making them wider than the frequency instability of the laser and therefore potentially usable for stabilisation.

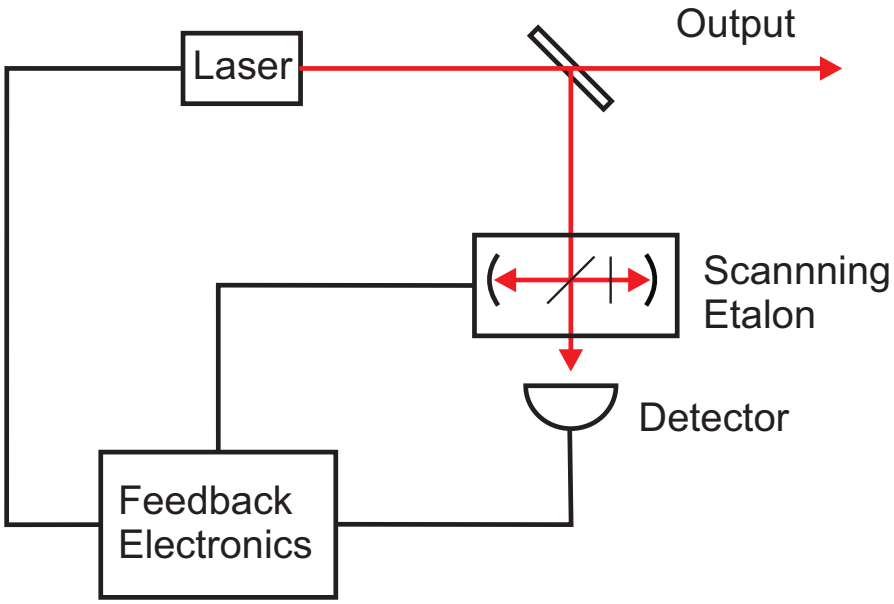

Figure 5.20: A schematic of the experimental set up for using a scanning etalon to stabilise a laser.

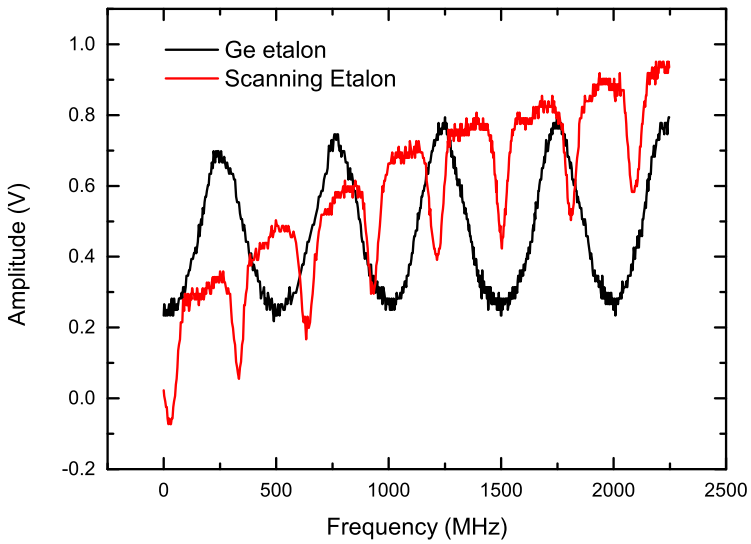

Figure 5.21: The transmission of the scanning etalon (whilst not being scanned) as a function of laser tuning. The transmission of a germanium etalon with a 500 MHz free spectral range is shown for comparison and to set a frequency scale. The free spectral range of the scanning etalon is 294.6±17 MHz.

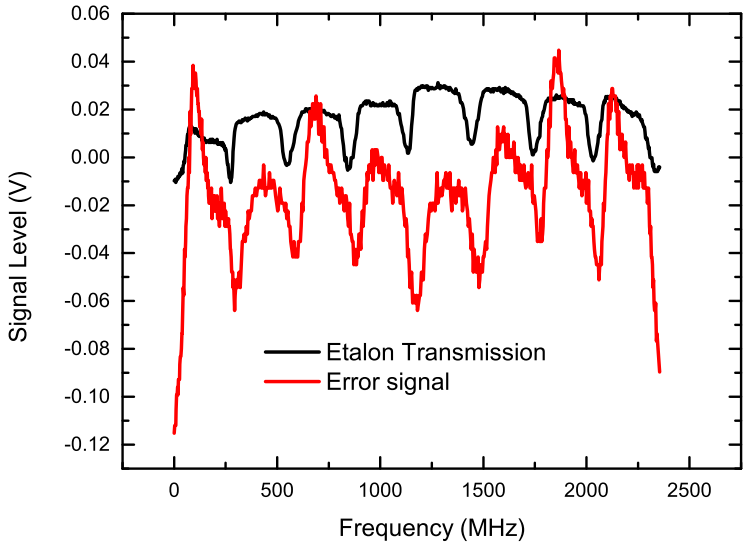

Figure 5.22: The transmission of the scanning etalon and the demodulated error signal produced by the lock-in amplifier.

An example of the demodulated signal from the lock-in amplifier is given in figure 5.22. The EC-QCL was found to tune 1.1 GHz per volt applied to the piezo driver but would not respond to a change in DC signal voltage of less than 6 mV. Unfortunately since this corresponds to a detuning of approximately 6 MHz, it does not seem possible to stabilise the laser to within its linewidth of 2 MHz by feedback to the piezo; it was found that once the error signal was attenuated to a level that would not cause the laser to oscillate, it did not appear to stabilise the laser as the PZT was unable to respond to the signal. The scanning etalon could be driven at up to 10 kHz, but at this highest rate the signal to noise ratio is very poor due a decrease in the modulation depth of the motor used to change the angle of the scanning plate. 10 kHz is the minimum frequency needed to apply a signal to the bias tee input of the EC-QCL and as such this method (using the equipment available) is not suitable for stabilising this particular commercial laser due to the limitations of the device.

To increase the usability of this technique it may be possible to build a scanning etalon with higher finesse, perhaps by increasing the FSR by using cavity mirrors as opposed to the current beam splitter design such that cavity losses are reduced. The

scanning of the etalon should be controlled by mounting one of the mirrors on a piezo which can be driven in the kHz regime and would provide better control over the cavity length than the KBr plate mounted on a motor currently used. This would enable both better signal to noise ratio and higher frequency feedback to overcome the problem of the EC-QCL's limited PZT response. If the EC-QCL were stabilised in this way, the DFB-QCL could potentially still be locked into two-photon resonance using two-colour polarisation spectroscopy. Effective feedback to the lasers has the potential not only to maintain two-photon resonance for an appreciable time but also to narrow the laser linewidths which would increase the population transfer in a STIRAP experiment by decreasing the velocity dephasing.

5.4 Summary and Outlook

In this chapter the operation of a mid-IR AOM was characterised and found to have a rise time of 506 ± 9 ns, allowing the AOM to create a puse of µs length or longer. The AOM was then used as a fast switch to investigate the temporal decay of a transient absorption signal in a pump-probe experiment using low pressures of NO. The signals were found to both decay and broaden over a period of approximately 1.5 µs and the low pressure samples (20 - 80 mTorr) measured showed a strong agreement between the measured decay rate and the published self broadening rate given by HITRAN [119].

The properties of the EC-QCL and the DFB-QCL measured throughout this thesis were then used as input parameters for simulations using the density matrix treatment outlined in chapter 2 to calculated the theoretical population transfer achievable in a STIRAP experiment. A simple three-level model suggested that as much as 92% population transfer could be achieved from the $v = 0, J = 6.5$ ro-vibrational level into the $v = 2, J = 8.5$ level with counter-intuitive pulse ordering and the correct delay between the pulses. A more complex model was then demonstrated based on the equations of Zare and Mukherjee [142], which take into account the $(2J+1)$ degeneracy of the rotational levels of the system. For the same

transitions and input parameters as the three-level model the calculated population transfer was 78% for 1 µs pulse durations. From the calculated density matrix elements it was also possible to construct a plot of the spatial distribution of the angular momentum for the final state and show that the result is an aligned system.

In order to achieve STIRAP using our lasers it is necessary for their frequencies to be stabilised in order to achieve two-photon resonance. To this end several methods were attempted in order to stabilise the commercial EC-QCL. Unfortunately due to the limitations of the commercial EC-QCL it was not possible to sufficiently stabilise this laser using the methods attempted. Polarisation spectroscopy offers a relatively simple, modulation free method of laser frequency stabilisation, but the signals attained in our experiments were too narrow to lock the laser to. An alternative method of polarisation spectroscopy suitable for laser locking demonstrated by Hansch and Couillaud is to put a linear polariser inside a reflecting cavity [151]. The light reflected from the cavity acquires a frequency dependent elliptical polarisation and thus produces an error signal in the same way as polarisation spectroscopy. The width of the error signals is then dependent on the cavity finesse and as such could be made wider than the velocity selected width of the polarisation signals shown in this chapter. In future this may provide a solution to the problem of frequency stabilising the EC-QCL.

Bibliography

[1] C. K. N. Patel, "From CO_2 lasers to quantum cascade lasers - A saga of high power infrared lasers," *Journal of Laser Applications*, vol. 21, no. 4, p. 224, 2009.

[2] J. Butler, A. Calawa, and R. Rediker, "Properties of the PbSe diode laser," *IEEE Journal of Quantum Electronics*, vol. 1, pp. 4–7, Apr. 1965.

[3] M. Tacke, "Lead-salt lasers," *Philosophical Transactions of the Royal Society A: Mathematical, Physical and Engineering Sciences*, vol. 359, pp. 547–566, Mar. 2001.

[4] M. Bass, P. Franken, A. Hill, C. Peters, and G. Weinreich, "Optical Mixing," *Physical Review Letters*, vol. 8, pp. 18–18, Jan. 1962.

[5] O. Levi, T. J. Pinguet, T. Skauli, L. A. Eyres, K. R. Parameswaran, J. S. Harris, M. M. Fejer, T. J. Kulp, S. E. Bisson, B. Gerard, E. Lallier, and L. Becouarn, "Difference frequency generation of 8-μm radiation in orientation-patterned GaAs," *Optics letters*, vol. 27, pp. 2091–3, Dec. 2002.

[6] C.-C. Liao, Y.-H. Lien, K.-Y. Wu, Y.-R. Lin, and J.-T. Shy, "Widely tunable difference frequency generation source for high-precision mid-infrared spectroscopy," *Optics express*, vol. 21, pp. 9238–46, Apr. 2013.

[7] J. Faist, F. Capasso, D. L. Sivco, C. Sirtori, A. L. Hutchinson, and A. Cho, "Quantum cascade laser," *Science (New York, N.Y.)*, vol. 264, pp. 553–6, Apr. 1994.

[8] R. Maulini, I. Dunayevskiy, A. Lyakh, A. Tsekoun, C. Patel, L. Diehl, C. Pflügl, and F. Capasso, "Widely tunable high-power external cavity quantum cascade laser operating in continuous-wave at room temperature," *Electronics Letters*, vol. 45, no. 2, p. 107, 2009.

[9] S. Bartalini, S. Borri, P. Cancio, A. Castrillo, I. Galli, G. Giusfredi, D. Mazzotti, L. Gianfrani, and P. De Natale, "Observing the Intrinsic Linewidth of a Quantum-Cascade Laser: Beyond the Schawlow-Townes Limit," *Physical Review Letters*, vol. 104, p. 083904, Feb. 2010.

[10] R. F. Curl, F. Capasso, C. Gmachl, A. A. Kosterev, B. McManus, R. Lewicki, M. Pusharsky, G. Wysocki, and F. K. Tittel, "Quantum cascade lasers in chemical physics," *Chemical Physics Letters*, vol. 487, pp. 1–18, Feb. 2010.

[11] Y. Yao, A. J. Hoffman, and C. F. Gmachl, "Mid-infrared quantum cascade lasers," *Nature Photonics*, vol. 6, pp. 432–439, June 2012.

[12] J. M. Supplee, E. A. Whittaker, and W. Lenth, "Theoretical description of frequency modulation and wavelength modulation spectroscopy," *Applied optics*, vol. 33, pp. 6294–302, Sept. 1994.

[13] K. Namjou, S. Cai, E. A. Whittaker, J. Faist, C. Gmachl, F. Capasso, D. L. Sivco, and a. Y. Cho, "Sensitive absorption spectroscopy with a room-temperature distributed-feedback quantum-cascade laser," *Optics Letters*, vol. 23, p. 219, Feb. 1998.

[14] S. Cristescu, S. Persijn, S. te Lintel Hekkert, and F. Harren, "Laser-based systems for trace gas detection in life sciences," *Applied Physics B*, vol. 92, pp. 343–349, Aug. 2008.

[15] G. Hancock, J. H. van Helden, R. Peverall, G. A. D. Ritchie, and R. J. Walker, "Direct and wavelength modulation spectroscopy using a cw external cavity quantum cascade laser," *Applied Physics Letters*, vol. 94, no. 20, p. 201110, 2009.

[16] M. Mazurenka, A. J. Orr-Ewing, R. Peverall, and G. A. D. Ritchie, "Cavity ring-down and cavity enhanced spectroscopy using diode lasers," *Annual Reports Section "C" (Physical Chemistry)*, vol. 101, p. 100, 2005.

[17] S. Welzel, G. Lombardi, P. B. Davies, R. Engeln, D. C. Schram, and J. Röpcke, "Trace gas measurements using optically resonant cavities and quantum cascade lasers operating at room temperature," *Journal of Applied Physics*, vol. 104, no. 9, p. 093115, 2008.

[18] G. Berden and R. Engeln, eds., *Cavity Ring-Down Spectroscopy.* Wiley, 2009.

[19] S. G. Baran, G. Hancock, R. Peverall, G. A. D. Ritchie, and N. J. van Leeuwen, "Optical feedback cavity enhanced absorption spectroscopy with diode lasers," *The Analyst*, vol. 134, pp. 243–9, Feb. 2009.

[20] J. H. van Helden, N. Lang, U. Macherius, H. Zimmermann, and J. Röpcke, "Sensitive trace gas detection with cavity enhanced absorption spectroscopy using a continuous wave external-cavity quantum cascade laser," *Applied Physics Letters*, vol. 103, no. 13, p. 131114, 2013.

[21] G. Hancock, G. Ritchie, J.-P. van Helden, R. Walker, and D. Weidmann, "Applications of midinfrared quantum cascade lasers to spectroscopy," *Optical Engineering*, vol. 49, no. 11, p. 111121, 2010.

[22] R. Kazarinov and R. Suris, "Possibility of amplification of electromagnetic waves in a semiconductor with a superlattice," *Fizika i Tekhnika Poluprovodnikov*, vol. 5, no. 4, pp. 797–800, 1971.

[23] A. Beattie and P. Landsberg, "Auger effect in semiconductors," *Procedings of the Royal Society of London. Series A, Mathematical and Physical Sciences*, vol. 249, no. 1256, pp. 16–29, 1959.

[24] A. Hugi, R. Maulini, and J. Faist, "External cavity quantum cascade laser," *Semiconductor Science and Technology*, vol. 25, p. 083001, Aug. 2010.

[25] T. Hosoda, G. Kipshidze, L. Shterengas, and G. Belenky, "Single spatial mode 3 μm diode lasers with continuous-wave output power of 15 mW at room temperature," *Electronics Letters*, vol. 47, no. 24, p. 1341, 2011.

[26] L. Shterengas, G. Belenky, T. Hosoda, G. Kipshidze, and S. Suchalkin, "Continuous wave operation of diode lasers at 3.36 μm at 12 °C," *Applied Physics Letters*, vol. 93, no. 1, p. 011103, 2008.

[27] K. Vizbaras and M.-C. Amann, "3.6 μm GaSb-based type-I lasers with quinternary barriers, operating at room temperature," *Electronics Letters*, vol. 47, no. 17, p. 980, 2011.

[28] C. Gmachl and F. Capasso, "Recent progress in quantum cascade lasers and applications," *Reports on progress in Physics*, vol. 1533, 2001.

[29] C. Sirtori, P. Kruck, S. Barbieri, P. Collot, J. Nagle, M. Beck, J. Faist, and U. Oesterle, "GaAs/$Al_xGa_{1-x}As$ quantum cascade lasers," *Applied Physics Letters*, vol. 73, no. 24, p. 3486, 1998.

[30] J. Faist, M. Beck, T. Aellen, and E. Gini, "Quantum-cascade lasers based on a bound-to-continuum transition," *Applied Physics Letters*, vol. 78, no. 2, p. 147, 2001.

[31] C. Pflügl, W. Schrenk, S. Anders, G. Strasser, C. Becker, C. Sirtori, Y. Bonetti, and a. Muller, "High-temperature performance of GaAs-based bound-to-continuum quantum-cascade lasers," *Applied Physics Letters*, vol. 83, no. 23, p. 4698, 2003.

[32] R. Maulini, M. Beck, J. Faist, and E. Gini, "Broadband tuning of external cavity bound-to-continuum quantum-cascade lasers," *Applied Physics Letters*, vol. 84, no. 10, p. 1659, 2004.

[33] O. Malis, C. Gmachl, D. L. Sivco, L. N. Pfeiffer, A. M. Sergent, and K. W. West, "The quantum cascade laser: A versatile high-power semiconductor laser

for mid-infrared applications," *Bell Labs Technical Journal*, vol. 10, pp. 199–214, Nov. 2005.

[34] Y. Bai, S. R. Darvish, S. Slivken, W. Zhang, A. Evans, J. Nguyen, and M. Razeghi, "Room temperature continuous wave operation of quantum cascade lasers with watt- level optical power," *Applied Physics Letters*, vol. 92, no. 10, p. 101105, 2008.

[35] Y. Bai, S. Slivken, S. Kuboya, S. R. Darvish, and M. Razeghi, "Quantum cascade lasers that emit more light than heat," *Nature Photonics*, vol. 4, pp. 99–102, Jan. 2010.

[36] A. Lyakh, R. Maulini, A. Tsekoun, R. Go, C. Pflügl, L. Diehl, Q. J. Wang, F. Capasso, and C. K. N. Patel, "3 W continuous-wave room temperature single-facet emission from quantum cascade lasers based on nonresonant extraction design approach," *Applied Physics Letters*, vol. 95, no. 14, p. 141113, 2009.

[37] N. Bandyopadhyay, Y. Bai, B. Gokden, A. Myzaferi, S. Tsao, S. Slivken, and M. Razeghi, "Watt level performance of quantum cascade lasers in room temperature continuous wave operation at $\lambda \sim 3.76$ μm," *Applied Physics Letters*, vol. 97, no. 13, p. 131117, 2010.

[38] A. Tsekoun, R. Go, M. Pushkarsky, M. Razeghi, and C. K. N. Patel, "Improved performance of quantum cascade lasers through a scalable, manufacturable epitaxial-side-down mounting process," *Proceedings of the National Academy of Sciences of the United States of America*, vol. 103, pp. 4831–5, Mar. 2006.

[39] M. L. Hamilton, G. A. D. Ritchie, Y. Arita, and P. Ewart, "Multi-mode absorption spectroscopy, MUMAS, using wavelength modulation and cavity enhancement techniques," *Applied Physics B*, vol. 100, pp. 665–673, May 2010.

[40] J. H. Northern, a. W. J. Thompson, M. L. Hamilton, and P. Ewart, "Multi-species detection using multi-mode absorption spectroscopy (MUMAS)," *Applied Physics B*, vol. 111, pp. 627–635, Mar. 2013.

[41] H. Kogelnik, "Stimulated Emission in a Periodic Structure," *Applied Physics Letters*, vol. 18, no. 4, p. 152, 1971.

[42] H. Kogelnik, "Coupled-Wave Theory of Distributed Feedback Lasers," *Journal of Applied Physics*, vol. 43, no. 5, p. 2327, 1972.

[43] J. Faist, C. Gmachl, F. Capasso, C. Sirtori, D. L. Sivco, J. N. Baillargeon, and A. Y. Cho, "Distributed feedback quantum cascade lasers," *Applied Physics Letters*, vol. 70, no. 20, p. 2670, 1997.

[44] D. F. Arnone and T. Day, "Compact external cavity mid-ir optical lasers," 2009. European Patent Number EP2074685 A2.

[45] "www.daylightsolutions.com/technology/qcl_technology.htm."

[46] A. Wakita and K. Sugiyama, "Single-frequency external-cavity tapered diode laser in a double-ended cavity configuration," *Review of Scientific Instruments*, vol. 71, no. 1, p. 1, 2000.

[47] C. J. Hawthorn, K. P. Weber, and R. E. Scholten, "Littrow configuration tunable external cavity diode laser with fixed direction output beam," *Review of Scientific Instruments*, vol. 72, no. 12, p. 4477, 2001.

[48] A. Kosterev, G. Wysocki, Y. Bakhirkin, S. So, R. Lewicki, M. Fraser, F. Tittel, and R. Curl, "Application of quantum cascade lasers to trace gas analysis," *Applied Physics B*, vol. 90, pp. 165–176, Dec. 2007.

[49] A. A. Kosterev, A. L. Malinovsky, F. K. Tittel, C. Gmachl, F. Capasso, D. L. Sivco, J. N. Baillargeon, A. L. Hutchinson, and A. Y. Cho, "Cavity Ringdown Spectroscopic Detection of Nitric Oxide with a Continuous-Wave Quantum-Cascade Laser," *Applied Optics*, vol. 40, no. 30, p. 5522, 2001.

[50] D. Nelson, J. Shorter, J. McManus, and M. Zahniser, "Sub-part-per-billion detection of nitric oxide in air using a thermoelectrically cooled mid-infrared quantum cascade laser spectrometer," *Applied Physics B: Lasers and Optics*, vol. 75, pp. 343–350, Sept. 2002.

[51] C. R. Webster, G. J. Flesch, D. C. Scott, J. E. Swanson, R. D. May, W. S. Woodward, C. Gmachl, F. Capasso, D. L. Sivco, J. N. Baillargeon, a. L. Hutchinson, and a. Y. Cho, "Quantum-cascade laser measurements of stratospheric methane and nitrous oxide," *Applied optics*, vol. 40, pp. 321–6, Jan. 2001.

[52] A. Schawlow and C. Townes, "Infrared and Optical Masers," *Physical Review*, vol. 112, pp. 1940–1949, Dec. 1958.

[53] C. Henry, "Theory of the linewidth of semiconductor lasers," *IEEE Journal of Quantum Electronics*, vol. 18, pp. 259–264, Feb. 1982.

[54] J. von Staden, T. Gensty, W. Elsässer, G. Giuliani, and C. Mann, "Measurements of the alpha factor of a distributed-feedback quantum cascade laser by an optical feedback self-mixing technique," *Optics letters*, vol. 31, pp. 2574–6, Sept. 2006.

[55] T. Aellen, R. Maulini, R. Terazzi, N. Hoyler, M. Giovannini, J. Faist, S. Blaser, and L. Hvozdara, "Direct measurement of the linewidth enhancement factor by optical heterodyning of an amplitude-modulated quantum cascade laser," *Applied Physics Letters*, vol. 89, no. 9, p. 091121, 2006.

[56] M. Yamanishi and T. Edamura, "Theory of the intrinsic linewidth of quantum-cascade lasers: Hidden reason for the narrow linewidth and line-broadening by thermal photons," *IEEE Journal of Quantum Electronics*, vol. 44, no. 1, pp. 12–29, 2008.

[57] S. D. Saliba and R. E. Scholten, "Linewidths below 100 kHz with external cavity diode lasers.," *Applied optics*, vol. 48, pp. 6961–6, Dec. 2009.

[58] S. Bartalini, S. Borri, I. Galli, G. Giusfredi, D. Mazzotti, T. Edamura, N. Akikusa, M. Yamanishi, and P. De Natale, "Measuring frequency noise and intrinsic linewidth of a room-temperature DFB quantum cascade laser," *Optics express*, vol. 19, pp. 17996–8003, Sept. 2011.

[59] N. Mukherjee, R. Go, and C. K. N. Patel, "Linewidth measurement of external grating cavity quantum cascade laser using saturation spectroscopy," *Applied Physics Letters*, vol. 92, no. 11, p. 111116, 2008.

[60] S. W. Sharpe, J. F. Kelly, J. S. Hartman, C. Gmachl, F. Capasso, D. L. Sivco, J. N. Baillargeon, and A. Y. Cho, "High-resolution (Doppler-limited) spectroscopy using quantum-cascade distributed-feedback lasers," *Optics letters*, vol. 23, pp. 1396–8, Sept. 1998.

[61] J. Remillard, D. Uy, W. Weber, F. Capasso, C. Gmachl, A. Hutchinson, D. Sivco, J. Baillargeon, and A. Cho, "Sub-Doppler resolution limited Lamb-dip spectroscopy of NO with a quantum cascade distributed feedback laser," *Optics express*, vol. 7, pp. 243–8, Sept. 2000.

[62] N. Mukherjee and C. K. N. Patel, "Molecular fine structure and transition dipole moment of NO2 using an external cavity quantum cascade laser," *Chemical Physics Letters*, vol. 462, pp. 10–13, Sept. 2008.

[63] A. Einstein, "Zur quantentheorie der strahlung," *Physikalische Zeitschrift*, 1917.

[64] P. M. Farrell and W. R. MacGillivray, "On the consistency of Rabi frequency calculations," *Journal of Physics A: Mathematical and General*, vol. 28, pp. 209–221, Jan. 1995.

[65] J. S. Melinger, S. R. Gandhi, A. Hariharan, D. Goswami, and W. S. Warren, "Adiabatic population transfer with frequency-swept laser pulses," *The Journal of Chemical Physics*, vol. 101, no. 8, p. 6439, 1994.

[66] M. M. T. Loy, "Observation of population inversion by optical adiabatic rapid passage," *Physical Review Letters*, vol. 32, no. 15, pp. 814–817, 1974.

[67] J. C. McGurk, T. G. Schmalz, and W. H. Flygare, "Fast passage in rotational spectroscopy: Theory and experiment," *The Journal of Chemical Physics*, vol. 60, no. 11, p. 4181, 1974.

[68] S. Avrillier, J.-M. Raimond, C. Bordé, D. Bassi, and G. Scoles, "Supersonic beam spectroscopy of low J transitions of the ν_3 band of SF_6: Rabi oscillations and adiabatic rapid passage with a CW laser," *Optics Communications*, vol. 39, pp. 311–315, Nov. 1981.

[69] A. Adam, T. Gough, N. Isenor, and G. Scoles, "Rabi oscillations and rapid-passage effects in the molecular-beam CO_2-laser Stark spectroscopy of CH_3F," *Physical Review A*, vol. 32, pp. 1451–1457, Sept. 1985.

[70] J. Kroon, H. Senhorst, H. Beijerinck, B. Verhaar, and N. Verster, "Rabi oscillations in the optical pumping of a metastable neon beam with a cw dye laser," *Physical Review A*, vol. 31, no. 6, pp. 3724–3732, 1985.

[71] S. M. Hamadani, A. T. Mattick, N. A. Kurnit, and A. Javan, "Observation of adiabatic rapid passage utilizing narrow infrared saturation resonances," *Applied Physics Letters*, vol. 27, no. 1, p. 21, 1975.

[72] U. Gaubatz, P. Rudecki, and M. Becker, "Population switching between vibrational levels in molecular beams," *Chemical Physics*, vol. 149, pp. 463–468, Sept. 1988.

[73] U. Gaubatz, P. Rudecki, S. Schiemann, and K. Bergmann, "Population transfer between molecular vibrational levels by stimulated Raman scattering with partially overlapping laserfields. A new concept and experimental results," *The Journal of Chemical Physics*, vol. 92, no. 9, pp. 5363–5376, 1990.

[74] G. Duxbury, N. Langford, M. T. McCulloch, and S. Wright, "Quantum cascade semiconductor infrared and far-infrared lasers: from trace gas sensing to non-linear optics," *Chemical Society reviews*, vol. 34, pp. 921–34, Nov. 2005.

[75] M. T. McCulloch, G. Duxbury, and N. Langford, "Observation of saturation and rapid passage signals in the 10.25 micron spectrum of ethylene using a frequency chirped quantum cascade laser," *Molecular Physics*, vol. 104, pp. 2767–2779, Aug. 2006.

[76] G. Duxbury, N. Langford, M. T. Mcculloch, and S. Wright, "Rapid passage induced population transfer and coherences in the 8 micron spectrum of nitrous oxide," *Molecular Physics*, vol. 105, pp. 741–754, Mar. 2007.

[77] E. A. McCormack, H. S. Lowth, M. T. Bell, D. Weidmann, and G. A. D. Ritchie, "Population transfer and rapid passage effects in a low pressure gas using a continuous wave quantum cascade laser," *The Journal of Chemical Physics*, vol. 137, p. 034306, July 2012.

[78] R. J. Walker, J. H. van Helden, J. Kirkbride, E. A. McCormack, M. T. Bell, D. Weidmann, and G. A. D. Ritchie, "Rapid passage signals from a vibrationally excited target molecule: a pump and probe experiment with continuous wave quantum cascade lasers," *Optics Letters*, vol. 36, pp. 4725–7, Dec. 2011.

[79] D. Grischkowsky and M. Loy, "Self-induced adiabatic rapid passage," *Physical Review A*, vol. 12, no. 1, pp. 1117–1120, 1975.

[80] G. Duxbury, J. F. Kelly, T. A. Blake, and N. Langford, "The ac Stark effect in nitric oxide induced by rapidly swept continuous wave quantum cascade lasers," *The Journal of chemical physics*, vol. 136, p. 174318, May 2012.

[81] G. Duxbury, J. F. Kelly, T. A. Blake, and N. Langford, "Sub-Doppler spectra of infrared hyperfine transitions of nitric oxide using a pulse modulated quantum cascade laser: rapid passage, free induction decay, and the ac Stark effect," *The Journal of chemical physics*, vol. 136, p. 174319, May 2012.

[82] F. Bloch, "Nuclear induction," *Physical review*, vol. 70, pp. 460–473, 1946.

[83] J. Olivero and R. Longbothum, "Empirical fits to the Voigt line width: A brief review," *Journal of Quantitative Spectroscopy and Radiative Transfer*, vol. 17, pp. 233–236, Feb. 1977.

[84] R. Dicke, "The Effect of Collisions upon the Doppler Width of Spectral Lines," *Physical Review*, vol. 89, pp. 472–473, Jan. 1953.

[85] L. Galatry, "Simultaneous Effect of Doppler and Foreign Gas Broadening on Spectral Lines," *Physical Review*, vol. 122, pp. 1218–1223, May 1961.

[86] S. G. Rautian and I. I. Sobelman, "The Effect of Collisions on the Doppler Broadening of Spectral Lines," *Soviet Physics Uspekhi*, vol. 9, pp. 701–716, May 1967.

[87] P. Berman, "Speed-dependent collisional width and shift parameters in spectral profiles," *Journal of Quantitative Spectroscopy and Radiative Transfer*, vol. 12, no. 1324, pp. 1331–1342, 1972.

[88] W. Demtröder, *Laser Spectroscopy*. Berlin Heidelberg New York: Springer-Verlag, 3 ed., 2003.

[89] S. E. Harris, "Electromagnetically Induced Transparency," *Physics Today*, vol. 50, no. 7, p. 36, 1997.

[90] W. Lamb, "Theory of an Optical Maser," *Physical Review*, vol. 134, pp. A1429–A1450, June 1964.

[91] V. S. Letokhov, "High resolution laser spectroscopy," in *High-Resolution Laser Spectroscopy* (K. Shimoda, ed.), vol. 12, p. 96, Berlin: Springer-Verlag, 1976.

[92] C. Wieman and T. Hänsch, "Doppler-Free Laser Polarization Spectroscopy," *Physical Review Letters*, vol. 36, pp. 1170–1173, May 1976.

[93] W. Ernst, "Doppler-free polarization spectroscopy of diatomic molecules in flame reactions," *Optics Communications*, vol. 44, no. 3, 1983.

[94] J. von Neumann, "Wahrscheinlichkeitstheoretischer Aufbau der Quantenmechanik," *Nachrichten von der Gesellschaft der Wissenschaften zu Göttingen, Mathematisch-Physikalische Klasse*, 1927.

[95] H. Torrey, "Transient Nutations in Nuclear Magnetic Resonance," *Physical Review*, vol. 76, pp. 1059–1068, Oct. 1949.

[96] H. Torrey, "Bloch equations with diffusion terms," *Physical Review*, vol. 104, pp. 563–565, Nov. 1956.

[97] R. P. Feynman, F. L. Vernon, and R. W. Hellwarth, "Geometrical Representation of the Schrödinger Equation for Solving Maser Problems," *Journal of Applied Physics*, vol. 28, no. 1, p. 49, 1957.

[98] C. L. Tang, "Optical Analog of the Transient Nutation Effect," *Applied Physics Letters*, vol. 10, no. 5, p. 145, 1967.

[99] L. Allen and J. H. Eberly, *Optical Resonance and Two-Level Atoms*. Ney York: Dover Publications, reprint ed ed., 1987.

[100] R. Boyd, *Nonlinear Optics*. Academic Press, 2 ed., 2003.

[101] V. Letokhov and V. Chebotayev, *Nonlinear Laser Spectroscopy*. Springer-Verlag, 1977.

[102] R. Brewer and R. Shoemaker, "Photo echo and optical nutation in molecules," *Physical Review Letters*, vol. 27, no. September, 1971.

[103] R. Brewer and R. Shoemaker, "Optical free induction decay," *Physical Review A*, vol. 6, no. 6, pp. 2001–2007, 1972.

[104] V. Malinovsky and J. Krause, "General theory of population transfer by adiabatic rapid passage with intense, chirped laser pulses," *The European Physical Journal D*, vol. 14, pp. 147–155, May 2001.

[105] J. H. Northern, G. A. D. Ritchie, E. P. Smakman, J. H. Helden, R. J. Walker, and G. Duxbury, "Chirped quantum cascade laser induced rapid passage signatures in an optically thick gas," *Applied Physics B*, vol. 102, pp. 37–42, Aug. 2010.

[106] N. Tasinato, K. G. Hay, N. Langford, G. Duxbury, and D. Wilson, "Time dependent measurements of nitrous oxide and carbon dioxide collisional relaxation processes by a frequency down-chirped quantum cascade laser: rapid passage signals and the time dependence of collisional processes," *The Journal of chemical physics*, vol. 132, p. 164301, Apr. 2010.

[107] G. Duxbury, J. F. Kelly, T. A. Blake, and N. Langford, "Observation of infrared free-induction decay and optical nutation signals from nitrous oxide using a current modulated quantum cascade laser," *The Journal of chemical physics*, vol. 136, p. 174317, May 2012.

[108] N. V. Vitanov, T. Halfmann, B. W. Shore, and K. Bergmann, "Laser-induced population transfer by adiabatic passage techniques," *Annual review of physical chemistry*, vol. 52, pp. 763–809, Jan. 2001.

[109] T. Laine and S. Stenholm, "Adiabatic processes in three-level systems," *Physical review. A*, vol. 53, pp. 2501–2512, Apr. 1996.

[110] M. Fewell, B. Shore, and K. Bergmann, "Coherent population transfer among three states: Full algebraic solutions and the relevance of non adiabatic processes to transfer by delayed pulses," *Australian Journal of Physics*, vol. 50, no. 2, pp. 281–308, 1997.

[111] K. Bergmann, H. Theuer, and B. W. Shore, "Coherent population transfer among quantum states of atoms and molecules," *Reviews of Modern Physics*, vol. 70, pp. 1003–1025, July 1998.

[112] N. Mukherjee and R. N. Zare, "Preparation of polarized molecules using coherent infrared multicolor ladder excitation," *The Journal of chemical physics*, vol. 132, p. 154302, Apr. 2010.

[113] A. Tay, T. W. Ng, Y. Wang, and S. Zhao, "Direct measurement of beam size in a spectroscopic ellipsometry setup," *The Review of scientific instruments*, vol. 79, p. 063101, June 2008.

[114] J. Brown and A. Carrington, *Rotational Spectroscopy of Diatomic Molecules*. Cambridge University Press, 2003.

[115] J. Brown, J. Hougen, K.-P. Huber, J. Johns, I. Kopp, H. Lefebvre-Brion, A. Merer, D. Ramsay, J. Rostas, and R. Zare, "The labeling of parity doublet levels in linear molecules," *Journal of Molecular Spectroscopy*, vol. 55, pp. 500–503, Mar. 1975.

[116] I. Kovács and I. Péczeli, "On Λ - type doubling in multiplet states of diatomic molecules," *Journal of Molecular Structure*, vol. 80, pp. 39–41, Mar. 1982.

[117] P. Atkins and R. S. Friedman, *Molecular Quantum Mechanics*. Oxford: Oxford University Press, third edit ed., 1997.

[118] W. Meerts and A. Dymanus, "The Hyperfine Λ-Doubling Spectrum of $^{14}N^{16}O$ and $^{15}N^{16}O$," *Journal of Molecular Spectroscopy*, vol. 44, pp. 320–346, Nov. 1972.

[119] L. Rothman, I. Gordon, A. Barbe, D. Benner, P. Bernath, M. Birk, V. Boudon, L. Brown, A. Campargue, J.-P. Champion, K. Chance, L. Coudert, V. Dana, V. Devi, S. Fally, J.-M. Flaud, R. Gamache, A. Goldman, D. Jacquemart, I. Kleiner, N. Lacome, W. Lafferty, J.-Y. Mandin, S. Massie, S. Mikhailenko, C. Miller, N. Moazzen-Ahmadi, O. Naumenko, A. Nikitin, J. Orphal, V. Perevalov, A. Perrin, A. Predoi-Cross, C. Rinsland, M. Rotger, M. Šimečková, M. Smith, K. Sung, S. Tashkun, J. Tennyson, R. Toth,

A. Vandaele, and J. Vander Auwera, "The HITRAN 2008 molecular spectroscopic database," *Journal of Quantitative Spectroscopy and Radiative Transfer*, vol. 110, pp. 533–572, June 2009.

[120] D. Weidmann, L. Joly, V. Parpillon, D. Courtois, Y. Bonetti, T. Aellen, M. Beck, J. Faist, and D. Hofstetter, "Free-running 9.1 μm distributed-feedback quantum cascade laser linewidth measurement by heterodyning with a $C^{18}O_2$ laser," *Optics letters*, vol. 28, pp. 704–6, May 2003.

[121] L. Tombez, J. Di Francesco, S. Schilt, G. Di Domenico, J. Faist, P. Thomann, and D. Hofstetter, "Frequency noise of free-running 4.6 μm distributed feedback quantum cascade lasers near room temperature," *Optics letters*, vol. 36, pp. 3109–11, Aug. 2011.

[122] L. Tombez, S. Schilt, J. Di Francesco, T. Führer, B. Rein, T. Walther, G. Di Domenico, D. Hofstetter, and P. Thomann, "Linewidth of a quantum-cascade laser assessed from its frequency noise spectrum and impact of the current driver," *Applied Physics B*, vol. 109, pp. 407–414, Apr. 2012.

[123] R. Walker, *Quantum Cascade Laser Spectroscopy : Applications and Developments*. PhD thesis, University of Oxford, 2011.

[124] R. J. Walker, J. H. van Helden, and G. A. D. Ritchie, "Quantum cascade laser absorption spectroscopy of the band of deuterium bromide at 5 μm," *Chemical Physics Letters*, vol. 501, pp. 20–24, Dec. 2010.

[125] R. J. Walker, J. Kirkbride, J. H. Helden, D. Weidmann, and G. A. D. Ritchie, "Sub-Doppler spectroscopy with an external cavity quantum cascade laser," *Applied Physics B*, vol. 112, pp. 159–167, Apr. 2013.

[126] V. V. Khodos, D. A. Ryndyk, and V. L. Vaks, "Fast-passage microwave molecular spectroscopy with frequency sweeping," *The European Physical Journal Applied Physics*, vol. 25, pp. 203–208, Feb. 2004.

[127] J. H. van Helden, R. Peverall, G. A. D. Ritchie, and R. J. Walker, "Rapid passage effects in nitrous oxide induced by a chirped external cavity quantum cascade laser," *Applied Physics Letters*, vol. 94, no. 5, p. 051116, 2009.

[128] J.-S. Wang, J. Levy, S. Kukolich, and J. Steinfeld, "Microwave transient nutation measurements of relaxation in OCS and NH_3," *Chemical Physics*, vol. 1, pp. 141–148, Mar. 1973.

[129] Y. Matsuo, T. Minowa, H. Komatsu, and T. Shimizu, "Rotational- and vibrational-state dependence of transverse relaxation rate constants of OCS," *The Journal of Chemical Physics*, vol. 82, no. 7, p. 3127, 1985.

[130] G. P. Srivastava, D. Kumar, and A. Kumar, "Temperature dependence of pressure broadened linewidths in the microwave region," *The Journal of Chemical Physics*, vol. 66, no. 1, p. 20, 1977.

[131] R. A. Creswell, S. R. Brown, and S. R. H., "Linewidths in OCS: Isotope effects, vibrational effects, temperature dependence, and T_1/T_2," *The Journal of Chemical Physics*, vol. 64, no. 4, p. 1820, 1976.

[132] M. Harris, C. Adams, S. Cornish, I. McLeod, E. Tarleton, and I. Hughes, "Polarization spectroscopy in rubidium and cesium," *Physical Review A*, vol. 73, p. 062509, June 2006.

[133] C. Carr, C. S. Adams, and K. J. Weatherill, "Polarization spectroscopy of an excited state transition," *Optics letters*, vol. 37, pp. 118–20, Jan. 2012.

[134] P. Kulatunga, H. Busch, L. Andrews, and C. Sukenik, "Two-color polarization spectroscopy of rubidium," *Optics Communications*, vol. 285, pp. 2851–2853, June 2012.

[135] S. Bartalini, S. Borri, and P. De Natale, "Doppler-free polarization spectroscopy with a quantum cascade laser at 4.3 μm," *Optics Express*, vol. 17, p. 7440, Apr. 2009.

[136] A. Goi, K. Syassen, and M. Cardona, "Effect of pressure on the refractive index of Ge and GaAs," *Physical Review B*, vol. 41, no. 14, pp. 104–110, 1990.

[137] Isomet, "Maximizing AO Diffraction efficiency," 2006. http://www.isomet.com/App-Manual_pdf/Maximizing DE.pdf.

[138] A. Feldman, R. M. Waxler, and D. Horowitz, "Photoelastic constants of germanium," *Journal of Applied Physics*, vol. 49, no. 4, p. 2589, 1978.

[139] B. Gorshunov, A. Shotov, I. Zasavitsky, V. Koloshnikov, G. Vedeneeva, and Y. Kuritsyn, "CW and pulsed $Pb_{1-x}Sn_xSe$ diode laser spectroscopy of $^{14}NH_3$ and $^{15}NH_3$ molecules," *Optics Communications*, vol. 28, pp. 64–68, Jan. 1979.

[140] R. J. Wilson and A. J. McCaffery, "Velocity selected laser polarization spectroscopy: a powerful and versatile method of obtaining the state-to-state differential cross section," *Chemical Physics Letters*, vol. 261, pp. 195–200, Oct. 1996.

[141] M. L. Costen and K. G. McKendrick, "Orientation and alignment moments in two-color polarization spectroscopy.," *The Journal of Chemical Physics*, vol. 122, p. 164309, Apr. 2005.

[142] N. Mukherjee and R. N. Zare, "Polarization of molecular targets using infrared stimulated Raman adiabatic passage," *The Journal of chemical physics*, vol. 133, p. 094301, Sept. 2010.

[143] I. Boradjiev and N. Vitanov, "Transition time in the stimulated Raman adiabatic passage technique," *Physical Review A*, vol. 82, pp. 1–8, Oct. 2010.

[144] A. J. Orr-Ewing and R. N. Zare, "Orientation and Alignment of Reaction Products," *Annual Review of Physical Chemistry*, vol. 45, pp. 315–366, Oct. 1994.

[145] R. N. Zare, *Angular Momentum: Understanding Spatial Aspects in Chemistry and Physics*. Wiley, 1988.

[146] S. Borri, S. Bartalini, I. Galli, P. Cancio, G. Giusfredi, D. Mazzotti, a. Castrillo, L. Gianfrani, and P. De Natale, "Lamb-dip-locked quantum cascade laser for comb-referenced IR absolute frequency measurements," *Optics express*, vol. 16, pp. 11637–46, July 2008.

[147] B. Dahmani, L. Hollberg, and R. Drullinger, "Frequency stabilization of semiconductor lasers by resonant optical feedback.," *Optics letters*, vol. 12, pp. 876–8, Nov. 1987.

[148] O. Svelto, *Principles of Lasers*. New York: Plenum Press, 4 ed., 1998.

[149] R. W. P. Drever, J. L. Hall, F. V. Kowalski, J. Hough, G. M. Ford, A. J. Munley, and H. Ward, "Laser phase and frequency stabilization using an optical resonator," *Applied Physics B Photophysics and Laser Chemistry*, vol. 31, pp. 97–105, June 1983.

[150] E. D. Black, "An introduction to Pound-Drever-Hall laser frequency stabilization," *American Journal of Physics*, vol. 69, no. 1, p. 79, 2001.

[151] T. W. Hänsch and B. Couillaud, "Laser frequency stabilization by polarization spectroscopy of a reflecting reference cavity," *Optics communications*, vol. 35, no. 3, pp. 3–6, 1980.